Sunshade Demonstrator Spacecraft Earth Sphere of Influence Escape Using a Propellant-free AOCS

A Feasibility Study

LEONARDO RICCI

Sunshade Demonstrator Spacecraft Earth Sphere of Influence Escape Using a Propellant-free AOCS

A Feasibility Study

LEONARDO RICCI

Sunshade Demonstrator Spacecraft Earth Sphere of Influence Escape Using a Propellant-free AOCS   /   Sunshade Demonstrator Rymdfarkost Earth Influenssfär flyr med hjälp av en drivgasfri AOCS

Abstract

This thesis provides insights to what is peculiar about a solar sail attitude and orbit control system and provides the assessment, in the form of a feasibility study, of the effectiveness of sail tip vanes as a control hardware to escape the Earth sphere of influence. The demonstrator aims to prove the technology for the Sunshade project, a constellation of solar sails located at the Lagrangian point L1 to obscure part of the solar radiation directed towards earth. Solar sailing poses a few fundamental challenges to spaceflight and it is a yet-to-be-proven branch of space engineering. Other tentative design exist but there is no standard to follow or off-the-shelf component that can be straightforward used. Moreover the scalability to the final project has to be accounted for in every step of the project.

The project is divided in a preliminary dimensioning, followed by a Simulink® based simulation which tests preliminary decisions. The simulation, performed on an orbit on the ecliptic plane, integrates models of Earth's eclipse and environmental disturbance torques. The escape time for a $100\,\text{m}$ solar sail is found to be 1215 days, with a nonlinear PD control algorithm and sail tip vanes as the only control hardware. Attention is also posed on the consequence of a simplified sail film deformation in terms of centre of pressure to centre of mass off-set.

Keywords

Sammanfattning

I detta examensarbete studeras vad som är speciellt med solsegels system för attityd- och bankontroll och ger en bedömning, i form av en möjlighetsstudie, av effektiviteten hos flöjlar som sätts på seglets hörn som kontrollhårdvara för att lämna jordens inflytelsesfär. Demonstratorn syftar till att bevisa tekniken för Sunshade-projektet, en konstellation av solsegel belägen vid lagrangepunkten L1 för att skugga en del av solstrålningen riktad mot jorden. Solsegling innebär några grundläggande utmaningar för rymdfärden och det är en ännu inte bevisad gren av rymdteknik. Annan preliminär design finns, men det finns ingen standard att följa eller standardkomponenter som enkelt kan användas. Dessutom måste skalbarheten till det slutliga projektet redovisas i varje steg i projektet. Projektet är uppdelat i en preliminär dimensionering, följt av en Simulink-baserad simulering som testar preliminära beslut. Simuleringen, utförd på en omloppsbana på ekliptikan, integrerar modeller av jordens skugga och störningar av vridmoment från ett antal källor. Flykttiden för ett 100m solsegel blir 1215 dagar, med en icke-linjär PD kontrollalgoritm och segelhörnsflöjlar som den enda styrhårdvaran. Dessutom studeras förskjutningen av tryckcentrum i förhållande till masscentrum under en förenklad modell av segeldeformation.

Nyckelord

Solsegel, Solstrålningstryck, Attitydkontroll, Flyktbana, Tryckcentrum, Störningsmoment, Eclipse.

Acknowledgments

Contents

List of Figures

List of Tables

List of acronyms and abbreviations

ALM Aluminized Mylar

AOCS Attitude and Orbit Control System

AU Astronomical Unit

BOTEC Back Of The Envelope Calculation

BRF Body Reference Frame

CAD Computer Aided Design

Cm Centre of Mass

ConOps Concept of Operations

Cp Centre of Pressure

DCM Direction Cosine Matrix

DOF Degrees of Freedom

ECI Earth-Centered Inertial

EOM Equations Of Motion

GEO Geostationary Earth Orbit

IGRF International Geomagnetic Reference Field

JPL Jet Propulsion Laboratory

KDE Kinematic Differential Equations

LVLH Local Vertical Local Horizon

OBC On-Board Computer

S/C Spacecraft

SOI Sphere Of Influence

SRP Solar Radiation Pressure

TRL Technology Readiness Level

Chapter 1

Introduction

Every aspect of space is starting to get more mainstream attention, argues Carissa Christensen CEO of Bryce Space and Technology [5]. Nowadays technological advancement and social media have made themes like climate change and geoengineering more and more common to hear. They permeate so much our usual content stream that we don't even notice them anymore. The truth is that the climate change situation is unprecedented: its effects, like global warming, become every day a more evident issue to everyone's eye. In 2020 every month, but December, had an average temperature in the top four ever recorded for that month [6]. Moreover, the year itself was the second warmest in almost 150 years [6]. It is in mankind's best interest to keep researching how to reduce their impact on our planet, and with that, the average temperature increase. Although, should the worst happen, a "seatbelt like" safety measure is needed [7]. As K. Caldeira says [7], geoengineering could serve as an emergency solution to reduce global warming consequences but, the research should start now. That's why the Sunshade project was born: the concept involves flying numerous solar sails to Lagrangian point 1. There they would shade earth from 1% of incoming solar radiation [8]. A feasibility study for the project suggests that around 10^8 sailcrafts would be needed to produce effective results, each with an area of $9000 \, \mathrm{m^2}$. Due to the large surface area and the shade-like shape, the analogy between a sunshade and a solar sail is straightforward. Hence, the solar sail is the Spacecraft (S/C) architecture of choice for the Sunshade project. Due to some highly demanding mission requirements, new technologies have to be developed in order to deploy such an advanced concept. The starting point is to demonstrate that the technology is available and functional. This research lays the foundation for part of that technology, and aims at studying the feasibility of a propellant-free control system for the demonstrator solar sail.

1.1 The Sunshade Project

The Sunshade project is a future geoengineering solution to reduce the Earth's average temperature by $1° \, \mathrm{C}$. This goal could be achieved by shading the incoming solar radiation, about 1% of it, using a constellation of spacecrafts positioned between the Sun and Earth itself [8]. The constellation's location would be around the Lagrangian point 1, where it is

possible to orbit in an equilibrium point between the two celestial bodies. An initial study [8] shows that a surface of $3.71 \times 10^{12}\,\mathrm{m^2}$ would have to be positioned at that point to obtain the predicted reduction in solar radiation. The direct consequence of such a large surface is a great mass, making the whole idea unfeasible. The only viable solution is, therefore, to use solar sails. The suggested solution is to employ 4.12×10^8 spacecrafts each of $9000\,\mathrm{m^2}$ area. In fact, this type of spacecraft allows having a small payload bus attached to a massive sail. The sail is a thin membrane (in the order of $2\,\mu\mathrm{m}$ thick) and doesn't affect the mass budget dramatically. The proposed design of one of the S/C for the Sunshade project weighs just $81\,\mathrm{kg}$.

One problem with such a big number of spacecrafts, apart from the required number of launches and their costs which is covered by Fuglesang and Miciano [8], is the resources that they need during their life cycle. The most evident being propellant. The propellant is used in spacecrafts to perform orbital maintenance and attitude corrections. Fuel production and refueling of an enormous number of spacecrafts would cause an impact on the project economy that risks undermining its core assumptions. Moreover, such a project predicts to have a useful life for the spacecrafts of around 50 years. This implies, propellant-wise, an even more extreme requirement for the Attitude and Orbit Control System (AOCS) that would, in turn, affect the mass budget and, ultimately, the feasibility of the project. Moreover, with such a large area, the moment inertia of the system would be large enough to require over-dimensioned conventional attitude control devices even for a shorter duration mission. Fortunately, solar sails offer a way of providing propellant-less attitude control, exploiting the same force they use to accelerate: the Solar Radiation Pressure (SRP).

1.2   The solar sail technology

Solar sail propulsion is an elegant and revolutionary form of propulsion. Indeed, it is not constrained by the renowned rocket equation in how much acceleration it can provide because it does not rely on mass loss to accelerate. Instead, it gains momentum from the interaction between photons and the sail's surface [1]. As one can imagine, the amount of momentum carried by each solar photon is considerably small: a large number of them need to be intercepted to build up enough momentum to propel the spacecraft. To date, the only way to capture a large number of photons is a large reflective surface. This inherently has two problems: mass and moment of inertia.

Mass is a direct consequence of the amount of material needed to build and support such a large and rigid sail structure. The sail film material has to be highly reflective, to better convert the photon's momentum in sail acceleration, while possessing low surface density. Rigidity, on the other hand, is needed to retain a defined shape during attitude maneuvers and to properly transmit control torques to the entirety of the structure. Sail film shape is especially important as it affects the pressure distribution, hence the total force obtained by a certain amount of light. Additionally, rigidity could affect control authority since a low

value might favor low-frequency vibrational modes. S/C rigidity is usually achieved by the use of booms which each have a certain linear density. At Earth's distance from the Sun barely around 9 N of force are available from SRP per square kilometer of sail [1]. Since the acceleration, according to Newton's second law, is inversely proportional to the mass at a given force, the whole sail ensemble has to be lightweight to be considered a meaningful mean of propulsion.

On the other hand, the moment of inertia grows more than linearly with the surface area while being directly proportional to the control torque needed to produce a given angular rate variation. This poses an evident challenge for the control system design. Moreover, some pointing perturbations are inertia dependent as well, making an extended surface area even more of a challenge from an attitude control standpoint.

Even provided one can face all the structural challenges which come with such size, with a reasonable mass and rigidity, launcher envelopes do not allow as large volumes. So the sail needs to be folded, and a deployment mechanism is to be added and made to work. It is clear that it is a technical and technological challenge to build and operate a solar sail. So far, only a handful of them has passed the design phase [9] [10]. Nevertheless, their usage potential is enormous and fits very well with some specific mission requirements among which fall the Sunshade project ones.

In order to have a functioning flight model of the Sunshade spacecraft the technology has to be further proven. The current Technology Readiness Level (TRL) for such an architecture is around 3. This is particularly true for the AOCS where the goal is to use non-traditional methodologies. In space engineering the solution is to build a smaller scale S/C, the so called "demonstrator" and fly it in a demonstrative mission. The aim of this mission being to test the design philosophy and the technology ultimately proving the feasibility of the full scale project. A schematic of the demonstrator concept is in Fig. 1.1.

1.3 Problem

Striving to develop a spacecraft which can use as little propellant as possible during its life-cycle, the Sunshade demonstrator is intended not to have any fuel consuming thrusters on board. The solar sail technology offers a way around fuel for both attitude and orbit control. These strategies are based on the concept of offsetting the spacecraft's Centre of Mass (Cm), about which the control torques are applied, from the sail's Centre of Pressure (Cp). This concept was introduced by Sohn in 1959 [11] and has been studied ever since. However a number of practical issues remain to be solved and a specific system design is yet to be done.
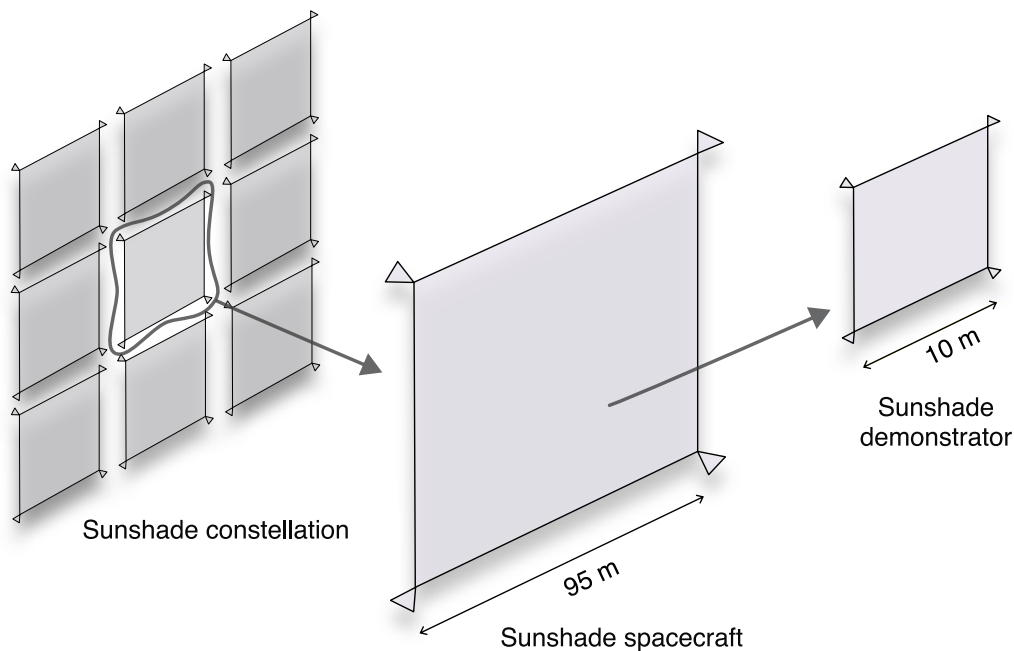
Figure 1.1: Sunshade constellation diagram. Represented are the constellation, the Sunshade S/C and the demonstrator.

1.3.1 Original problem and definition

What are the high level requirements for a 10 metre sided square solar sail's propellant-less AOCS design based on Cm - Cp off-set? This study seeks an answer to this question and all of the related ones that arises. In fact, a number of factors have to be evaluated. Can such a S/C escape earth orbit, which steering law does it have to follow, what is the effect of orbital environment disturbances and eclipse, which dimensions and positions should the control actuators have, are all relevant issues to be tackled when setting a first set of requirements.

1.4 Goals

The goal of this project is to provide an initial set of requirements for the propellant-free AOCS of the Sunshade's project demonstrator spacecraft. This has been divided into the following sub-goals:

1. Prove the sail tip vanes a feasible control hardware and provide dimensions for them;

2. Set an initial steering law for the real system and study its escape performance;

3. Qualify and quantify the perturbations on the system that affect the AOCS performance.

1.5   Delimitation

The analysis conducted in this study only covers the environment inside the Earth's sphere of influence.   None of the reported work has to be considered valid for the Sunshade demonstrator in its trajectory from escape to L1. Moreover, no optimization is performed in terms of exit direction from the sphere of influence, more on this is covered by Fuglesang and Miciano [8]. Additionally, the deployment procedure and its previous mission phases are not analysed, it is assumed that the S/C has already been de-tumbled and that the sail has been nominally deployed.

The control algorithm is not optimized, nor is its tuning. The implementation presented in this study is intended to be a first and simple-to-analyse tool to automatically control the S/C along the steering law and to understand the effects of saturation. No estimation algorithm, software nor hardware is intended to be developed within this study. The assumption is made that all of the relevant data to the control system is obtainable via on-board sensors and data processing.

No structural analysis is preformed. The effects of the control torques on such a system can be relevant to the problem at hand but it is not within the scope of this project. Moreover, the structural properties, related to mass, surfaces, and volumes are considered to be constant over time and not deteriorating by their life cycle.

1.6   Structure of the thesis

This report is divided into 7 chapters. Chapter 2 contains a literature review of the concepts and models that are used to support the research. Chapter 3 covers the methodology: spanning from research process to test environment and analytical tools. The fourth chapter is a description of all of the developed models and frameworks that contribute to the simulation environment. Moreover, it contains dedicated sections to describe some specific studies from which some simulation parameters are derived. Chapter 5 outlines all of the obtained results and their analysis and explanation, whereas the discussion is presented in chapter 6. The discussion is intended to compare the results and highlight their weaknesses and strengths in relation to the research goals. Lastly chapter 7 sums up the work in the conclusion and specifies the limitations of this study as well as describing possible future work.

Chapter 2

Literature study

2.1 Solar Radiation Pressure Force

A common particles physics principle associates sunlight photons to particles, and dictates that each of these photons carries a quantum packet of energy. Due to the mass-energy equivalence it is possible to associate each photon with a certain amount of momentum [1]. If a surface is exposed to sunlight, the momentum-carrying photons impinging on it are going to transfer their momentum resulting in the so called Solar Radiation Pressure (SRP). Depending on the surface orientation, a certain effective area is exposed to the sunlight thus generating an applied force on the solar-sail spacecraft [12]. A number of different models, simplifications and parametrisations of this force exist in literature, here the most important are summarized.

2.1.1 Perfect solar sail

Assuming a perfectly reflecting, rigid and non-deformed solar sail with surface area A the SRP can be described as:

$$\mathbf{F_s} = \mathbf{f_i} + \mathbf{f_r} \tag{2.1}$$

Where the forces applied by impacting and reflected photons, respectively $\mathbf{f_i}$, $\mathbf{f_s}$:

$$\mathbf{f_i} = PA(\hat{\mathbf{u}}_\mathbf{i} \cdot \hat{\mathbf{n}})\hat{\mathbf{u}}_\mathbf{i} \tag{2.2a}$$

$$\mathbf{f_r} = -PA(\hat{\mathbf{u}}_\mathbf{i} \cdot \hat{\mathbf{n}})\hat{\mathbf{u}}_\mathbf{r} \tag{2.2b}$$

Note that $P = 4.563 \times 10^{-6}\,\mathrm{N\,m^{-2}}$ is the nominal solar radiation pressure constant at 1 AU from the Sun. The direction of the impinging and reflected photons as well as the surface normal are identified in Fig. 2.1: $\hat{\mathbf{u}}_\mathbf{i}$ and $\hat{\mathbf{u}}_\mathbf{r}$ are the unit direction vectors of the impacting and reflected photons and $\hat{\mathbf{n}}$ is the sail normal. Minding the vector identity

$$\hat{\mathbf{u}}_\mathbf{i} - \hat{\mathbf{u}}_\mathbf{r} = 2(\hat{\mathbf{u}}_\mathbf{i} \cdot \hat{\mathbf{n}})\hat{\mathbf{n}} \tag{2.3}$$
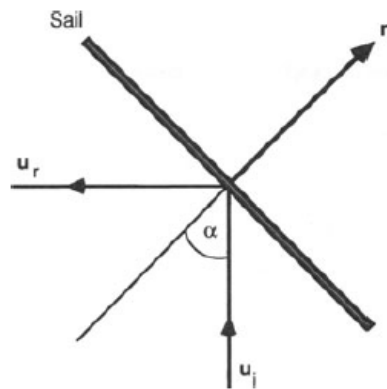
Figure 2.1: Impinging and reflected photons directions and surface normal unit vectors, perfectly reflecting solar sail [1].

The total force becomes:
$$\mathbf{F_s} = 2PA(\mathbf{\hat{u}_i} \cdot \mathbf{\hat{n}})^2 \, \mathbf{\hat{n}} \tag{2.4}$$

Note how the resulting force is directed along the direction normal to the sail and is proportional to the square of the dot product between the incoming sunlight direction and the sail normal direction. This represents the effective exposed area; in fact, the dot product can be associated with the cosine of the angle α since the cosine is the mathematical equivalent of the projection of a direction onto another. Moreover, α, in Fig. 2.1 [1], is called the pitch angle of the sail, i.e. the angle between the sunlight direction and the $\mathbf{\hat{n}}$ direction.

The total SRP force is applied in the Centre of Pressure (Cp): an imaginary point on the sail surface where the resultant force generated from the SRP acting on the sail area, is effectively exerted. This point is generally positioned in the middle-point (centeroid) of the surface. However, since the sail is typically not perfectly straight and non-deformed, the Cp might not be assumed as corresponding to the surface centeroid [13].

2.1.2 Non-perfect solar sail

In reality, a number of factors contribute to make the idealized model presented above not suitable for mission analysis and subsystem design. In fact, the real SRP force is not only deflected from the ideal normal-to-sail-surface direction but also different in magnitude. This is mainly due to two phenomena: real reflective surface, and sail deformation.

Generally speaking each reflective surface, depending on its optical properties, has a reflected, an absorbed, and an emitted portion of the SRP. Each of the components contributes to the force exerted on the sail as:
$$\mathbf{F_s} = \mathbf{f_r} + \mathbf{f_a} + \mathbf{f_e} \tag{2.5}$$

The distribution of how the incoming radiation constitutes each component is dependent on

the reflection coefficient (ρ_r), the absorption coefficient (ρ_a) and the transmission coefficient (ρ_t) [12] [1]. These are indeed the fractions of the incoming photons which are either absorbed, reflected or transmitted. The latter is generally assumed $\rho_t = 0$ on the reflective side of the sail, thus the relation between the other two is:

$$\rho_a = 1 - \rho_r \tag{2.6}$$

Note how the emissivity portion of the SRP, f_e, is not accounted for in Eq. 2.6, this because it is due to re-radiation, thus it is governed by the Stefan-Boltzmann law.

In subsection 2.1.1 only the direction vector $\hat{n}$ was defined as the one identifying the normal to the sail surface. It is now convenient to also define the $\hat{t}$ direction vector which points towards the tangent to the sail surface as in Fig. 2.2 [1]. It is also worth specifying the
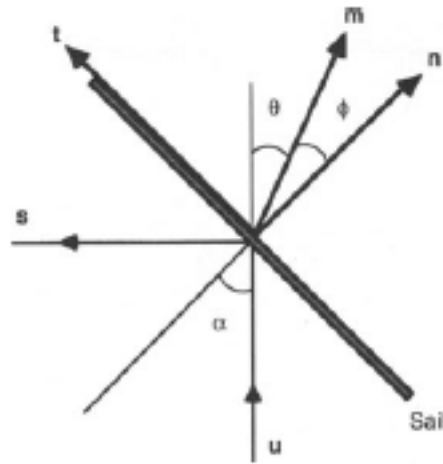
Figure 2.2: Non-perfect solar sail representation with its relevant direction vectors [1].

concept of Lambertian reflector. A so called Lambertian surface is a surface which reflects the light from a certain source with the same brightness no matter the reciprocal angle and position of source and surface [14]. If a non-Lambertian surface is considered a correction coefficient, B, is required.

As McInnes shows in "Solar Sailing. Technology,Dynamics and Mission Applications" [1], the three contributions of the SRP force for a non perfect sail are:

$$\mathbf{f_a} = PA(\cos^2(\alpha)\,\hat{\mathbf{n}} + \cos(\alpha)\sin(\alpha)\,\hat{\mathbf{t}}\,) \tag{2.7}$$

$$\mathbf{f_r} = PA\left[(\rho_r s\,\cos^2(\alpha) + \beta_f(1-s)\rho_r\,\cos(\alpha))\,\hat{\mathbf{n}} - \rho_r s\,\cos(\alpha)\sin(\alpha)\,\hat{\mathbf{t}}\,\right] \tag{2.8}$$

$$\mathbf{f_e} = PA(1-\rho_r)\frac{\epsilon_f B_f - \epsilon_b B_b}{\epsilon_f + \epsilon_b}\cos(\alpha)\,\hat{\mathbf{n}} \tag{2.9}$$

Here s is the fraction of reflected photons which are reflected specularly, ϵ is the emissivity

with its subscripts f and b referring respectively to front (sun-wards) and back surface of the sail. The subscript also apply to the Lambertian correction coefficient B. Distinction between front and back side of the sail is made because the usual sunshade design requires very different properties in the two main phases of the mission: cruising and shading. The most practical way to achieve such characteristic is to build a two sided sail film, which in turn changes the thrust force. Summing up, the two components in $\hat{\mathbf{n}}$ and $\hat{\mathbf{t}}$ directions are:

$$\mathbf{f_n} = PA \left\{ (1 + \rho_r s)\cos^2(\alpha) + B_f(1 - s)\rho_r \cos(\alpha) + (1 - \rho_r)\frac{\epsilon_f B_f - \epsilon_b B_b}{\epsilon_f + \epsilon_b}\cos(\alpha) \right\} \hat{\mathbf{n}} \tag{2.10}$$

$$\mathbf{f_t} = PA(1 - \rho_r s)\cos(\alpha)\sin(\alpha)\,\hat{\mathbf{t}} \tag{2.11}$$

This leads to a force $\mathbf{F_s} = F_s\,\hat{\mathbf{m}}$ in the $\hat{\mathbf{m}}$ direction as per Fig. 2.2. The direction vector $\hat{\mathbf{m}}$ splits the pitch angle α in two: the cone angle θ and the centre-line angle ϕ. The two are consequently related:

$$\alpha = \theta + \phi \tag{2.12}$$

Eq. 2.10 and Eq. 2.11 clarify how the SRP generated force is affected by real optical properties of the sail. Sail film deformation, on the other hand, affects only the magnitude of $\mathbf{F_s}$. The extent of the variation is dependant on the cone angle. In fact, to study such phenomenon a real sail model has to be created and the Solar Radiation Pressure distribution has to be integrated over the sail's surface to find the precise effect of the curvature [1]. Such study has been conducted by the Jet Propulsion Laboratory (JPL) for the comet Halley rendezvous mission and it results in a paramterised model to correct the SRP force magnitude for both sail billowing and film wrinkling:

$$\mathbf{F_s} = F_{s_0}(0.349 + 0.662\cos(2\theta) - 0.011\cos(4\theta))\,\hat{\mathbf{m}} \tag{2.13}$$

Where F_{s_0} is the force's magnitude when $\theta = 0°$.

2.1.3 Common simplifications

While the Solar Radiation Pressure (SRP) model presented in the previous sections is the state of the art for the non-differential SRP force models, it is not typically used when performing high level analysis or feasibility studies [13] [12]. In fact $\mathbf{F_s}$ is usually simplified as:

$$\mathbf{F_s} \approx \eta PA\cos^2(\alpha)\,\hat{\mathbf{n}} \tag{2.14}$$

Here $\eta = 2Q$. Q is the sail's efficiency factor and, according to McInnes [4], is defined:

$$Q = \frac{1}{2}\left[(1 + \rho_r s) + \frac{2}{3}(1 - \rho_r s)\frac{\epsilon_f - \epsilon_b}{\epsilon_f + \epsilon_b}\right] \tag{2.15}$$

Across literature a reflective solar sail film has a typical $\eta = 1.82$ [12] and an ideal maximum value of $\eta_{max} = 2$. The corresponding Q value is $Q = 0.91$ as illustrated by McInnes in "Space-based geoengineering: challenges and requirements" [4], the other parameters typical

values are summarized in Tab. 2.1.

The simplification presented in Eq. 2.14 loses generality with respect to the model in Eq. 2.10 and Eq. 2.11 both in the force direction and in the Lambertian correction coefficient for the sail film. The JPL paramterised model to account for surface deformation, on the other hand, can be used also for the simplified model [8] by simply substituting the cone angle with the pitch angle and adjusting the direction vector:

$$\mathbf{F_s} = F_{s_0} \left(0.349 + 0.662 \cos(2\alpha) - 0.011 \cos(4\alpha) \right) \hat{\mathbf{n}} \qquad (2.16)$$

Where F_{s_0} is the SRP generated force at $\alpha = 0°$ and calculated with Eq. 2.14.

Film type	ρ_r	s	ϵ_f	ϵ_b	Q	η
Reflective	0.88	0.94	0.06	0.06	0.91	1.82
Non-Reflective	0	0	0.01	0.5	0.17	0.34

Table 2.1: Sail film optical and efficiency parameters for generic reflective and non-reflective solar sail [4].

2.2 Metrics

In order to have a meaningful comparison between different set-ups and scenarios a standard metric has to be defined. In literature a number of different sets of parameters are described, the main ones are introduced in this subsection. These not only provide an effective way of comparing results, but also help in understanding a specific design performance.

First of all the specific impulse: I_{sp}, usually defined as the ratio between the thrust and the mass expulsion ratio, is the most common performance metric for space propulsion. As it is, it would not make much sense with a propulsion technique which does not expel any mass while generating thrust. It would, in fact, always be infinite. However, the total impulse delivered by the solar sail is finite, provided that the mission will come to an end. Thus the need of defining the I_{sp} as an efficiency metric. McInnes shows how it can be adapted by modifying the Rocket Equation in order to account for the payload mass over total mass ratio [1]:

$$I_{sp} = \frac{\Delta V}{g} \ln \left(\frac{m_{tot}}{m_p} \right)^{-1} \approx \frac{a_0 T}{g} \ln \left(\frac{m_{tot}}{m_p} \right)^{-1} \qquad (2.17)$$

The approximated version is not valid for close to Sun operations since it is based on specific acceleration a_0 (which will be described next). This result shows how solar sailing can be an efficient type of propulsion if the total mission time T grows large. Generally, in a year long mission solar sail propulsion can be considered more efficient than the vast majority of the traditional chemical propulsion thrusters [1]. Fig. A.1 in appendix gives a better overview of various architectures efficiencies.

The most indicative sail performance metric parameter is the sail's specific acceleration a_0 [8] [1].

$$a_0 = \frac{2\eta AP}{m_{tot}} \tag{2.18}$$

Note how P is a constant, making a_0 dependant on the sail's area, mass and efficiency factor only. This is fundamental when considering that the sail can be used at different distances from the sun, thus having a different P and nullifying the comparability. The reason why this parameter is important is that it gives a direct idea of the absolute thrust capability of the solar sail. Moreover it allows for immediate feedback on what is the weak part of the design since it isolates mass properties from area, dimensions, and film optical properties. Specific acceleration is typically measured in $\mathrm{mm\,s^{-2}}$ and common value range is $0.5\,\mathrm{mm\,s^{-2}}$ to $6\,\mathrm{mm\,s^{-2}}$.

In the context of the specific acceleration formulation another useful parameter is the sail loading σ. This expresses the sail's mass per unit area:

$$\sigma = \frac{m_{tot}}{A} \tag{2.19}$$

This parameter gives a good indication of how much the overall S/C moment of inertia grows with sail size, thus the required control torque to obtain a certain angular velocity. Moreover, this parameter gives a direct feedback on the sail's dimensions. In fact, once defined the payload mass, the efficiency η and the shape, the sail loading indicates what is the size to obtain the desired specific acceleration [1].

The last conventional parameter used to measure solar sail merit is the lightness number β. Defined by Eq. 2.20 [8] the lightness number is a function of the sail efficiency factor and sail loading, thus containing information both about the optical properties of the film material and the structural characteristics.

$$\beta = 1.53 \, \frac{Q}{\sigma} \tag{2.20}$$

With σ expressed in $\mathrm{g\,m^{-2}}$. Note, also, how there is a proportionality constant: 1.53. It is a constant generated from a function of the solar mass and luminosity as stated by McInnes [1]. In fact, β can be interpreted as the ratio between the acceleration induced on the sail by the Sun, i.e. the SRP, and the gravitational acceleration. This makes the lightness number a parameter with which the sail's properties influence its on-orbit force capabilities, effectively being a correction coefficient for the gravitational parameter μ [1]. This can be seen in the vector orbital equation of motion in Cartesian coordinates:

$$\frac{d^2\mathbf{r}}{dt^2} + (1 - \beta) \, \frac{\mu}{r^2} \, \hat{\mathbf{r}} = 0 \tag{2.21}$$

Moreover, a simple effect of the correction is that based on β one can characterize along which Sun's orbit the sailcraft could move, see Tab. 2.2 [1].

Sail β	0	$0 < \beta < \frac{1}{2}$	$\beta < \frac{1}{2}$	$\frac{1}{2} < \beta < 1$	1	$\beta > 1$
Allowed orbit	circular	elliptical	parabolic	hyperbolic	rectilinear	positive effective gravity hyperbolic

Table 2.2: Allowed orbits for a solar sail with lightness number β in a two body problem with solar radiation pressure force and normal directed along the Sun-sail line [1]

2.3 Solar sail Earth orbit escape trajectories

Solar sails have a number of different applications, thus there are a number of orbits which they might be required to follow. More specifically, Earth orbits are just a few of the manifold trajectories they could run in the solar system. However a fundamental step to unlock any of the interplanetary orbits is escaping the Earth's Sphere Of Influence (SOI). This can be done in a variety of ways, as found in literature. Here three standard, simple to understand escape steering laws are presented.

In an orbit around the Sun it is always possible to face a sail's side towards the source of SRP. Around Earth, on the other hand, this condition does not hold. In fact, there always is a part of the orbit which is travelled sun-wards where the SRP would effectively act as a brake. This effect is partially alleviated by a polar escape orbit, but since it is shown to be less efficient than an equatorial one [1] it will not be reported.

In section 2.1 the SRP generated force is always defined on a plane, the one where the Sun-S/C line lays. This convention is used here as well and it derives from assuming the so called clock angle $\delta = 90°$, see Fig. 2.3 [1]. The clock angle δ is defined between the projection of the sail normal on the plane perpendicular to the incoming sunlight, and a reference direction $\hat{\mathbf{p}}$. Similarly, this assumption coincides with considering the trajectory as performed on the ecliptic plane. Thus the SRP force intensity is only function of the cone angle α. With this simplification is possible to analyze the different escape trajectories on a plane, this gives better understanding of the on-going dynamics.

2.3.1 On-Off switching

This steering law is the simplest among the ones suggested, it consists in switching on and off the SRP generated force during the orbit based on the position of the sun relative to the S/C. No position-related pitch angle adjustment is performed, the sail is perpendicular to the sun whenever the S/C is going away from the Sun. On the other hand, it is parallel to the Sun when going sun-wards. This zeroes the SRP force and the losses in orbital energy in that portion of the orbit. The ultimate goal of an escape trajectory is increasing the orbital energy ϵ, in fact, escape is reached when $\epsilon = 0$. With the on-off switching strategy a whole half
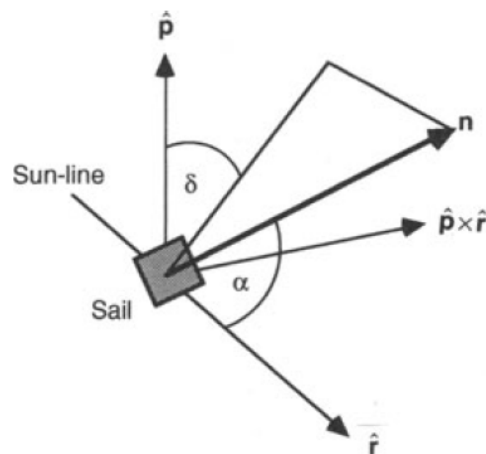
Figure 2.3: Clock (δ) and cone angle (α) representation in the three dimensional space [1] . $\hat{\mathbf{r}}$ is the direction of the incoming sunlight, and $\hat{\mathbf{n}}$ is the sail normal.

of the orbit is not actively producing any energy gain, this accounts for an inefficiency. The active half on the other hand contributes to increasing the the orbit semi-major axis a and the eccentricity e.

Besides inefficiency this method could seem a rather easy strategy to perform orbit raising. This is in general true, but it can be seen that every half orbit a theoretically instantaneous rotation is needed to obtain the correct sail pointing. Such requirement might pose demanding requirements on the control system. A better overview of the escape strategy is displayed in Fig. 2.4 [1].

2.3.2 Orbit rate steering

The most natural way of improving the on-off switching steering is gaining energy even when directed sun-wards. This can be done by exposing to the Sun part of the sail's film even in the second and third quarters of the orbit. Refer to Fig. 2.5 [1]. It is still key, however, not to expose any sail at $90°$ of true anomaly as that causes a reduction in orbital energy.

One way of setting a proper sail pointing in each phase of the orbit is spinning the S/C along its out-of-plane axis at a constant rate. McInnes suggests [1]:

$$\frac{d\alpha}{dt} = \frac{1}{2}\frac{df}{dt} \tag{2.22}$$

Where α is the sail's pitch and f the sail's orbital true anomaly. In order to keep the same sail film side oriented towards the Sun an instantaneous $180°$ rotation is required at $f = 90°$. Once more this can be a weak link in the control system's chain, therefore it has to be taken into account when choosing a strategy.
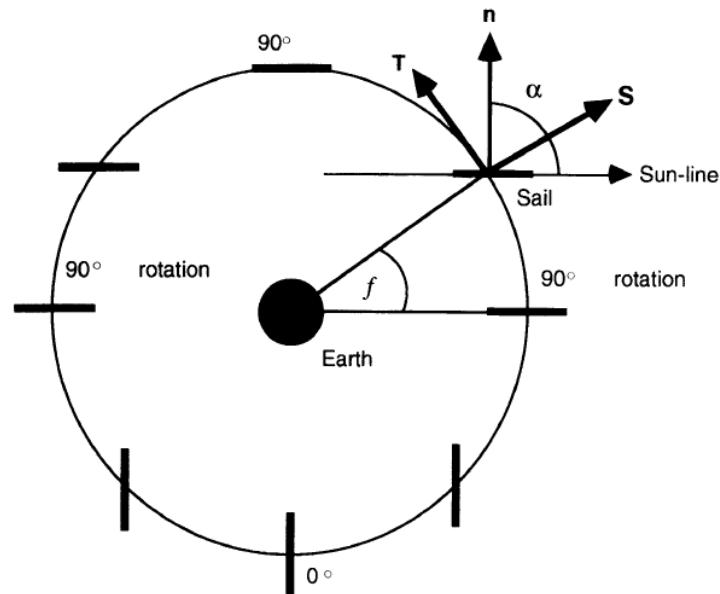
Figure 2.4: On-off switching escape steering strategy representation [1].

The orbital energy increase in the orbit rate strategy is more consistent throughout the whole 360° of true anomaly. This is yielded by greater per-orbit increase in semi-major axis a which is reflected by a lower per-orbit increase in e. In fact, even when the S/C is close to apogee some component of the thrust force is acting, thus raising the perigee. This develops the orbit in a less elliptical shape lowering the eccentricity.

2.3.3 Energy optimal steering

The choice of a spinning rate to improve performance might seem arbitrary, that is why now a locally optimal steering law is presented. The target is maximising the instantaneous rate of change in orbital energy [1]:

$$\frac{d\epsilon}{dt} = \eta P A \left(\mathbf{l} \cdot \mathbf{n}\right)^2 \mathbf{n} \cdot \mathbf{v} \tag{2.23}$$

Where $\mathbf{l}$ is the Sun-line and the other vectors are self explained in Fig. 2.6 [1]. By defining Ψ as the angle of the sail's velocity $\mathbf{v}$ relative to the Sun-line $\mathbf{l}$, one can prove that the energy optimal pitch is:

$$\alpha^* = \frac{1}{2} \left[\Psi - \sin^{-1} \left(\frac{\sin \Psi}{3} \right) \right] \tag{2.24}$$

Here the orbital energy increase is the biggest among the three strategies, this is reflected in the semi-major axis a growth. However the eccentricity grows to a similar extent to the on-off switching strategy. The difference with the previous one is that the energy optimal law has a more efficient propulsion in the away-from-Sun side of the orbit which increases the
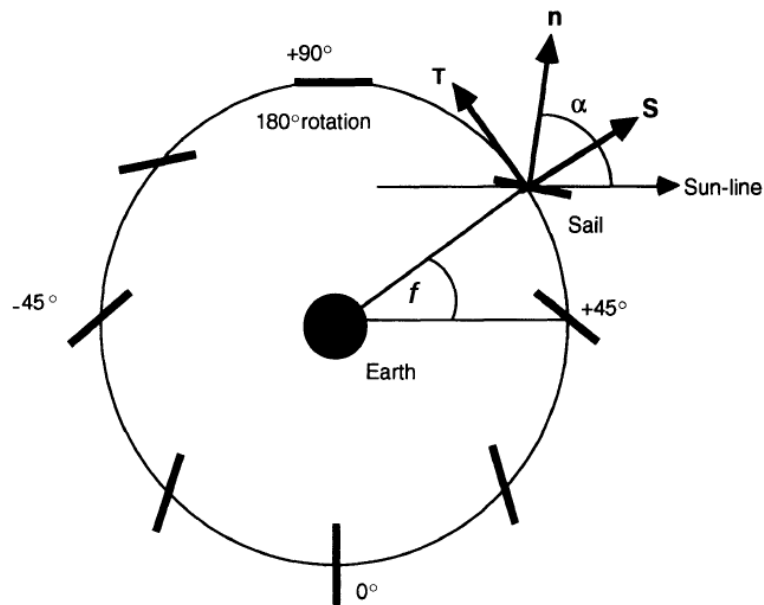
Figure 2.5: Orbit rate steering law representation [1].

apogee altitude more than the orbit rate. The perigee altitude still grows. This indicates how more efficient the present steering law is. To put the efficiency into perspective, as suggested by McInnes [1], one can compare the per-orbit semi-major axis increase brought about by each of these strategies. In general, when orbiting around a planet with standard gravitational parameter μ, it is true that:

$$\Delta a = \zeta \frac{\eta P A}{\mu} a^3 \qquad (2.25)$$

In Eq. 2.25, η is the sail efficiency parameter and ζ is a constant dependent on the chosen

Steering law	On-Off	Orbit rate	Energy Optimal	Polar *
ζ	4.00	5.33	5.52	4.84

Table 2.3: Proportionality constant for the per-orbit a variation, the Polar* is mentioned for completeness.

steering law. Its value is described in Tab. 2.3. All of the presented strategies involve at some point a theoretically instantaneous rotation. It gets more demanding with efficiency, the more efficient strategies need a sudden $180°$ change in pitch angle at true anomaly $f = 90°$. This operation is required if the sail design only has one reflective side of the film. This is usually the case for mass budget reasons. However, a double sided sail could be build and the rotation, either with constant rate or with an optimal angle, could seamlessly continue orbit after orbit. In the Sunshade project the design should have a two sided membrane, but only one has optical properties good enough for propulsion [8] making in necessary to have the rotation at $f = 90°$.
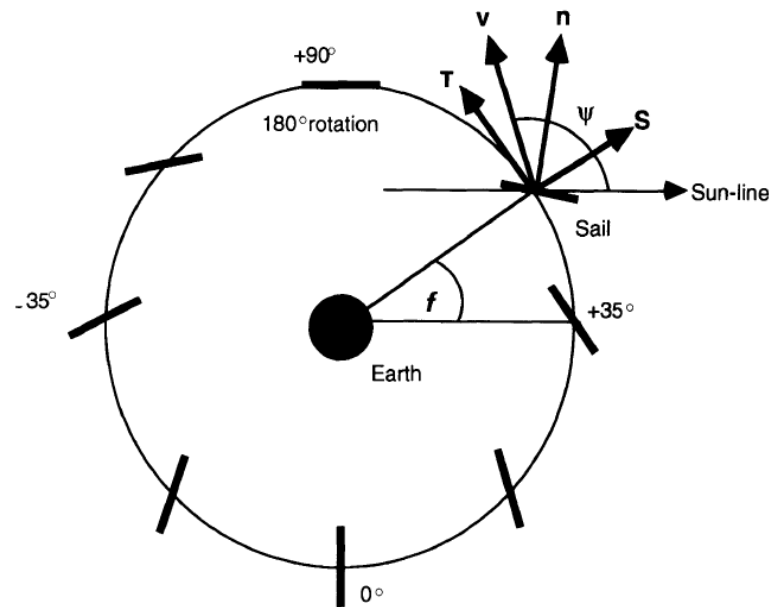
Figure 2.6: Energy optimal steering law representation [1]

Another reason why it might be important to keep the same sail side Sun-facing is passive stability. As shown by Wie [12] a sun-facing S/C could benefit from its Cm being in between the Cp and the Sun. This is not in principle needed for a three axis controlled S/C but might help reducing the control effort in the long term.

2.4 Orbital perturbations

During its life in orbit a Spacecraft is subject to a number of disturbance effects. Some of these affect the optical or thermal properties of the structure, some cause charging while some others affect the dynamics. Among these, two types of perturbations can be identified: the angular accelerations and the forces on the Cm [3]. The first determine part of the attitude control system requirements. Indeed, it should be able to counteract them in order to maintain a correct pointing. The latter, on the other hand affect the orbital dynamics. Literature has a number of interesting studies related to orbital disturbances and perturbations, here notions from the Atchison and Peck's "Length Scaling in Spacecraft Dynamics" [3] will be reported. Their formulation, which relates the order of magnitude of the perturbations to the spacecraft form factor, dimension and altitude, is particularly apt for the present study.

For a square plate with side of $10\,\mathrm{m}$, in an orbit as high as GEO the only relevant acceleration on the Cm which is not related to gravity is the Solar Radiation Pressure. This is covered in section 2.1 and it is considered the source of propulsion for the solar sail. All the other Cm accelerations are not covered in the study for two main reasons: their intensity (around $10^{-10}\,\mathrm{N\,m}$) [3] and the fact that they affect orbital and mission optimization more

than they affect the attitude control requirements.

Angular accelerations, however, are relevant because they directly produce perturbing torques on the system. The main environmental disturbances and the formulation of their torques are listed here.

Gravity gradient

As per Newton's formulation of the Force of Gravity, a given body, even if rigid, does not experience the same gravitational pull on all of its points. The ones which are closer to the source of Gravity are pulled more strongly. This is also suggested by common sense, while holding an elongated object, like a pen, from one of its ends. The implications of this differential pull are important when in orbit. Depending on the mass distribution of the body, in this case the S/C, a torque is produced according to:

$$\mathbf{L}_{GG} = \frac{3\mu}{\mathbf{r}^5} \left(\mathbf{r} \times [I]\, \mathbf{r} \right) \tag{2.26}$$

This is the expression for the first order approximation [15] of the gravity gradient torque. The inertia tensor $[I]$ describes the S/C mass distribution, while $\mathbf{r}$ is the position vector on-orbit of the Spacecraft. This together with Earth's gravitational parameter μ determine the intensity of the gravitational force producing the effect.

Residual magnetic dipole moment

In the orbital environment, specifically within the Earth's magnetosphere there exists a variable magnetic field $\mathbf{B}$. Its intensity varies with altitude, latitude and longitude and is modelled by the International Geomagnetic Reference Field (IGRF) model [16]. Moreover, each spacecraft possesses a certain residual magnetic dipole moment $\mathbf{M}_{sc}$ due to factors like permanent magnetism, internal current loops or magnetism and currents induced by external fields [17]. The cross product of a magnetic dipole with a magnetic field is a torque, in this case experienced as a disturbance by the S/C:

$$\mathbf{L}_M = \mathbf{M}_{sc} \times \mathbf{B} \tag{2.27}$$

If a Class II is applied to the magnetic properties control, the estimation for the magnitude of $\mathbf{M}_{sc}$ is $M_{sc} = 3.5 \times 10^{-3}\,\mathrm{A^2\,m\,kg^{-1}}$ [17], and this is true for a non-spinning spacecraft. The classification system is a three classes categorisation based on a set of design guidelines established by Nasa [17]: Class II implies avoidance of "soft" magnetic materials and current loops, and inspection an testing of suspect parts. It is intended to be average design scenario, where magnetic torques are considered comparable to other torques. Note that this residual dipole value is mass-specific, i.e. it needs to be scaled with the mass of the S/C. The direction of $\mathbf{L}_M$, if the Spacecraft is still in a design phase, has to be accounted for as the worst case scenario [17].

Micrometeoroid collision

The orbital environment is populated with a number of dust and micrometeoroid particles. These impact the S/C surface carrying momentum and, besides degrading the film's surface, they can generate a torque if the Cp is off-set from the Cm. The off-set, $\mathbf{r}_{off}$, between Centre of Mass and Centre of Pressure for a square solar sail is usually assumed to be 0.25% of the square side according to Wie [13]. The validity of this assumption is investigated later in the study.

The micrometeoroid impact torque is then expressed as [3]:

$$\mathbf{L}_{MM} = \mathbf{r}_{off} \times \mathbf{F}_{MM} \tag{2.28}$$

Where the force applied by the impinging particles is [3]:

$$\mathbf{F}_{MM} = \dot{m}_p A \mathbf{v}_{pc} \tag{2.29}$$

$\dot{m}_p = 6.13 \times 10^{-16}\,\mathrm{kg^2\,m^{-1}\,s}$ is the mass flux rate of particles, A is the solar sail surface area an $\mathbf{v}_{pc}$ is the mean particle velocity of the particles roughly directed towards earth:

$$\mathbf{v}_{pc} = G_p \times -20\hat{\mathbf{r}} \tag{2.30}$$

A number of clarifications are needed for Eq. 2.30. $\mathbf{r}$ is once again the S/C position vector, while the number $20\,\mathrm{km\,s^{-1}}$ is a constant derived from the average micrometeoroid velocity observed via photographic measurements [18]. Lastly, G_p is the so called defocusing factor, and it corrects the velocity $\mathbf{v}_{pc}$ for the reduced micrometeoroid concentration in the vicinity of Earth due to the Earth and Moon gravitational field [19].

$$G_p = 0.57 + 0.43\frac{R_E}{r} \tag{2.31}$$

Where R_E is Earth's radius.

Solar wind

The orbital environment is filled with other particles besides micrometeoroids. Some of them, like ions or electrons, are emitted from the Sun and constitute the so called solar wind. These particles carry a momentum, modeled through their momentum flux $\dot{p}_{SW}$ [3], which can be transferred to the sail in the form of a pressure on its surface. This pressure, in the same way that the SRP, is applied on the Cp. Due to this, an off-set usually existing in solar sail between Cm and Cp, results in a disturbance torque:

$$\mathbf{L}_{SW} = \mathbf{r}_{off} \times \mathbf{F}_{SW} \tag{2.32}$$

The formulation of Eq. 2.32 is common among the perturbations generated by a pressure applied on the sail surface. The force produced by the solar wind, through the surface area A

is [3]:

$$\mathbf{F}_{SW} = \dot{p}_{SW} \left(\frac{r_0}{r_S} \right)^2 A \hat{\mathbf{r}}_S \qquad (2.33)$$

Here r_0 is the reference distance from the Sun at which $\dot{p}_{SW}$ is measured. At $r_0 = 1$ AU, $\dot{p}_{SW} = 2.3 \times 10^{-9}\, \mathrm{kg\,m^{-1}\,s^{-2}}$ [20]. Ultimately, $\mathbf{r}_S$ is the position vector from the Sun to the S/C. In the formulation of the solar wind related disturbance the Parker Spiral angle is disregarded, however its value should be considered an upper boundary since the Earth's magnetosphere would filter most of the incoming particles, thus reducing the $\dot{p}_{SW}$ value.

Parasitic solar radiation pressure

The Solar Radiation Pressure is used by the solar sail as a propulsive mean, i.e. a thrust. Its formulation is described in section 2.1. As stated, the SRP generated force $\mathbf{F}_s$ is applied in the Cp, thus not on the Centre of Mass. Across this study a 0.25% of the sail side is accounted for as Cm-Cp off-set [13]. Once again, this off-set $\mathbf{r}_{off}$ acts as a moment arm which origins the parasitic SRP disturbance torque:

$$\mathbf{L}_{SRP} = \mathbf{r}_{off} \times \mathbf{F}_s \qquad (2.34)$$

Planetary albedo

The same solar flux which is generating the SRP on the solar sail impacts also the planets in the solar system. These, in turn, reflect part of the incoming radiation and generate yet another radiation pressure on the bodies that orbit around them. This happens also to a solar sail orbiting Earth. Specifically the pressure generated by Earth's albedo is [3]:

$$P_{EA} = P \left(\frac{2}{3} \eta_p \frac{R_E^2}{r^2} \right) \qquad (2.35)$$

Here P is, once more, the nominal solar radiation pressure constant at 1 AU, η_p is the fraction of the incoming radiation which is reflected by the planet, Earth in this case, and it is assumed to be constant at $\eta_p = 0.306$ [21]. Lastly, R_E is once more Earth's radius and $\mathbf{r}$ is the S/C position on orbit.

The pressure generated by albedo radiation P_{EA} is converted into a force by using the same principles used in subsection 2.1.1 for the SRP generated force. However, no attitude correction is applied here, this means that the reciprocal orientation of the solar sail surface area A with respect to Earth is not accounted for in the formulation. The result is an upper bound for the planetary albedo disturbance torque:

$$\mathbf{L}_{EA} = \mathbf{r}_{off} \times \mathbf{F}_{EA} \qquad (2.36)$$

Where $\mathbf{F}_{EA}$ is the force applied in the Cp generated by the albedo radiation according to:

$$\mathbf{F}_{EA} = A P_{EA} \hat{\mathbf{n}} \qquad (2.37)$$

Planetary thermal emission

According to Atchison and Peck [3], planetary thermal emission, regulated by the Stephan-Boltzmann law produces a radiation which impacts on the solar sail. This, similarly to the planetary albedo or the solar radiation, carries a momentum which is carried over to the S/C in the form of a pressure. The pressure then generates a force in the direction of the sail's normal, applied in the Cp. Its off-set with the Cm, defined as $\mathbf{r}_{off}$ functions as a moment arm and results in the disturbance torque:

$$\mathbf{L}_{PTE} = \mathbf{r}_{off} \times \mathbf{F}_{PTE} \tag{2.38}$$

The force is an upper boundary since, similarly to the planetary albedo, is expressed with no correction for the sail attitude:

$$\mathbf{F}_{PTE} = A P_{PTE} \hat{\mathbf{n}} \tag{2.39}$$

Here $\hat{\mathbf{n}}$ is the solar sail normal and P_{PTE} is the planetary thermal emission pressure [3]:

$$P_{PTE} = \frac{\sigma \xi_P T_P^4}{c} \left(\frac{R_E}{r} \right)^2 \tag{2.40}$$

σ is the Stephan-Boltzmann constant, ξ_P is the planet's emissivity assumed to be $\xi_p = 1$ [3]. c is the speed of light, $T_p = 255\,\mathrm{K}$ is the Earth's temperature as assumed in Atchison and Peck formulation [3].

Poynting-Robertson drag

Generally speaking the solar sail is considered a hot body, i.e. emitting thermal radiation itself. When such body moves with velocity $\mathbf{v}$ there is a Doppler shift in the thermal radiation radiated in the velocity and anti-velocity directions[3]. This imbalance causes a force, once more applied in the Cp thus generating a disturbance torque through the off-set $\mathbf{r}_{off}$:

$$\mathbf{L}_{PR} = \mathbf{r}_{off} \times \mathbf{F}_{PR} \tag{2.41}$$

$\mathbf{F}_{PR}$ is a drag force and is expressed as [22]:

$$\mathbf{F}_{PR} = -\frac{\sigma \xi T^4}{c^2} A \mathbf{v} \tag{2.42}$$

The numerator term in the fraction is derived from the Stephan-Boltzmann law, this time, however, the parameters are S/C related. ξ is the emissivity and T the temperature.

Eddy current damping

Another notable disturbing effect acting on a S/C moving on an orbit is the damping associated with eddy currents [3]. It is generated by the current loops generated in the structure, or sail film, by the moving electrons driven by the changing magnetic field. In fact, the effect is proportional to the angular rate of the moving body $\boldsymbol{\omega}$ immersed in the magnetic field B, it

is a damping. The formulation of this torque is [17]:

$$\mathbf{L}_{EC} = k_e \left(\boldsymbol{\omega} \times \mathbf{B} \right) \times \mathbf{B} \tag{2.43}$$

The value of k_e is dependent on the geometry and resistivity ρ of the rotating object [17]. The flat square of the sail can be treated a circle of wire [3], thus:

$$k_e = \frac{\pi}{4} \frac{1}{\rho} r^3 A \tag{2.44}$$

Here r is the radius of the current loop, assumed to be the half of the square sail diagonal. Moreover, using the surface area A in Eq. 2.44 corresponds to an upper bound to the disturbance, since the S/C is only seldom rotating around its normal axis, i.e. $\hat{\mathbf{n}}$.

Others

The orbital environment is rich of other phenomena, not mentioned so far, that could create disturbances on an orbiting S/C. These, however, are not considered to be relevant for this study:

- **Aerodynamic drag:** this force applied to the Cp could generate a perturbing acceleration. It is disregarded because of the high altitude of the GEO.

- **S/C thermal emission:** this radiative disturbance is disregarded because the sail film is assumed to be an isothermal surface.

- **Lorentz force:** the centre of charge is considered correspondent to the Centre of Mass, therefore it does not generate any perturbing acceleration.

Chapter 3

Methodology

3.1 Research process

With this being a feasibility study, a specific approach is followed through the research and analysis. The idea is to reach the goal of performing the desired analysis in a step-by-step fashion, which inherently brings understanding of the subject. Such characteristic should not be underestimated by the reader since it allows to proceed with the next step only when having gathered enough knowledge in a sub-field. This is fundamental when performing a first-level study, de facto part of what would be an ESA phase 0 study [23]. Part of the acquired knowledge is then filtered into the next step. This multi-layer architecture will be more evident in chapter 5 where the results of the various steps are outlined and key take-aways described.

Initially, a Back Of The Envelope Calculation (BOTEC) like analysis is performed on S/C inertia and required control surfaces dimensions. The purpose of this is to get an initial set of values that corresponds to initial requirements and compare these with previous designs and studies. Moreover, since the ultimate intent of the demonstrator is to build the actual Sunshade spacecraft, a comparison is provided with the larger-sized sail architecture.

The next step involves familiarizing with the trajectory. In any actively thrusted S/C, the attitude motion is coupled with orbital dynamics. The same is true for a solar sail, its orientation with respect to the Sun's direction will determine a smaller or grater thrust level, thus contributing more or less effectively to increasing the orbital energy. Therefore, when studying the control system, which actively affects attitude, it is fundamental to be aware of what modifications are being made to the orbital parameters. Timing and extent of these modifications are key to determine whether a theoretically optimal trajectory turns out to be optimal even in a simulated real environment.

At this point the control system itself is added to the picture. In both this and the previous step a unit mass for the sail is used, because it yields an almost unitary specific acceleration a_0 which in turn is particularly convenient for results display. Both unconstrained and

constrained control algorithms are tested, to estimate what are the differences and weaknesses of a potentially real system along the selected orbit. Note that a rather simple control algorithm is admittedly used, it is intentional not to develop a sophisticated control in this work. The saturation law is in this phase simply based on the maximum obtainable torque.

Now it becomes relevant to introduce the actual physical model of the S/C in the simulation. Both mass-wise and structure-wise, in the sense that the torque model is developed and integrated. The torque model, described in section 4.6, allows to calculate the required vane deflection angles starting from the control output: a desired control torque. Moreover, it contains a pitch-angle dependent saturation law which defines the obtainable torques envelope. Note that, once the torque model has proven to work, it is not necessary to include vane deflections in the simulation. In fact, by keeping solely the saturation algorithm one can be sure that a solution will be found in terms of vane deflection corresponding to a desired torque for each of the permitted (in envelope) torques.

Then, a couple more iterations are done in building the simulation environment. A correction in the trajectory is added together with orbital disturbances from different sources and eclipse. Only the disturbances which result in an angular acceleration are considered. To do this a solar sail specific study is performed accounting for 9 different environmental sources. The SRP parasitic torque is investigated further in sections 4.9, 5.4.2.

Lastly, the effect of eclipse is analyzed and counteracted introducing a gyroscopic-stability effect: i.e. by spinning up the S/C only for that portion of the orbit.

3.2   Test environment and measurements

All of the research that has been performed within the scope of this study does not involve real world laboratory experiments. For this reason the test environment is entirely virtual and built via software tools. This requires that a set of initial assumptions are made as well as boundaries set. The author's intent is to craft the virtual model, in this case the three dimensional simulation of the Earth's orbital environment, with high fidelity to the real scenario. However, this was not always possible throughout the whole study: partly because of the limits set by the initial assumptions, and partly because of the intrinsic approximation within the models. In each of these instances uncertainty margins are applied. At times, worst case scenario assumptions are made in order to assess the upper bound effect of a phenomenon. Throughout the following chapters all of the relevant assumptions, both initial assumptions and circumstantial ones, will be notified to the reader.

The data gathered from the simulations results are reported as they were collected and no uncertainty is added. This both because of the very nature of the simulation as a model, thus being not an exact representation of the reality, and because no sensor model is added. The inputs to the model are always assumed to be exact and the process with which outputs are

obtained is considered to be accurate to numerical precision, see the following section 3.3 for insights on the software and its settings.

3.3 Analytical tools

For the present reaserch two main softwares are used: Matlab® and Simulink®. The first is used to preform calculations and, generally, plot results. One of the most relevant applications is symbol equations derivation [24]. In fact, this tool allows to solve precisely multi-variable non linear derivatives.

Simulink®, on the other hand, is used to build the simulation environment and solve various differential equations. The simulation model relies on two sets of Equations Of Motion (EOM), thus it has 6 Degrees of Freedom (DOF). The EOM are indeed ordinary differential equations and they are used to propagate spatial and rotational motion of a body in the three dimensions. For simplicity in results post processing a constant time-step integration algorithm is selected as a solver: Fourth-order Runge-Kutta (RK4) [25]. This choice also allows for more control over the number of points in a simulation cycle. The selected time-step is $3\,\mathrm{s}$, this number is chosen for its good behaviour in terms of precision in the results and convergence, moreover it yields a reasonable duration when simulating the full S/C escape orbit. It is worth to note the relative dimension between time-step and simulation time, in fact the whole simulation models a total of $1.12 \times 10^8\,\mathrm{s}$ making the time-step a mere $2.7 \times 10^{-7}\%$ of the total time.

3.4 Assumptions and data validity

As mentioned in section 3.2 when building and executing the simulation model, in all of its different test cases, a series of assumptions are made. First, it is relevant to distinguish between the two types of assumptions used to build the virtual test environment: simplifying assumptions and value assumptions.

- **Simplifying assumptions**: are assumptions made in order to simplify the analysis. In this case, they are typically applied in order to model phenomena with less complexity than in reality. It is a good practice to evaluate the implications of these, in terms of what the differences are compared to the real case or to a more complicated model.

- **Value assumptions**: are assumptions related to specific values in the models. When, for example, building a physical model one might need to assume certain dimensions because the final design is not yet available. Generally, these assumptions do not need to be verified if their choice has a motif.

Throughout this study assumptions are used in two instances: a priori, in order to start building a model and have an initial test case, or in-the-process. The first is the common case for value assumptions and some general model related simplifying assumptions. The

second occur when, as a consequence of a test, a value or a model results to be inappropriate for the research objective.

In order to assess the validity of simplifying assumptions non-dimensional ratios and relative differences are used. These allow to measure the variation introduced with an assumption. Due to this method being a comparison, some models or initial assumptions are taken as true and not verified. This is a limitation of the study, for more on limitations check sections 7.2.

Chapter 4

Models and Studies

4.1 Initial vanes size estimation

The first step in analysing a control system is to define the required torque, hence a preliminary set of hardware dimensions. This can be done based on a number of factors, here some initial assumptions are made. First, since the S/C is assumed to start in a Geostationary Earth Orbit (GEO), the minimum level requirement is that it can rotate quickly enough to keep itself oriented towards the Sun at all times during this orbit. Being the assumed starting orbit, the GEO is the shortest in terms of orbital period (provided the escape trajectory works). Thus it is the one used as a driving factor. However, as seen in section 2.3 a solar sail typically has to rotate around one of its own body axes at least once per orbit to keep the same sail face oriented towards the Sun. This rotation can either be ideal and immediate, or last a fraction of the orbit. The assumption is that the S/C has to rotate around its diagonal axis, being square-shaped, in at least $\frac{1}{8}$ of a GEO. It is estimated that a target angular rate variation of $\dot{\omega}_{\mathbf{B}} = 1 \times 10^{-6} \, \mathrm{rad \, s^{-1}}$ is enough to meet this requirement.

The control hardware is tip mounted vanes. These produce a torque based on their surface area and position with respect to the Cm. For a torque $\mathbf{L}$ applied in the Cm it is known that [15]:

$$\mathbf{L} = \frac{d\mathbf{H}}{dt} = [I] \frac{d\boldsymbol{\omega}}{dt} \tag{4.1}$$

Where $\mathbf{H}$ is the angular momentum and $[I]$ the inertia tensor for the S/C. With Eq. 4.1 it is possible to associate an angular rate variation with a torque and an inertia tensor. A further simplification is made to make the analysis one-dimensional. The inertia tensor is substituted by its equivalent moment of inertia I about the diagonal axis which can be expressed as a function of the area, A, as:

$$I(A) = \frac{\lambda A^{\frac{3}{2}}}{3\sqrt{2}} + \frac{\rho A^2}{12} \tag{4.2}$$

Here λ and ρ are constants indicating, respectively, the structural booms' length density and the sail film's areal density. The torque $\mathbf{L}$ is also substituted with its one-dimensional equivalent, thus being expressed as a function of the vane area A_v and distance from the

centre of mass C:

$$L = 2A_v PQC \tag{4.3}$$

To be precise, C is the summation of the square's half diagonal L and the distance from the boom tip to the vane's Cp. See section 4.4 for further details. Note also that no pitch angle dependency is included in Eq. 4.3 because it is assumed that the analyzed vane can always produce the maximum torque correspondent to a $0°$ pitch angle. Moreover, $P = 4.563 \times 10^{-6} \, \text{N m}^{-2}$ and $Q = 0.85$ are used. While the P value is a common environmental constant for space [4], the choice for Q is described in section 4.4.

This framework allows to compare the vanes required area to the whole solar sail area. This can be done for any given area, in fact, results are provided also in comparison to the future full scale Sunshade mission.

4.2 The orbital simulation

In order to perform any analysis related to the S/C on-orbit behaviour it is fundamental to faithfully reconstruct such environment. Doing so involves mimicking all of the natural phenomena taking place in the orbital environment while allowing the S/C to react along 6 DOF: three translational and three rotational. On top of this, each motion or phenomena description has to be written in a specific reference frame. Thus it is fundamental to clearly establish the relations between each reference frame.

4.2.1 Reference frames

The main reference frame in the simulation is the Earth-Centered Inertial (ECI). This frame is assumed to be inertial, i.e. not undergoing acceleration and where differential equations of motion are true in their common form, see subsections 4.2.2 and 4.2.3. Its centre is located at the Earth's centre of mass and its axes are defined as follows [26]:

- $\mathbf{X}_{ECI}$: Vernal equinox at J2000 [27];

- $\mathbf{Y}_{ECI}$: Right hand orthogonal to $\mathbf{X}_{ECI}$ and $\mathbf{Z}_{ECI}$;

- $\mathbf{Z}_{ECI}$: Earth rotation axis at J2000.

Another relevant frame related to a S/C in orbit and utilized in the computation is the Local Vertical Local Horizon (LVLH). The frame definition can be inferred from Fig. 4.1:

- $\mathbf{X}_{LVLH}$: Direction of the orbital tangent velocity;

- $\mathbf{Y}_{LVLH}$: Right hand orthogonal to $\mathbf{X}_{LVLH}$ and $\mathbf{Z}_{LVLH}$;

- $\mathbf{Z}_{LVLH}$: Direction of the opposite of the spacecraft position vector on orbit.

This frame is used as the reference orbital frame, i.e. the frame with respect to which the attitude parameters measure the difference in orientation. It is not inertial, in fact it is in constant motion along the orbit and has an angular velocity $\boldsymbol{\omega_{orb}}$, directed along $\mathbf{Y}_{LVLH}$, with respect to the ECI frame which causes its acceleration vector to change direction. Lastly,
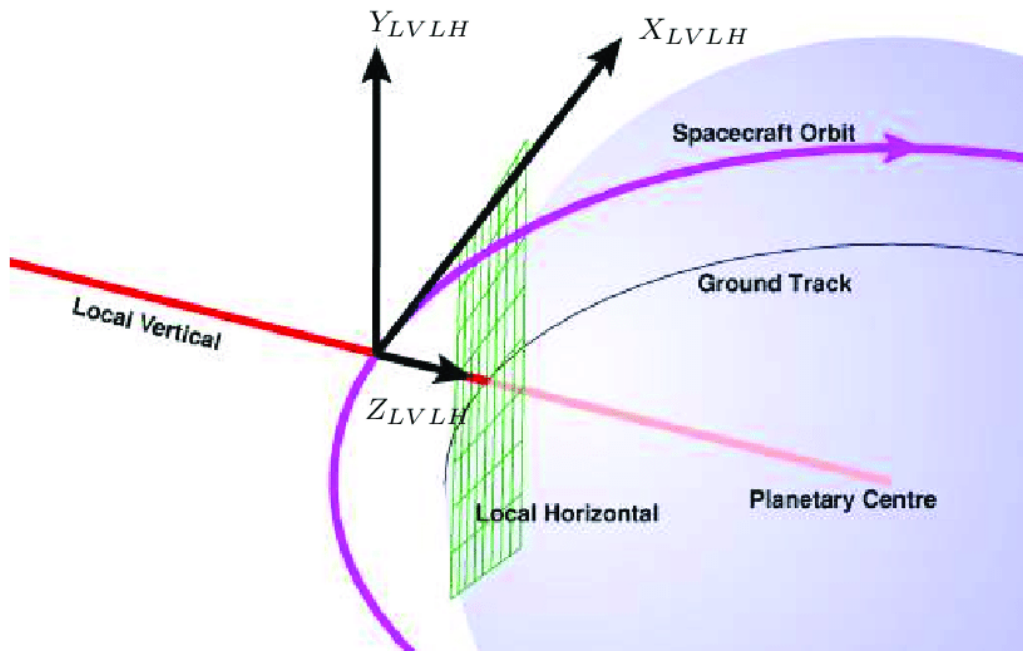
Figure 4.1: LVLH frame definition [2]

the Body Reference Frame (BRF). This is depicted in Fig. 4.2, and it is used to define the control torques and to quantify the disturbances. The rotational equations of motions are ultimately solved in this reference frame. Its origin is assumed to in the Cm, the $\mathbf{Y}_{BRF}$ and $\mathbf{Z}_{BRF}$ direction are on the sail film's plane and point to the hinges of the tip vanes: 4 and 3 respectively. The $\mathbf{X}_{BRF}$ axis is perpendicular to the sail film and directed opposite to the S/C bus, the latter is visible in Fig. 4.6.

Each frame is related to the others by a Direction Cosine Matrix (DCM). This relation is fundamental as it allows to express any vector $\mathbf{v}$ in any desired frame by only using a matrix multiplication, provided that $\mathbf{v}$ is unit length:

$$\mathbf{v^B} = [BE]\ \mathbf{v^E} \tag{4.4}$$

Where $[BE]$ is the DCM from ECI to BRF,

4.2.2 Translation

The first 3 DOF are related to the translation motion, i.e. the motion of the Centre of Mass (Cm) of the solar sail. This motion is governed by Newton's Second Principle of

Dynamics which equates acceleration to force over mass. In a two body Earth-sail system, this accelerations equality can be written as:

$$\frac{d^2\mathbf{r}}{dt^2} = -\frac{\mu}{r^2}\hat{\mathbf{r}} + \mathbf{f} \tag{4.5}$$

This is the differential equation of translational motion, written in ECI frame. Here, μ is the standard gravitational parameter, its value for Earth is $3.986 \times 10^{14}\,\mathrm{m\,s^{-2}}$. Note that Eq. 4.5 is expressed in accelerations form, therefore any term must be expressed in $\mathrm{m\,s^{-2}}$. Specifically, the sum of all the accelerations produced by the forces acting on the sail's Cm is represented by the right hand side of Eq. 4.5. By integrating this equation the solution is found for the motion of the sail's Cm.

In this study the simplification is made that no other force is acting on the spacecraft other than the Solar Radiation Pressure and the gravity, therefore any orbital perturbing acceleration is disregarded. Gravity is expressed by the first term on the right side of Eq. 4.5 while $\mathbf{f}$ is indeed the SRP force only:

$$\mathbf{f} = \mathbf{F_s} \tag{4.6}$$

4.2.3 Rotation

The rotational motion completes the 6 DOF capability of the simulation. If the translational motion accounts for the sail's Cm motion, the rotational motion is around the Cm. In an inertial frame the equation regulating such motion is the Euler Rotational Equations Of Motion (EOM) in the following formulation:

$$\frac{d\mathbf{H}}{dt} = \mathbf{L} \tag{4.7}$$

Provided that the torque $\mathbf{L}$ is applied on the Cm [15]. The $\frac{d}{dt}$ notation implies an inertial frame derivative, but to be informative to the user, Eq. 4.7 needs to be expressed in BRF. This is because $\mathbf{H}$ contains the angular velocity which measures the body frame angular rate with respect to the Cm. The Euler Rotational EOM is expressed in BRF as [15]:

$$[I]\dot{\boldsymbol{\omega}}_B = -\boldsymbol{\omega}_B \times [I]\,\boldsymbol{\omega}_B + \mathbf{L} \tag{4.8}$$

Note the change in the derivative notation and the subscript B which indicate the equation's reference frame. As a consequence $\mathbf{L}$ is the total applied torque about the Cm expressed in body frame.

Eq. 4.8 describes the dynamics of the BRF with respect to the LVLH, for this reason another notation and concept variation is needed. Indeed, the fact that the LVLH frame is not inertial requires the $\boldsymbol{\omega}_{orb}$ orbital angular velocity to be accounted for. Thus:

$$\boldsymbol{\omega} = \boldsymbol{\omega}_B + \boldsymbol{\omega}_{orb} \tag{4.9}$$

Where both are expressed in BRF. Therefore, Eq. 4.8 becomes:

$$[I]\dot{\boldsymbol{\omega}}_B = -\boldsymbol{\omega} \times [I]\boldsymbol{\omega} + \mathbf{L} \qquad (4.10)$$

Another part of the rotational motion tracking is the attitude variation, i.e. the shift in reciprocal position between BRF and LVLH. The attitude parameter selected for this simulation is the unit quaternion expressed with the scalar part q_0 first:

$$\mathbf{q} = (q_0, q_1, q_2, q_3) \qquad (4.11)$$

The selection is justified by the non-singularity property of the quaternion, together with their bi-linear Kinematic Differential Equations (KDE). KDE are used to update the attitude parameter in the simulation, thus tracking its variation. This has to be done together with the angular velocity. In fact, the quaternion KDE is:

$$\begin{pmatrix} \dot{q}_0 \\ \dot{q}_1 \\ \dot{q}_2 \\ \dot{q}_3 \end{pmatrix} = \begin{bmatrix} 0 & -\omega_1 & -\omega_2 & -\omega_3 \\ \omega_1 & 0 & \omega_3 & -\omega_2 \\ \omega_2 & -\omega_3 & 0 & \omega_1 \\ \omega_3 & \omega_2 & -\omega_1 & 0 \end{bmatrix} \begin{pmatrix} q_0 \\ q_1 \\ q_2 \\ q_3 \end{pmatrix} \qquad (4.12)$$

Here the numbered ω_i terms are intended as the components of $\boldsymbol{\omega}_B$.

When solving the Rotational EOM the overall inertia tensor $[I]$ is assumed to be constant and diagonal. The diagonality assumption only coincides with simplifying the selected BRF to be the geometry's principal inertia axes system. It can be done without loss in generality. The constant inertia tensor implies that the variation in the moment of inertia with respect to the body axes produced by the shifts in the vanes' positions are considered negligible. The impact of this assumptions needs to be verified by specific studies with a precise 3D model of the S/C. However, since most of the structural mass is located in the S/C bus and in the fixed sail structure, the assumption is considered valid.

4.2.4   Other features

Besides rotation and translation, which fully describe the Spacecraft motion some other models need to be implemented in the simulation in order to represent the real orbital environment with fidelity. The simulation has other features which where developed as the study progresses. Hence this subsection provides a list of those features and a brief description containing the reference to their own subsection.

The first model is the sunlight model. The Sun gravitational influence is not modeled in the simulation, however sunlight has to be. In fact, is the very source of the SRP force. That said, the simulation has a sunlight model which revolves around Earth, in the ECI frame as the real Sun would do. More precisely it rotates in a plane inclined as the ecliptic plane with respect to $\mathbf{Z}_{ECI}$ of around $0.986°$ per day.

At this point it is worth mentioning the other initial simplifying assumption which is made at simulation level. The orbit used for the study is at GEO altitude but it is not at GEO inclination, similarly to what is reported in section 2.3. In this way the Sun is on the orbital plane, which is the also the ecliptic plane, and the escape dynamics are easier to understand. This choice implies over-estimating the SRP effect since the optimal attitude has the sail perpendicular to the incoming radiation. On the other hand, the effect of the eclipse is over-estimated since such orbit has eclipse in each revolution instead of a seasonal dependency. The latter is considered to be an upper-bound scenario for the control system thus justifying the simplification. Moreover, this assumption allows to directly use the steering laws suggested in section 2.3.

Another integrated model is the eclipse reproduction. The shaded area moves based on the sun position, and its duration is dependent on the S/C-Earth distance. See section 4.10. Moreover, the environmental disturbance torques are modeled according to section 4.9.

4.3 Escape trajectory analysis

The simulation described in the previous section is used as a test bench for most of the studies hereby reported. One of them is the escape trajectory analysis: the steering laws described in section 2.3 are built into a constructed test scenario and their resulting escape trajectories are compared. The objective is not only to understand each steering law's strengths and benefits but also to assess how ad to what extent they might impact the control system. In fact, it is common understanding that in an actively-propelled S/C the attitude is directly influencing orbital parameters and vice versa.

To perform the escape trajectory analysis a specific test set-up has been prepared. The selected initial orbit is at GEO altitude, circular and on the ecliptic plane. The control system is absent from the equation, in the sense that the desired attitude is always considered to be the true attitude at each time instant, therefore no S/C model is implemented nor any rotational EOM are activated. Since the scope of this analysis is to assess the steering laws, the escape condition is not set at the border of the Earth's SOI but at $\epsilon = 0$ J, i.e. when the total orbital energy is null. This allows to evaluate even parts of the trajectory at high eccentricity which would not be reached within the limits of the SOI.

The SRP force model is the one described in section 4.5 where $\mathbf{n}$ corresponds to $\mathbf{X}_{BRF}$. The solar sail's specific acceleration is assumed to be $a_0 = 1 \, \mathrm{mm \, s^{-2}}$, this value is found to yield explanatory results. Lastly, attitude estimation, Sun position and orbital velocity estimation are assumed to be done on-board by a dedicated subsystem which is not described hereby. A combination of a remote ranging strategy and on board sensors is suggested. The Inertial Stellar Compass, by Draper Laboratories, might be a valid sensor array considering its completeness and low impact requirements [12] [28].

The Energy optimal steering law implies an instantaneous $180°$ rotation at true anomaly $f = 90°$. This is not possible to implement in a real case scenario because it would require infinite torque. Any real control system, intuitively, has a limited amount of torque it can deliver, well defined within an envelope of available torques, see section 4.6. To make up for this, a correction needs to be implemented in the Energy optimal steering law, giving way to the Corrected energy optimal steering law. The major difference is that instead of instantaneously rotating $180°$ when the sail's pitch $\alpha = 90°$, the solar sail will start the rotation at a certain α_{turn}. The rotation is then performed at a constant rate until the optimal α matches the actual pitch the sail has in its constant rotation, the slew rate is selected accordingly. One thing to note is that this rotation manoeuvre completely exposes the sail film to the Sun photons in the Sun-ward portion of the orbit. This generates a thrust force opposite to the orbital velocity directly reducing the orbital energy and the semi-major axis in an eccentricity non-efficient manner. In fact the eccentricity increases. For this reason an optimal α_{turn} needs to be found which balances the energy loss with the required torque to perform the manoeuvre. The higher α_{turn} is, the quicker the rotation needs to be since the sail has to rotate $180°$ in a smaller optimal α span.

The tested scenarios are:

- From standard initial orbit to escape with On-Off switching law;

- From standard initial orbit to escape with Orbit rate steering law;

- From standard initial orbit to escape with Energy optimal steering law.

- From standard initial orbit to escape with several α_{turn} angles to find the best Corrected energy optimal escape.

- From standard initial orbit to escape with the selected α_{turn} in the Corrected energy optimal steering law.

4.4   The spacecraft model

4.4.1   The Solar Sail and other Reflective Surfaces

In Fig. 4.2 the S/C Body Reference Frame (BRF) is defined together with the vanes positions and their deflection angles. Note that each vane is numbered and the number can be identified as a subscript to the vane normal in the figure. These normals are indicated in Fig. 4.2 by n_i with i = 1,2,3,4 and represent the direction perpendicular to each vane surface. This is the direction in which each control force, originated on the vane, is directed and it is rotated around its own rotation axis by an angle δ_i, again with i= 1,2,3,4. Note that each vane normal has origin in the vane Cp, which, again, is the point where the resultant force generated by the SRP on the vane's surface is imagined to be applied.
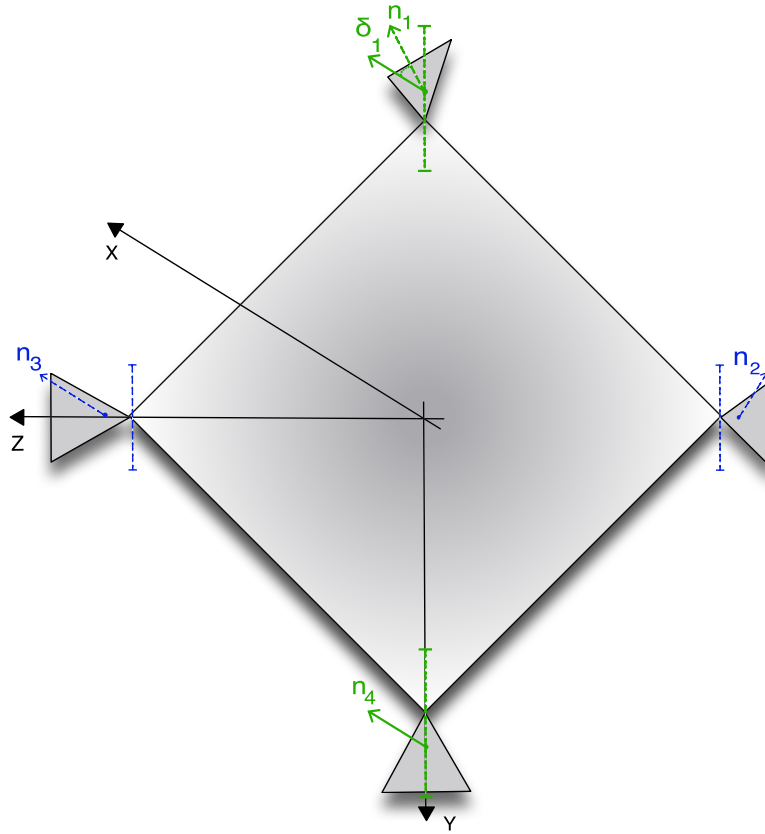
Figure 4.2: Sail film model representation with body reference axes, vanes and their rotation axes.

All the δ_is are defined as positive when rotated positively with respect to the Y body axis identified by the unit vector $\hat{\mathbf{j}}$, and are ultimately aligned with the four vanes rotation axes. All of the rotation axes in Fig. 4.2 are labelled with dashed lines and have T-shaped vertices. One can see how the direction of the rotation axis is always the same. In fact, the pitch vanes, 2 and 3 (in blue), are hinged to rotate out of the sail's plane whereas the roll/yaw vanes 1 and 4 (in green) rotate around their own spar's axis. The choice of this configuration is motivated by the assumption that the pitch angle, controlled by vanes 2 and 3, is the most relevant parameter for a successful escape. The two vanes that are hinged to move out of the sail's film plane, 2 and 3, enable better control of the pitch angle while using a simple deflection angle algorithm, see section 4.6.3.

Based on this physical model each of the four vane normal unit vectors can be the described as follows:

$$\mathbf{n_1} = \cos(\delta_1)\,\hat{\mathbf{i}} - \sin(\delta_1)\,\hat{\mathbf{k}} \tag{4.13a}$$

$$\mathbf{n_2} = \cos(\delta_2)\,\hat{\mathbf{i}} - \sin(\delta_2)\,\hat{\mathbf{k}} \tag{4.13b}$$

$$\mathbf{n_3} = \cos(\delta_3)\,\hat{\mathbf{i}} - \sin(\delta_3)\,\hat{\mathbf{k}} \tag{4.13c}$$

$$\mathbf{n_4} = \cos(\delta_4)\,\hat{\mathbf{i}} - \sin(\delta_4)\,\hat{\mathbf{k}} \tag{4.13d}$$

Note that here, once more, unit vectors $\hat{\mathbf{i}}$ and $\hat{\mathbf{k}}$ indicate respectively the directions of the body X and Z axes.

The reflective surfaces are made with $2.5\,\mu\mathrm{m}$ thick Aluminized Mylar (ALM), this is a value assumption. The details related to the specific assembly design are not yet developed, therefore the assumption is made that each sheet is cut to the specific size and shape and is attached to its support spars as it is. For details about the structure see subsection 4.4.2. Another value assumption is the efficiency factor $Q = 0.85$. This is a conservative value with respect to the one suggested in section 2.1, however it should be more feasible from a TRL standpoint.

Tab. 5.2, in the results, summarizes the vanes chosen dimensions. Each vane is shaped as an isosceles triangle with height, $h = 1\,\mathrm{m}$. The base length, b, is thus determined by the selected vane area as displayed in Fig. 4.4. Initially it it assumed $b = 1\,\mathrm{m}$ according to section 4.1. The choice of a right isosceles triangle is motivated by Fig. 4.3. In fact, the torque difference produced by selecting the the maximum-torque-angle does not justify the added complexity of achieving a precise angle during the deployment phase.
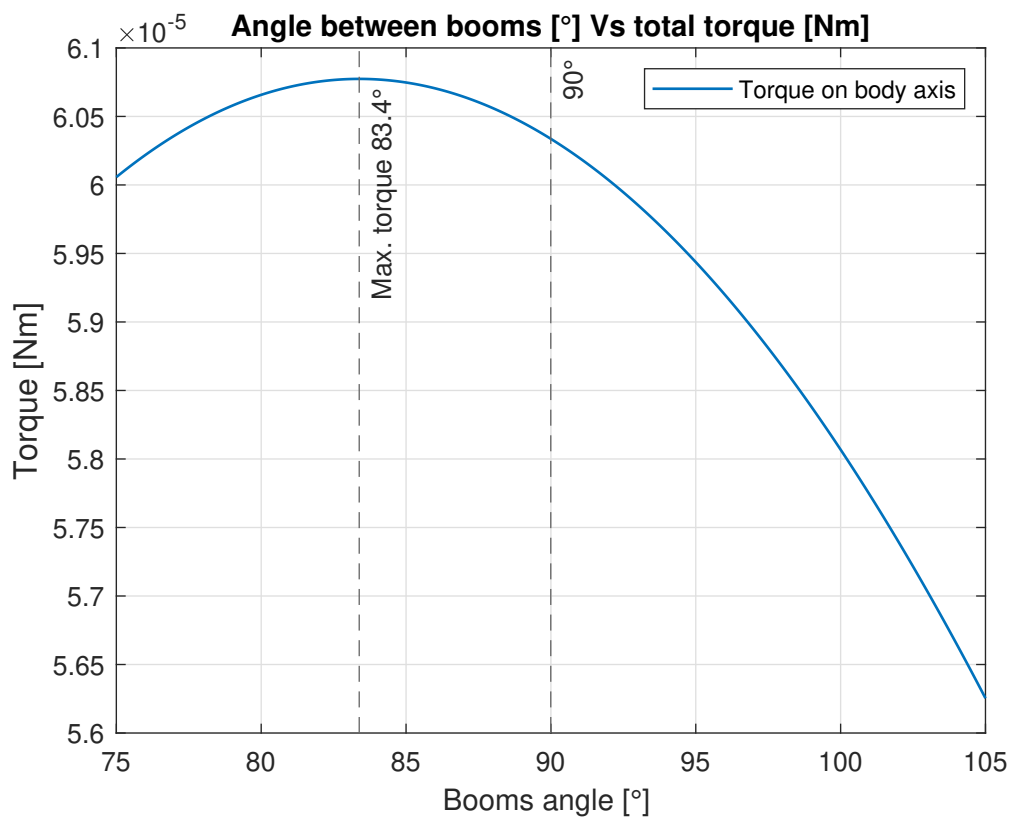
Figure 4.3: Maximum pitch control vane torque variation with respect to the angles between the vane booms ξ.

The Cp for the roll/yaw vanes, 1 and 4, is identified by the position vectors:

$$\mathbf{C}_1 = -(L + l)\,\hat{\mathbf{j}} \tag{4.14}$$

$$\mathbf{C}_4 = (L + l)\,\hat{\mathbf{j}} \tag{4.15}$$

Note how the components are expressed in BRF. This definition is intuitive as these vanes rotate along their symmetry axis and the Cp never falls out of it. L is the half-diagonal length of the sail square, and l is the distance of the Cp from the tip of the triangular sail as indicated in Fig. 4.4. More specifically l is at one-third of the triangle height as that is the application point of a pressure generated triangular distributed load on a line. Here the assumption is made that the pressure distributed on the whole surface is effectively generating load only on the symmetry axis. The back side of vanes 2 and 3, i.e., the pitch vanes, is assumed to be non reflective. The back side corresponds to the positive $\mathbf{X}_{BRF}$ when the deflection angle is zero, see subsection 4.6.1 for details.
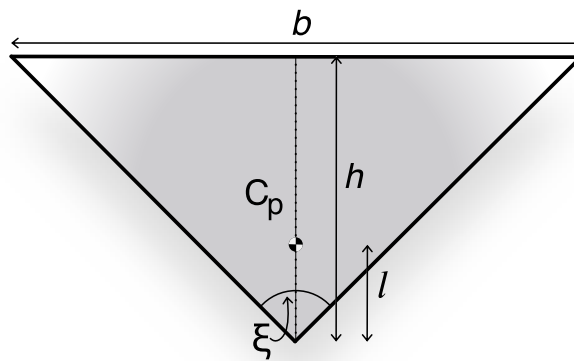
Figure 4.4: Generic vane parameters representation.

Vanes' 2 and 3, i.e. the pitch vanes, Cp definition is:

$$\mathbf{C}_2 = l\,\sin(-\delta_2)\,\hat{\mathbf{i}} - (L + l\,\cos(-\delta_2))\,\hat{\mathbf{k}} \tag{4.16}$$

$$\mathbf{C}_3 = l\,\sin(\delta_3)\,\hat{\mathbf{i}} + (L + l\,\cos(\delta_3))\,\hat{\mathbf{k}} \tag{4.17}$$

This because the vane's symmetry axis, where the Cp lies, is rotated off-sail-plane as showed in Fig. 4.5.

The sail on the other hand is a square with side $10\,\mathrm{m}$. In the geometrical model no wrinkling or billowing is accounted for, thus having a flat surface. However, this is not true for the propulsive force model as described in section 4.5. Moreover, the effective sail area is $100\,\mathrm{m}^2$, no empty gaps or mounting points are considered to be interrupting the illuminated surface as per Fig. 4.2. Tab. 4.1 summarizes the design properties.
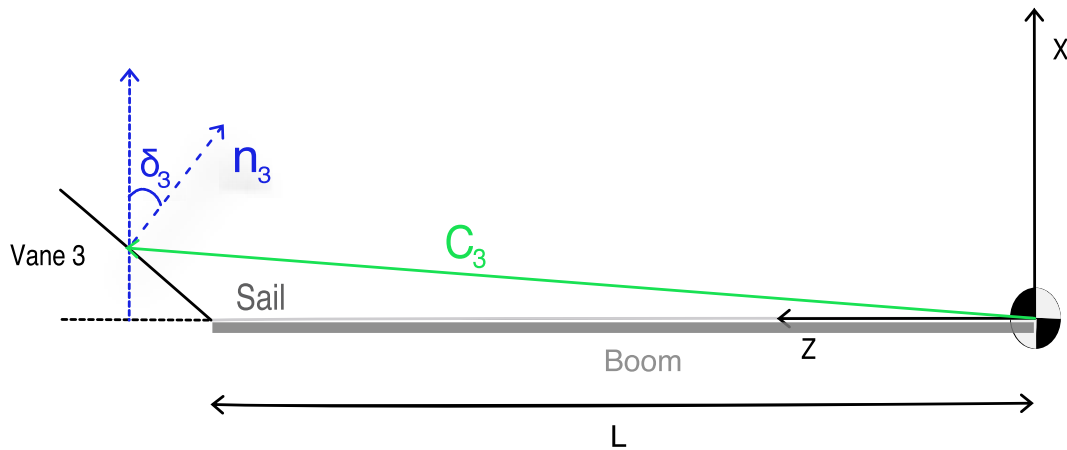
Figure 4.5: Vane 3 Cp position vector $\mathbf{C_3}$ in BRF

Shape	Area [m^2]	Side [m]	Q efficiency factor	Material
Square	100	10	0.85	ALM

Table 4.1: Solar sail reflective surface paramters.

4.4.2   The Spacecraft Bus and Structure

At this stage in the project no bus has yet been designed. However preliminary estimations and other designs [29] [30] show that it should be possible to fit all the required equipment, i.e. the S/C bus in a 6U CubeSat architecture [31]. The bus is intended to house and power the On-Board Computer (OBC), the antennas and transceivers, the power generation and storage system, the data handling devices, the stowed sail prior to deployment and, the attitude estimation sensors with an auxiliary array of attitude actuators. Whether or not the demonstrator mission will carry a payload, other than demonstrating the feasibility of the cruise to L1, is yet to be determined.

Based on these requirements the assumption is made that a 6U CubeSat structure with a mass of $12\,kg$ will be used. This is the maximum mass for a regular 6U CubeSat [31]. Moreover, this preliminary study doesn't account for the out-of-sail-plane shift of the Cm generated by the presence of the S/C bus attached to the sail ensemble. This means that the Cm is considered to be positioned in the centre of the sail, note that this is not in accordance with the 6U CubeSat design specification [31]. On the other hand, according to specification the launch configuration of the structure consists of a box sized $366.0\,mm \times 226.3\,mm \times 100\,mm$, see Fig. 4.6. The basic structure will extend during the sail deployment procedure. The sail structure is supported by 4 spars which will sustain the square sail along its diagonals, as in Fig. 4.7. The spars, or booms, are rolled up in the stowed configuration, the design of the mechanism which unrolls these is not yet designed. The

control vanes themselves are supported by two spars along the short sides of the right triangle and are also rolled up in their launch configuration. A preliminary study is being performed related to this deployment mechanism and its integration in the CubeSat architecture. The one detail already established for the vanes actuators is a constraint on the range of motion. In fact, this decision is a consequence of the rotation axis of each vane, see subsection 4.4.1. The pitch vanes, 2 and 3, rotate outside the plane and their rotational range of motion is constrained to $\delta_{2,3} \in [\,+90°, -90°\,]$ otherwise they wold risk to collide with the sail film. Moreover, the mechanism for the actuator would be complicated and prone to malfunction if a bigger range of motion were targeted, the rotation has to take place outside of the spar axis on which it is mounted. The roll/yaw vanes on the other hand have a range of motion of $\delta_{1,4} \in [\,+180°, -180°\,]$, there is no risk of collision and the installation of a motor co-axial to the spar on which it is mounted is simpler and safer. The fixtures types and numbers attaching the sail film to the structures have not been decided upon but a study is ongoing to find an efficient set-up that doesn't undermine the performance requirements of the Sunshade project. The final dimension of the square sail side, for the demonstrator architecture, is $10\,\mathrm{m}$. All of the relevant values related to the mass and geometrical properties of the structure are gathered in Tab. 4.2

This study covers no analysis relatively to the loading and consequent deformation of the sail structure. In fact, the deformation which might derive from an incorrect deployment procedure or by the effect of the control torque being applied at the tip of the square side is not taken into account in this model. In other words, this study assumes the sail film and its sustaining structures are indeed a perfectly rigid body.

Total mass	Spar length	Bus height	Bus length	Bus width	Sail side	$\sigma\ \mathrm{kg\,m^{-2}}$
$12\,\mathrm{kg}$	$14.1\,\mathrm{m}$	$0.366\,\mathrm{m}$	$0.226\,\mathrm{m}$	$0.100\,\mathrm{m}$	$10\,\mathrm{m}$	0.12

Table 4.2: Demonstrator's structural parameters, the bus related parameters are related to the stowed configuration.
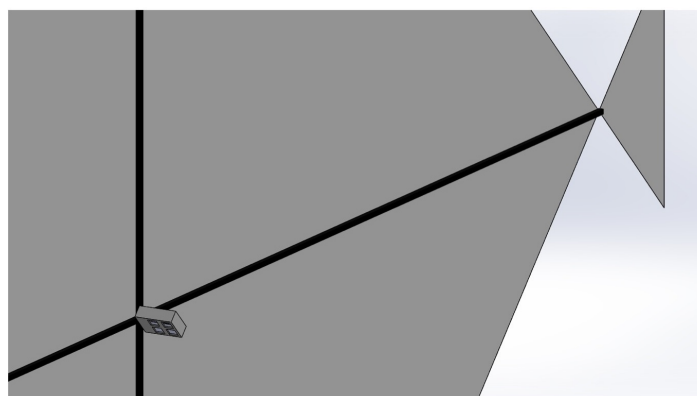
Figure 4.6: Detail: S/C bus attached to the sail ensemble sustained by its spars.
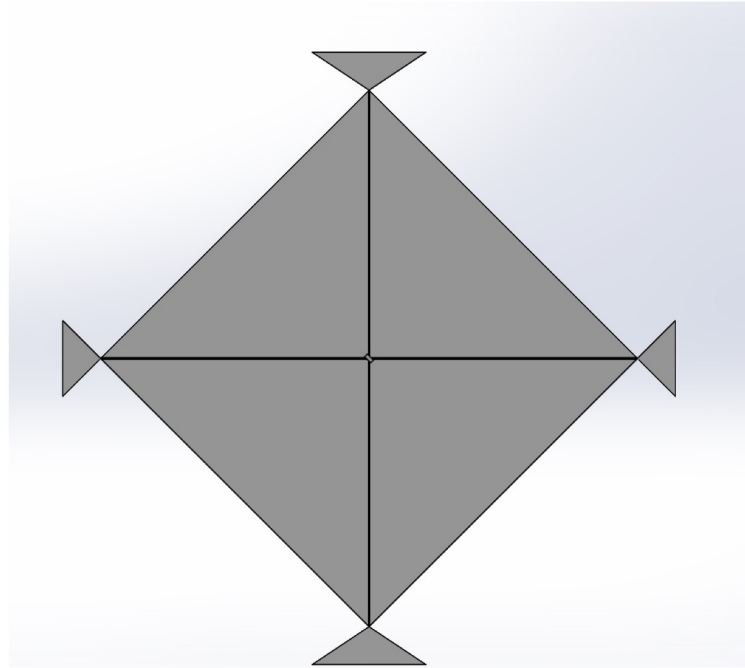
Figure 4.7: Sail structure and sail film, to scale with the assumed dimensions

The inertia tensor, in $\mathrm{kg\,m^2}$, is as follows:

$$[I] = \begin{bmatrix} 300 & 0 & 0 \\ 0 & 200 & 0 \\ 0 & 0 & 200 \end{bmatrix} \tag{4.18}$$

It is self evident that the Body Reference Frame is assumed to be a principal inertia axes system.

4.5 The Solar Radiation Pressure Model

As mentioned previously, the only external force acting on the Centre of Mass of the S/C, besides gravity, is the Solar Radiation Pressure generated force. A model of it is built into the simulation according to subsection 2.1.3:

$$\mathbf{F_s} = \eta P A \left(\mathbf{S}\cdot\mathbf{n}\right)^2 \chi\,\hat{\mathbf{n}} \tag{4.19}$$

Where $\chi(\alpha)$ is the correction coefficient mentioned in Eq. 2.16. Note how the $\cos^2(\alpha)$ component in section 2.1 is here substituted by $(\mathbf{S}\cdot\mathbf{n})$ to account for three-dimensional inclination effects on the force magnitude [1]. Here an important simplifying assumption is made with regards to the direction of the resultant SRP generated force, in fact it is always assumed to be pointing in the normal-to-sail direction. This assumption is common in phase 0-like studies [13]. However, a number of other factors are accounted for: first of

all, the wrinkling and billowing behaviour. The sail, as virtually any sail one can think of, when exposed to the photons flow changes its shape in what is defined as the sail billowing. Moreover, the film surface, under the prolonged influence of energetic particles changes its properties and becomes wrinkled. The effects of these are simulated in the model by using the correction coefficients described in section 2.1.

At the same time, the coefficient η compensates for the real optical and thermal properties of the material except for the Lambertian reflectivity. Once more, reference to the literature study in section 2.1 for the full explicit equation formulation of the parameters. Another simplifying assumption which is made throughout the study is related to the value of the nominal solar radiation pressure constant P. This value is assumed to be constant, even if according to literature [32] it would vary with the inverse squared of the distance S/C-Sun. This causes a relative error in the P value of around 2%.

The final values used in the model yield to a solar sail specific acceleration $a_0 = 0.065 \, \mathrm{mm \, s^{-2}}$ and a lightness number $\beta = 0.011 \, \mathrm{m^2 \, g^{-1}}$. Moreover, due to the $\chi(\alpha)$ correction the SRP force profile changes so that it goes to zero at around $\alpha = 60°$ as in Fig. 4.8.
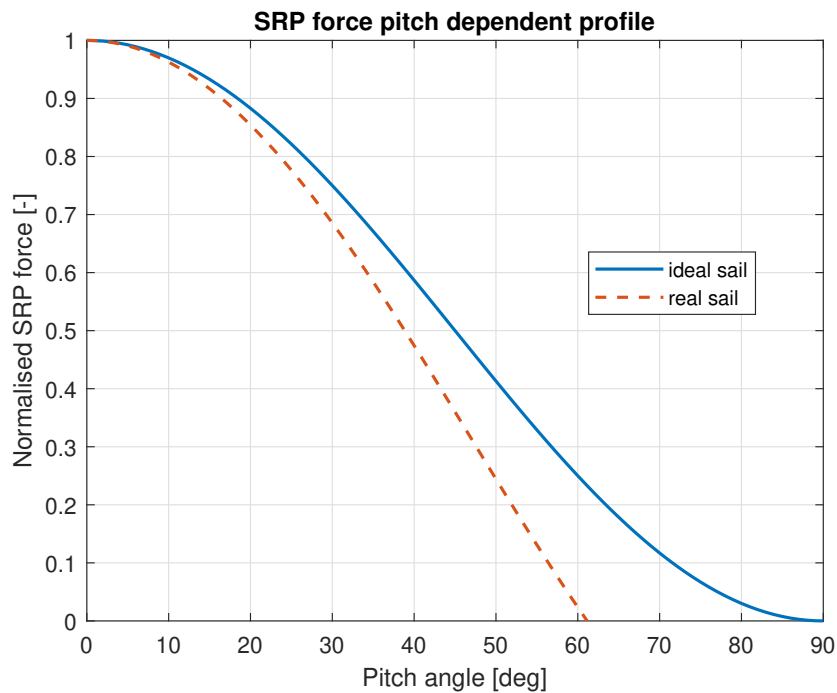
Figure 4.8: SRP generated force for and ideally flat sail compared to a billowed and wrinkled sail.

4.6 The Torque Model

The chosen control hardware is control vanes. In general, any deflection of one of the vanes with which the solar sail is equipped produces a torque around the S/C Centre of Mass. The intensity of the torque depends on several factors: first, the actual vane deflection angle. Secondly, the incoming direction of the sunlight matters, therefore there is a dependency on attitude and position on-orbit. In order to develop a control system and to assess its performance or feasibility, a torque model is required. This should relate a set of vane deflection angles, δ_is, in any environmental condition, i.e. attitude and position on the orbit, to the resultant torque. Ideally, it must also work backwards, form torque and environment to δ_is. The accuracy of this model is crucial because it affects how accurately a generic torque can be translated into a desired vane deflection angle.

In its most general form the torque model is described by [12]:

$$\mathbf{M}_v = \sum_{i=1}^{4} \mathbf{C_i} \times F_v (\mathbf{S} \cdot \mathbf{n_i})^2 \mathbf{n_i} \qquad (4.20)$$

Here the subscript v denotes that the torque is generated by the vanes deflection, the point about which this torque is expressed is the S/C Cm. $\mathbf{C_i}$ is the i-th moment arm from the S/C Cm or the i-th vane Cp description vector. $\mathbf{S}$ is the sun direction vector and $\mathbf{n_i}$ the i-th vane normal direction. It is important to note that each of the vectors in Eq. 4.20 is to be taken in Body Reference Frame so that the resulting torque is iself in BRF. Lastly $F_v = \eta P A_v$ is the maximum force which can be produced by a vane with area A_v and sail efficiency parameter η at 1 AU from the Sun (where $P = 4.563 \times 10^{-6} \, \text{N m}^{-2}$). Note how in the SRP force generated by the vane the $\chi(\alpha)$ correction is missing. The assumption is that the vane structure is sturdy enough to prevent any deformation.

To better understand Eq. 4.20 and to be able to implement it as a sub-model in the simulation each vane's contribution is separated by the others as:

$$\mathbf{M}_1 = F_v L \left[S_x \cos(\delta_1) - S_z \sin(\delta_1) \right]^2 \left[\sin(\delta_1)\hat{\mathbf{i}} + \cos(\delta_1)\hat{\mathbf{k}} \right] \qquad (4.21a)$$

$$\mathbf{M}_2 = -F_v \left[S_x \cos(\delta_2) - S_z \sin(\delta_2) \right]^2 \left\{ l \sin^2(\delta_2) + \cos(\delta_2) \left[L + l \cos(-\delta_2) \right] \right\} \hat{\mathbf{j}} \qquad (4.21b)$$

$$\mathbf{M}_3 = F_v \left[S_x \cos(\delta_3) - S_z \sin(\delta_3) \right]^2 \left\{ l \sin^2(\delta_3) + \cos(\delta_3) \left[L + l \cos(\delta_3) \right] \right\} \hat{\mathbf{j}} \qquad (4.21c)$$

$$\mathbf{M}_4 = F_v L \left[S_x \cos(\delta_4) - S_z \sin(\delta_4) \right]^2 \left[-\sin(\delta_4)\hat{\mathbf{i}} - \cos(\delta_4)\hat{\mathbf{k}} \right] \qquad (4.21d)$$

It can be noted right away that Eq. 4.21a and Eq. 4.21d have components along both the $\mathbf{X}_{BRF}$ and $\mathbf{Z}_{BRF}$ axes. Thus, they are coupled and contribute to the roll and yaw torques. Eq. 4.21b and Eq. 4.21c, on the other hand, are only directed along the $\mathbf{Y}_{BRF}$ axis, and they each contribute to the pitch torque. It is also important to point out that the deflection angles $\delta_2, \delta_3 \in [-90°, 90°]$ while $\delta_1, \delta_4 \in [-180°, 180°]$ due to mounting reasons.

One important characteristic to understand about Eq. 4.21 is the interpretation of the dependency on the Sun direction vector $\mathbf{S}$. $\mathbf{S} = \{S_x, S_y, S_z\}$ and is expressed in BRF, therefore:

$$\tan(\alpha) = \frac{S_z^2 + S_y^2}{S_x} \tag{4.22}$$

Moreover, the S_y component indicates the inclination of the sail around the $\mathbf{Z}_{BRF}$ axis. In other words, if the sail were perfectly perpendicular to the Sun direction, i.e. $\hat{\mathbf{n}} \equiv \hat{\mathbf{S}}$, and then inclined around $\mathbf{Z}_{BRF}$, S_y would give an indication of how much it is leaning forward or backward. In fact, naming γ the said inclination angle:

$$\sin(\gamma) = \frac{S_y}{S} \tag{4.23}$$

Now the three torque components are analysed separately. Note that some additional constraints have to be added to the model in order to properly represent the sail behaviour.

4.6.1 The pitch torque

The pitch torque is defined as the torque applied around the $\mathbf{Y}_{BRF}$ axis. Due to the control vanes architecture, vanes number 2 and 3 both contribute to the pitch torque, and to it only. This can be seen in Eq. 4.21b and Eq. 4.21c. More specifically, the second vane produces the negative pitch torque component, while the third the positive one. This feature largely helps when solving the two equations, in a system, to find the δ_is starting from the torque, as it adds the condition that at least one of the two has always to be zero. For this to be true, however, it is necessary to assume the back-side of the vane as non reflective, i.e. not able to convert the SRP in a force. This is a worst case scenario assumption since it results in the loss of some torque capability at high pitch angles. The pitch torque is thus expressed as:

$$\mathbf{T}_y = \mathbf{M}_2(\mathbf{S}, \delta_2) + \mathbf{M}_3(\mathbf{S}, \delta_{\mathbf{3}}) \tag{4.24}$$

Keep in mind that for any combination of the components of $\mathbf{S}$, the first and the third inform about the sail's pitch angle. Whereas, the second one is essentially a scale factor for the maximum SRP force that the sail can produce at that attitude and with that pitch. Fig. 4.9 depicts the available control torques envelope for $\mathbf{T}_y$ at $\gamma = 0°$ for any pitch angle α. Remember that the positive region is generated by the deflection of vane 3, while the negative by vane 2. Any inclination angle would scale down this envelope retaining its shape unvaried.

The positive and negative regions of the envelope are symmetric with respect to the zero torque plane, therefore the maximum a minimum torques that the control system can produce about the $\mathbf{Y}_{BRF}$ axis are opposite. Respectively, they are $0.06\,\text{N}\,\text{mm}$ and $-0.06\,\text{N}\,\text{mm}$ and they are possible at $\alpha = 0°$, when the sail is perpendicular to the sunlight. These numbers are the consequence of the geometrical model that is used in this study, with its dimensions and control system architecture. Note how, depending on the pitch angle, the maximum and minimum values change. This is due to the effective vane pitch, expressed as α_i in section 4.4,
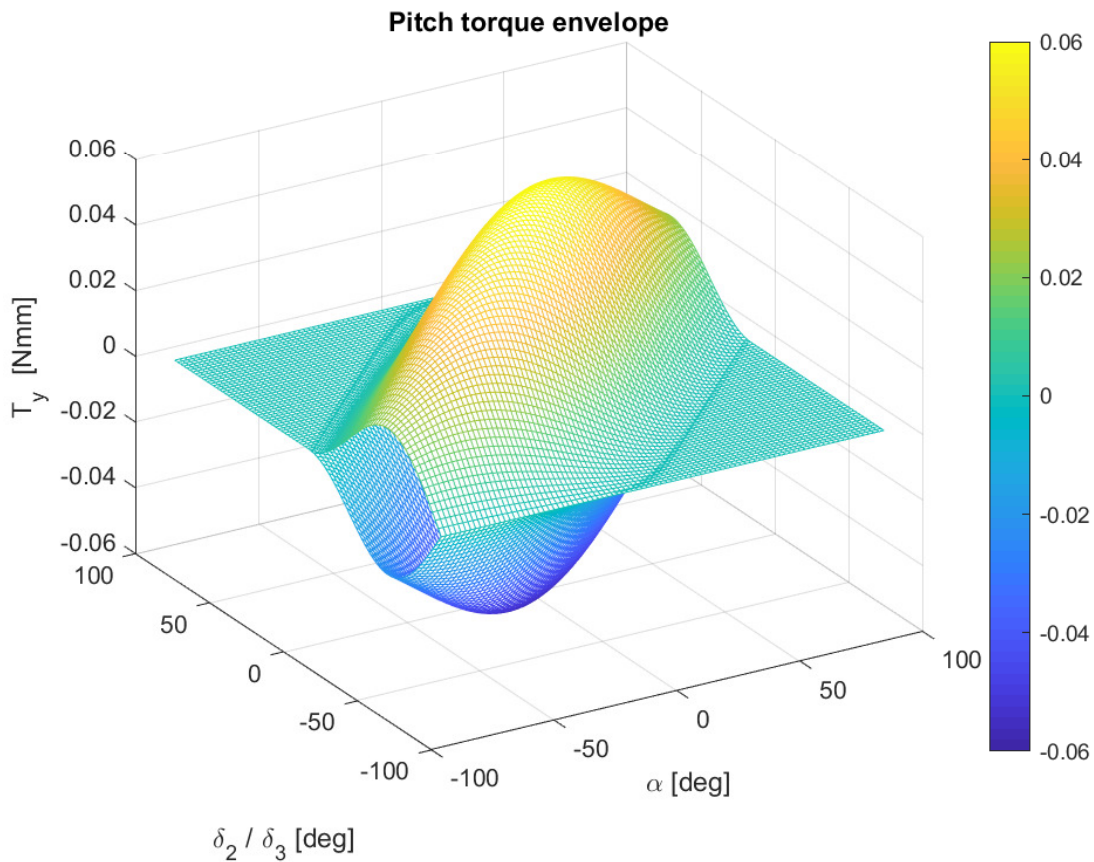
Figure 4.9: Pitch control torque envelope, the positive and the negative regions are generated by the deflections of vane 3 and 2 respectively, non-reflective backside assumption included. The two regions are symmetric with respect to the zero torque plane.

which is the orientation of the vane normal form the Sun direction. This is what ultimately determines the effective exposed vane area which generates the control force.

Lastly, note that there are two evident flat, $T_y = 0\,\mathrm{N\,mm}$, regions. Those are the byproduct of the non-reflective back-side assumption and are obtained by manipulating the envelope generated by Eq. 4.24.

4.6.2   The roll and yaw torques

The roll ($\mathbf{T}_x$) and yaw ($\mathbf{T}_z$) torques definition is not as intuitive as the pitch one, see Eq. 4.25 and Eq. 4.26. In fact, they both depend on the coupled deflection of vanes number 1 and 4, forcing to assess both envelopes together. The deflection of one angle influences both the pitch and the roll torques, limiting the solution space obtainable with the defection of the

other vane. This affects the bandwidth of the saturation law, described in section 4.7.1.

$$\mathbf{T}_x = F_v L \left\{ K_1 \left[S_x \cos(\delta_1) - S_z \sin(\delta_1) \right]^2 \sin(\delta_1) - K_4 \left[S_x \cos(\delta_4) - S_z \cos(\delta_4) \right]^2 \sin(\delta_4) \right\} \hat{\mathbf{i}}$$
$$(4.25)$$

$$\mathbf{T}_z = F_v L \left\{ K_1 \left[S_x \cos(\delta_1) - S_z \sin(\delta_1) \right]^2 \cos(\delta_1) - K_4 \left[S_x \cos(\delta_4) - S_z \cos(\delta_4) \right]^2 \cos(\delta_4) \right\} \hat{\mathbf{k}}$$
$$(4.26)$$

Note that K_1, K_4 coefficients were not indicated in Eq. 4.21. They represent the added constraint, on top of the general model in Eq. 4.20, that the sail film elements can generate force only in the direction opposite to the Sun:

$$K_1 = \text{sign}(\mathbf{n}_1 \cdot \mathbf{S}) \qquad (4.27\text{a})$$
$$K_4 = \text{sign}(\mathbf{n}_4 \cdot \mathbf{S}) \qquad (4.27\text{b})$$

The evaluation of two envelopes at the same time implies that the variation of the torque is displayed as a function of both the vane defection angles. Therefore the assessment has to be performed at a given α. For this reason three cases are presented here, one with zero pitch, one with intermediate pitch and one with the sail almost parallel to the sunlight. Moreover, the envelopes are presented with $\delta_1, \delta_4 \in [-90°, 90°]$ for easier understanding. However the structural geometry allows the whole $360°$ to be used, the full envelopes are available in the appendix Fig. A.2, A.3, A.4. Once more, keep in mind that the S_y component of the Sun direction vector only acts as a scale factor: for clarity of representation reasons it is considered $S_y = 0$. In Fig. 4.10 the roll and yaw control torques envelopes are assessed at the same time. It is important to note, once more, that when selecting a deflection angle for one of the two vanes, the available solution space for both torques is limited to the points laying on the intersection between the plane defined by the selected angle and the torque envelope.

The roll torque ($\mathbf{T_x}$) at low pitch angles has generally lower obtainable values than the yaw torque ($\mathbf{T_z}$), as per Fig. 4.10. In fact, the maximum positive $T_x = 0.63\,\text{N mm}$ whereas $T_z = 0.82\,\text{N mm}$. This is intuitive since the torque around $\mathbf{Z}_{BRF}$ axis can potentially exploit the whole vane being perpendicular to the sunlight. For comparison in Fig. 4.12 when the sail is almost parallel to sunlight the same happens for the rotation around the $\mathbf{X}_{BRF}$ axis. There, the maximum values for the torques are $T_x = 0.082\,\text{N mm}$ and $T_z = 0.063\,\text{N mm}$. Due to the periodicity in the function defining these torques the minimum values, or maximum negative values, have the same magnitude but opposite sign of the positive ones for both torque envelopes. It is also important to note that there exists a zero torque line for both envelopes where $\delta_1 = \delta_4$. Moreover, across all the pitch angle range, the tips of the plots (Fig. 4.10, 4.11, 4.12) all produce zero torque. This because both at $\delta_i = 90°, -90°$ the direction of the torques depends only on the Sun position, which is the same for both vanes thus nullifying the sum of the contributions by each vane.
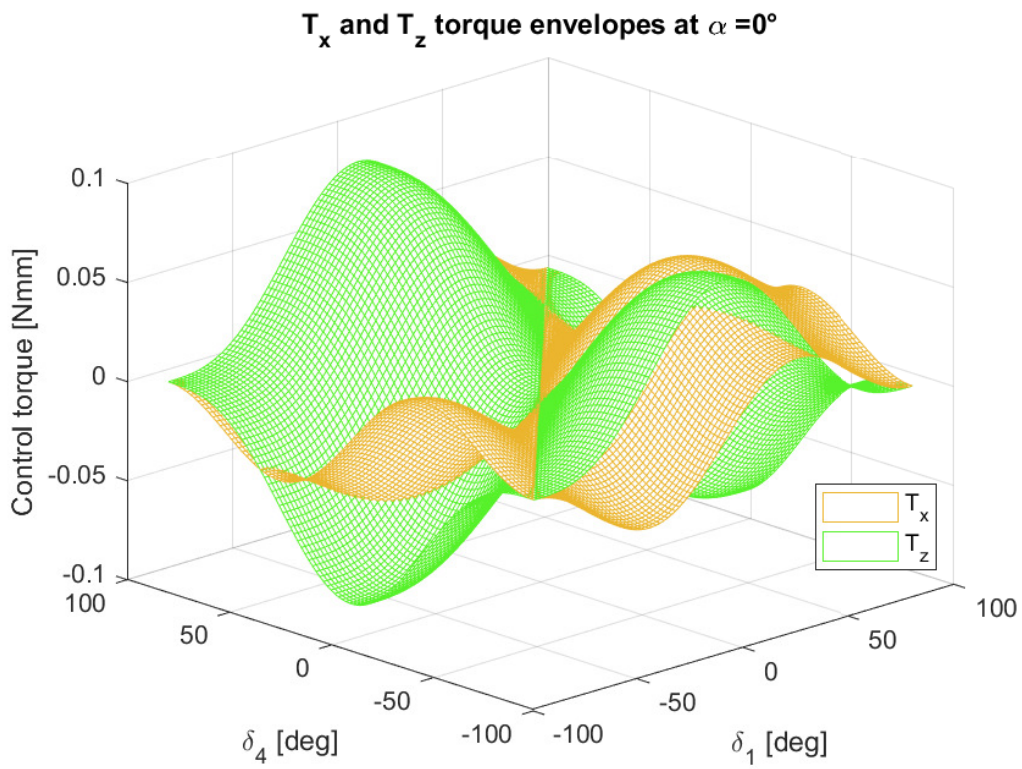
Figure 4.10: Roll and yaw torques overlapped envelopes at $\alpha = 0°$.
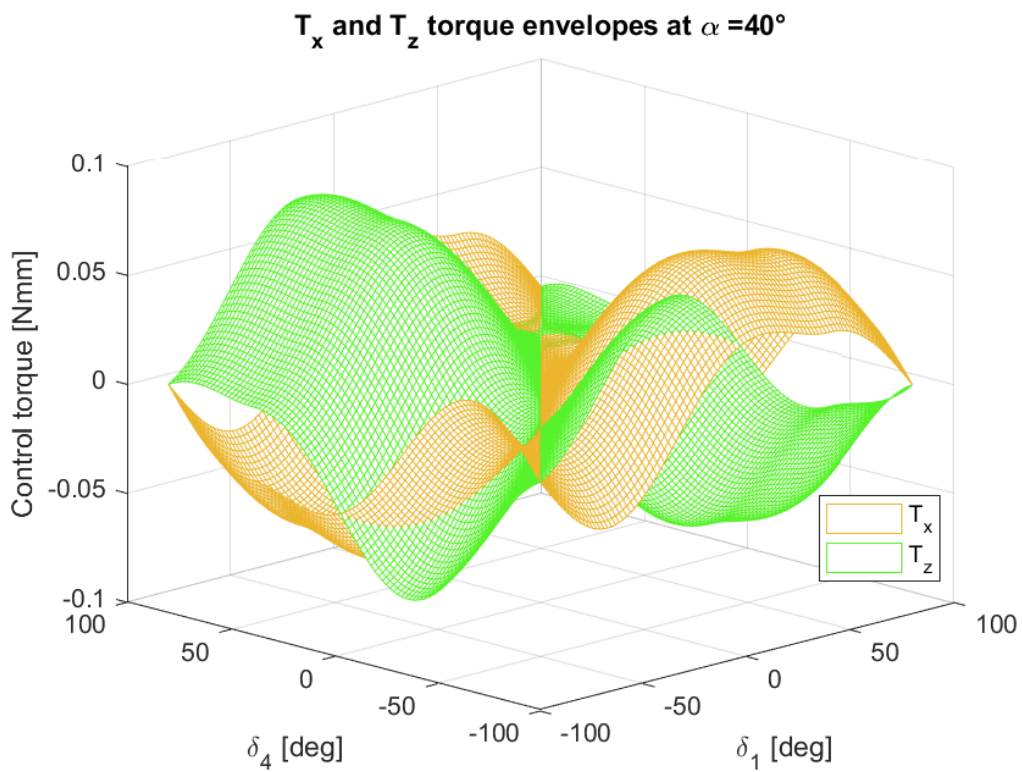
Figure 4.11: Roll and yaw torques overlapped envelopes at $\alpha = 40°$.
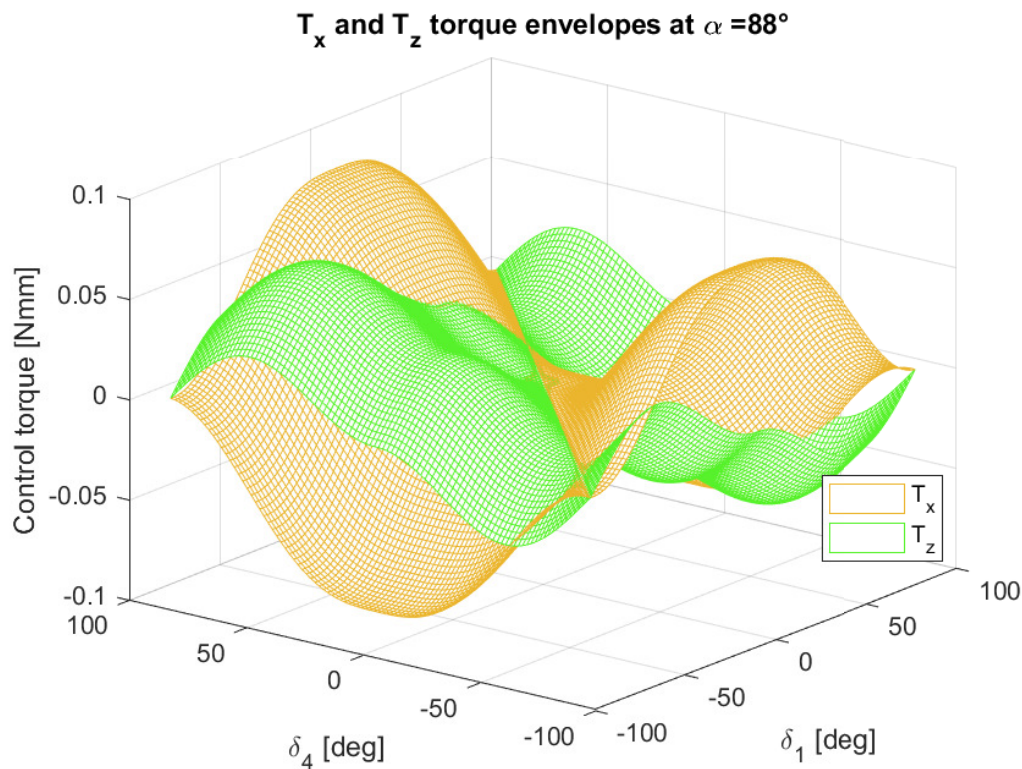
Figure 4.12: Roll and yaw torques overlapped envelopes at $\alpha = 88°$.

While increasing the pitch angle, the conformation of the $\mathbf{T_x}$ roll torque is modified, becoming more similar to the $\mathbf{T_z}$ one. This is, once again, physically due to the $\mathbf{X}_{BRF}$ axis being almost aligned with the sunlight at low pitch, while the $\mathbf{Z}_{BRF}$ is perpendicular to it. While $\mathbf{Z}_{BRF}$ becomes almost aligned itself at high pitch so the situation is reverted. Eventually in Fig. 4.12, where $\alpha = 88°$, the envelope conformations resemble the opposite of the ones at $\alpha = 0°$, in Fig. 4.10. Maths supports this physical intuition, in fact, the weights of the contributions to the $\sin$ functions in Eq. 4.25 are higher at high α, while the ones to the $\cos$ in Eq. 4.26 are higher at low α. A further confirmation comes from Fig. 4.11, where $\alpha = 40°$, there the envelope conformations are akin, underlining the transition from one to the other.

4.6.3 The deflection angle algorithm

The control algorithm, in section 4.7, outputs a set of saturated desired torques. For each of these the system should be able to tell what is the deflection angle set δ_i, with $i = 1, 2, 3, 4$, that generates the aforementioned desired torque. It is essentially a problem of solving the inverse functions of the pitch and yaw/roll torque models. The different models have different levels of complexity due to their properties, therefore different algorithms are used.

Pitch deflection angles

The pitch model is described in Eq. 4.24 and essentially lays out a positive, $\mathbf{M}_3$, and a negative, $\mathbf{M}_2$, contribution to the $\mathbf{T}_y$. This property allows to divide the problem in two parts. The positive and negative contributions are dealt with separately. In fact, if the desired torque is positive, the desired $M_2 = 0 \, \mathrm{N \, mm}$, and a solution is found as:

$$\mathbf{T}_{yDES} = \mathbf{M}_3(\delta_3) \tag{4.28}$$

The opposite happens should the desired torque value be negative. The $\mathbf{M}_3$ dependence on $\mathbf{S}$ is not highlighted since the Sun direction is a constant in the problem of finding the deflection angle. Also, keep in mind the the additional constraint of non-reflective back-side is applied to $\mathbf{M}_3$ as described in subsection 4.6.1.

To find the solution to Eq. 4.28, i.e. a δ_3 that results in $\mathbf{T}_{yDES}$, the *fzero(f(x),x_0)* function form Matlab® [33] is used on the function:

$$f(\delta_3) = T_{yDES} - M_3(\delta_3) \tag{4.29}$$

This set-up makes the problem a rather trivial seek for the root of a nonlinear function with initial guess x_0. The root has to lay within the prescribed interval $\delta_3 \in [-90°,90°]$. It is always sure that a zero of the function in Eq. 4.29 lays within that interval because both of the shape of the envelope, in Fig. 4.9, and of the pitch dependent saturation law. Note how in Eq. 4.29 the vector notation is dropped, it is not needed since the torque is know to act about the Cm around the $\mathbf{Y}_{BRF}$ axis.

Lastly, it is worth pointing out that the problem in Eq. 4.29 has to be solved also for the one M_i which is set equal to zero. In fact, the deflection angle which generates a null torque changes together with the pitch angle α. If there is more than one solution no selection criteria is applied at this stage. The algorithm is free to select whichever solution it converges to first.

Roll/yaw deflection angles

Deriving the deflection angles from a set of desired torques for the roll and yaw axes is more complex than the pitch one. In fact, these torques have equations where the effect of the vane 1 and 4 deflections are coupled, in the sense that each contributes partly to the final result. In this case no particular simplification can be made, therefore the problem is approached in the most general way possible.

Once more, the solution corresponds to finding a couple $\Delta_{RY} = (\delta_1, \delta_4)$ that satisfies the following condition in the best way possible:

$$\begin{cases} T_{xDES} = T_x(\delta_1, \delta_4) \\ T_{zDES} = T_z(\delta_1, \delta_4) \end{cases} \tag{4.30}$$

This essentially corresponds to finding the least possible result for the following differences. Again the vector notation is dropped in this subsection since it is self-evident which torque is applied around which axis.

$$r_1 = T_{xDES} - T_x(\delta_1, \delta_4) \tag{4.31a}$$

$$r_2 = T_{zDES} - T_z(\delta_1, \delta_4) \tag{4.31b}$$

To solve this kind of problem, a simplified nonlinear least square iterative solver, such as the Newton-Gauss [34] method, can be used. In fact, due to the number of unknowns being equal to the number of equations, the Jacobian matrix ($\mathbf{J_r}$) of the residuals is square and can be inverted. Thus, the Δ_{RY} update equation is:

$$\Delta_{RY}^{(k+1)} = \Delta_{RY}^{(k)} - \mathbf{J_r}^{-1} \mathbf{r}(\Delta_{RY}^{(k)}) \tag{4.32}$$

with

$$(J_r)_{ij} = \frac{\partial r_i(\Delta_{RY})}{\partial \Delta_{RYj}} \tag{4.33}$$

Where $\mathbf{r}(\Delta_{RY}^{(k)})$ is the vector $\mathbf{r} = (r_1(\Delta_{RY}), r_2(\Delta_{RY}))$ that describes the differences to minimise calculated with the current set of deflection angles.

The Newton-Gauss algorithm, in the formulation above is an iterative method, it needs an initial guess for Δ_{RY} and a criterion for the maximum number of iteration. Once more, no particular implementation is selected other than an initial guess with both $\delta_1, \delta_4 \neq 0°$ and a number of iterations sufficiently high to make the algorithm converge in all the tested test cases, one hundred. In general, the algorithm can converge to any number but, due to the problem constraint, δ_1, δ_4 are post-processed to obtain $\delta_1, \delta_4 \in [-180°, 180°]$ which is always possible for any angle. The results are displayed in section 5.3.

4.7   Control algorithm

In order to apply any meaningful thrust to a Spacecraft it is necessary to be able to control the direction of the resultant force vector. This is particularly true for a solar sail, where once deployed the thrust and direction are solely dependant on attitude. As mentioned, the orbit dynamics are dependent on attitude themselves, that is why a real control algorithm is ultimately needed to investigate the feasibility of the tip vanes as an effective control hardware.

The dynamic problem, as described in subsection 4.2.3 requires a nonlinear control law to cope with the nonlinear angular velocity coupling that generates from the derivatives expressed in body frame. This control law describes the vector $\mathbf{u}$ which is the time dependant total control torque. Eq. 4.10 with the added control torque vector becomes:

$$[I]\dot{\boldsymbol{\omega}}_B = -\boldsymbol{\omega}_B \times [I]\boldsymbol{\omega}_B + \mathbf{u} + \mathbf{L} \tag{4.34}$$

The selected control law is an unconstrained nonlinear proportional derivative control derived from Lyapounov functions of the position and angular velocity errors [15]. Its aim is driving to zero the body's state error with respect to the reference trajectory. The formulation in the literature is [15]:

$$\mathbf{u} = -K\boldsymbol{\epsilon} - P\boldsymbol{\delta\omega} + [I]\,\dot{\boldsymbol{\omega}}_r - \boldsymbol{\omega}_B \times \boldsymbol{\omega}_r + \boldsymbol{\omega}_B \times [I]\,\boldsymbol{\omega}_B - \mathbf{L} \tag{4.35}$$

Where $\boldsymbol{\omega}_B$ is the S/C angular velocity expressed in body frame, $\boldsymbol{\omega}_r$ is the desired angular velocity also in body frame and the dot notation indicates the body frame derivative. $\boldsymbol{\epsilon}$ is the attitude error defined as the vector part of the quaternion attitude parameter:

$$\boldsymbol{\epsilon} = (q_1, q_2, q_3) \tag{4.36}$$

Moreover K and P are the proportional and derivative gain matrices, their notation is not in matrix form because they are intended to be multiplied by the identity $[3 \times 3]$ matrix. In principle these gains could be selected per axis but precise control tuning is not a pledge of this study. Lastly, $\boldsymbol{\delta\omega}$ is the angular rate difference between desired and actual body frame angular velocities expressed as:

$$\boldsymbol{\delta\omega} = \boldsymbol{\omega}_B - \boldsymbol{\omega}_r \tag{4.37}$$

.

Being the quaternion a non-singular attitude parameter, the control algorithm does not need any further trick when executing. However, it is wise to switch the quaternion set to its alternate one when the scalar part q_0 becomes negative. This makes the control system know about which is the shortest rotation to drive the error to zero. This solution is implemented in the algorithm and it is observed to avoid a number of unwanted quick slews which are harmful for the sail system.

As it is presented in Eq. 4.35 the control algorithm still does not work in the simulation environment. Indeed, the control works on the errors between the Body Reference Frame and the Local Vertical Local Horizon which is inherently not inertial. Thus the need of slightly changing the formulation of $\mathbf{u}$:

$$\mathbf{u} = -K\boldsymbol{\epsilon} - P\boldsymbol{\delta\omega} + [I]\,\dot{\boldsymbol{\omega}}_r - \boldsymbol{\omega}_B \times \boldsymbol{\omega}_r + \boldsymbol{\omega} \times [I]\,\boldsymbol{\omega} + [I]\,\dot{\boldsymbol{\omega}}_{orb} - \mathbf{L} \tag{4.38}$$

Note that a term containing $\boldsymbol{\omega}_{orb}$ is added and that the notation $_B$ is dropped on the fifth term. This can also be seen in subsection 4.2.3, in particular in Eq. 4.9 where the correction for the non-inertial reference frame is applied.

The obtained control law, Eq. 4.38, outputs a vector of torques in BRF which is unconstrained, thus indefinitely and arbitrarily big. Hence the need of a saturation law, it is required to make sure that the control algorithm always outputs a torque which yields to a mechanically feasible vane deflection angle. The introduction of saturation makes it so that the system is no longer asymptotically stable, therefore convergence to an equilibrium point

(on the reference trajectory) is not any more granted. However, the theory does not deny such asymptotic stability. It is common to prove the system's stability through numerical simulations, which was the approach for this model.

No particular gain selection technique is implemented. The only attentions besides system convergence are related to saturation and convergence behaviour. Saturation theoretically imposes upper limits on gains [15], if these are surpassed the selection still requires low enough gains to avoid parasitic destabilising actuation. Convergence behaviour, on the other hand, has to do with how long the system takes to detumble an initial angular velocity, arbitrarily chosen, with norm $|\boldsymbol{\omega}_B| = 0.5\,\mathrm{rad\,s^{-1}}$ while catching the varying reference attitude provided by the steering law (see section 4.3). The selected gains are:

$$K = 1 \tag{4.39a}$$
$$P = 1 \tag{4.39b}$$

4.7.1 Saturation

The spacecraft and control hardware models have clear physical limits in which deflection angles can be achieved. On top of them the Sun's position with respect to the S/C poses limits on what is the force obtainable per each vane within that limited angle span. The control algorithm presented in the previous section is agnostic of those limits, thus a saturation law is needed to model them, i.e. to build into the control algorithm the knowledge about the physical constraints resulting in an accurate representation of the reality. Note that in general the saturation is pitch (α) dependent.

Pitch saturation

The goal when devising a saturation law is to make sure the maximum obtainable torque is effectively the maximum which the system can produce. In this way no system-inherent control capability is lost. In the pitch case this is relatively simple to implement.

By looking at the pitch torque envelope in Fig. 4.9 it is clear how per each α angle there are always a maximum and minimum torques well defined within that envelope. The saturation law is built in a way that uses the derivative of the pitch torque positive or negative equations at a certain α to find the maximum (or minimum) value as in Fig. 4.13. Then it uses that value as an upper or lower limit for the torque requested by the control algorithm. This technique grants that the control algorithm never requires more torque than what the hardware can deliver.

Roll yaw saturation

When considering these two coupled envelopes the definition of the saturation law can not simply be limited to finding the maximum or minimum value for each envelope. In fact, a solution Δ_{RY} has to satisfy at the same time the requested torque on both envelopes so, for
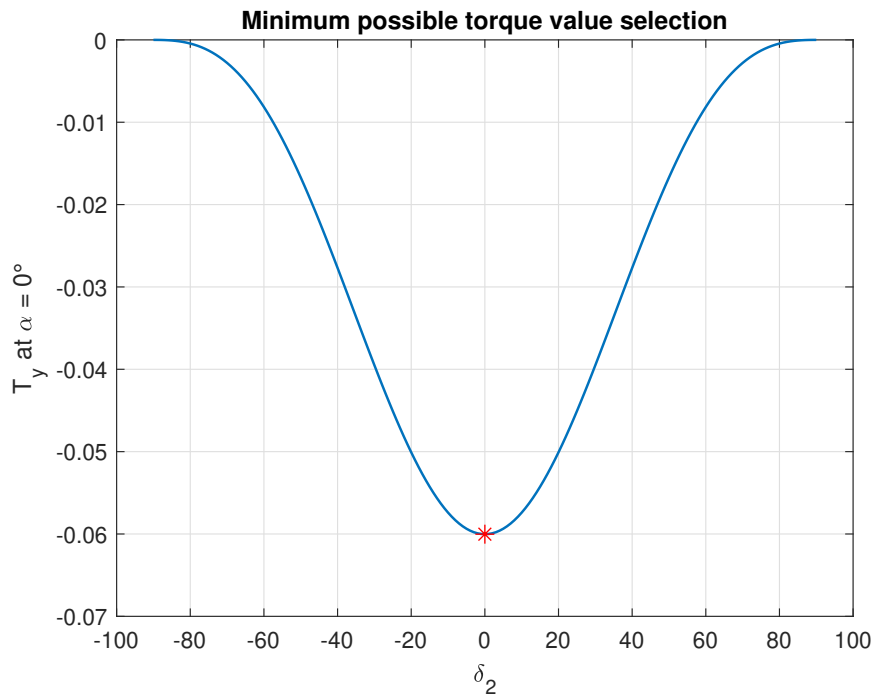
Figure 4.13: Minimum torque value selection for saturation limit at $\alpha = 0°$ and $\gamma = 0°$.

instance, a condition like the two maximum points can never be satisfied. For this reason the implementation suggested in this model is simply a saturation band, or a band within which any torque output from the control system is permitted. Any desired torque outside of this band is limited to the band's maximum or minimum value depending on its sign. The selected values are $[-0.02, 0.02]$ N mm.

Filtering the control torques with a saturation band implies the loss of some control hardware capability as seen in Fig. 4.14, but it is a simple and direct solution. Moreover, the suggested range covers a torque range big enough to provide control for the simulated mission scenario. In order to select the bandwidth of this saturation band, i.e. the range in between the two numbers, several attempts have been performed with the validation tool presented in section 4.8.

One last point to note is that the width of this band has to vary when the inclination angle γ does. In fact, a certain inclination of the sail with respect to the sunlight carries with itself a lower force obtainable from the control vanes. This is built into the saturation band by multiplying its interval margins by a correction coefficient $\chi_{IC}(\gamma)$ that varies with γ as shown in Fig. 4.15. The band thus is defined by $\chi_{IC}(\gamma)[-0.02, 0.02]$ N mm. It can be observed that the inclination correction factor curve, Fig. 4.15, behaves exactly like the squared cosine of the inclination angle, indeed:

$$\chi_{IC} = \cos^2(\gamma) \tag{4.40}$$
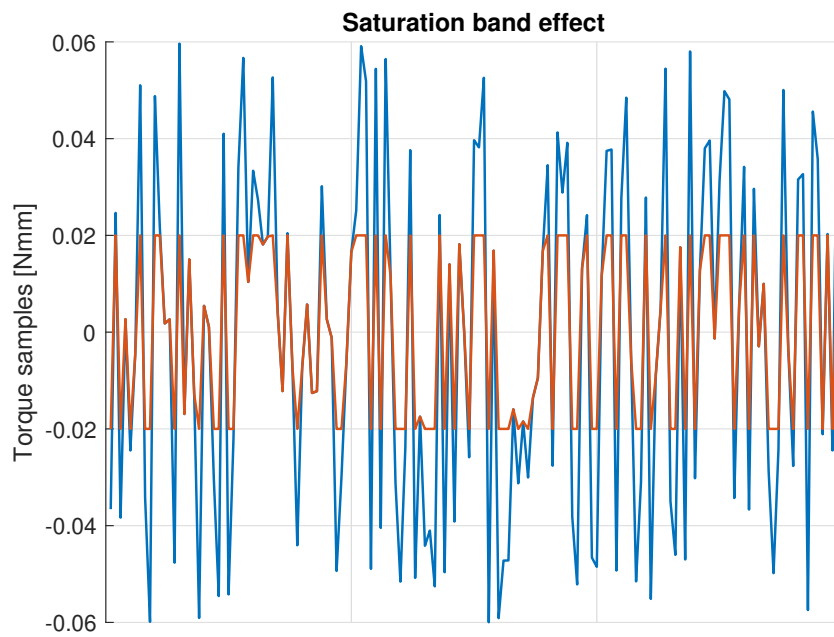
Figure 4.14: Saturation band applied onto randomly sampled torques in the available torques range at $\alpha = 0°$ and $\gamma = 0°$.

Figure 4.15: Inclination correction factor variation with the inclination angle γ.

4.8 Torque validation analysis

For reasons of complexity and computational demand the whole torque model described in section 4.6 is not implemented in the orbital simulation model. On the other hand, the control and saturation algorithms are included. To make sure that the model is representative of the real case, even with this simplification a validation study should be made on the combined torque model and deflection angle algorithm.

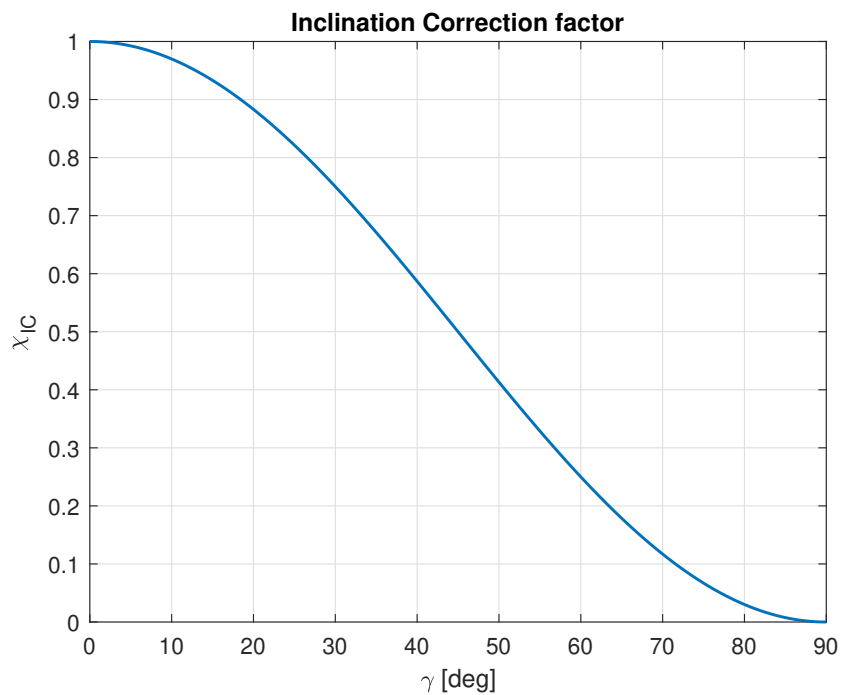The validation technique itself is inspired by the work of M. Choi and M. J. Damaren [35]. A random torque is generated in the range $T_{rnd} \in [\,-0.08,\, 0.08\,]\,\mathrm{N\,mm}$ and acts as desired torque. This T_{rnd} is then passed through the saturation algorithm and trough the deflection angle algorithm which is able to derive the correct deflection angles to obtain $T_{ctrl} = T_{rnd}$. The deflection angle is than used in Eq.4.25, 4.24 and 4.26 to compose the $T_{ctrl} = (T_x, T_y, T_z)$ vector. The relative error per axis between T_{rnd} and T_{ctrl} is then calculated.

This test has been conducted a total of 20 times with different sets of T_{rnd} torques. Other important parameters to specify are the inclination γ and pitch α angles. For each test the solar sail is rotated around its $\mathbf{Y}_{BRF}$ axis of $180°$ in steps of $1°$ covering the whole span $\alpha \in [-90°,\, 90°\,]$. This corresponds to a pitch angle variation, in fact, every time the pitch angle changes a new T_{rnd} is generated, see Fig. 5.10. The inclination angle γ is kept unvaried during the whole test, but each set of $180°$ α is run with inclinations of $\gamma = 0°, 30°, 60°$ and $90°$.

4.9 Disturbance torques

The orbital environment is characterized by the presence of many physical phenomena, unusual on Earth, which influence the performance of a Spacecraft. These phenomena have effects which are very weak in terms of magnitude, but impact the attitude and the motion of the spacecraft. The effects on the on-orbit Cm motion are out of the scope of this study, and are therefore disregarded. However the disturbance torques, which affect the attitude and its control are modelled, particular attention is posed onto the evolution of the disturbances with the increasing sail size. The model is validated through a comparison with the work by Atchison and Peck [3]. In order to select which disturbances to implement in the orbital simulation model a characterization is performed. Lastly, a study on the sail sag, which influences the off-set between Cm and Cp is performed.

4.9.1 Model

Each of the disturbance torques covered in section 2.4 is implemented according to its suggested formulation, more specifically:

- **Gravity gradient:** the first order approximation is implemented according to Eq. 2.26. No other particular simplification is made.

- **Residual magnetic dipole moment:** the implementation is according to Eq. 2.27. The direction of the residual dipole moment $\mathbf{M_{sc}}$ is the worst case scenario one in the simulated orbit. Since the main $\mathbf{B}$ component is in the out-of-plane direction, corresponding with the nominal $\mathbf{Y}_{BRF}$, the residual dipole moment has value $\mathbf{M_{sc}} = 3.5 \times 10^{-3}\,\mathrm{A^2\,m\,kg^{-1}}\,\hat{\mathbf{n}}$.

- **Micrometeoroid collisions:** the implementation is described in Eq. 2.28. It is worth noting that the direction of the $\mathbf{r}_{off}$: the Cm - Cp off-set vector has to be in the sail film plane. It is therefore selected to be $\mathbf{r}_{off} = r_{off}(\,0.0, 0.7, 0.7\,)$ m. Note that this value is constant through the whole study, its magnitude is $r_{off} = 0.025\,\mathrm{m}$.

- **Solar wind:** Eq. 2.32 describes the implemented torque formulation. The off-set vector $\mathbf{r}_{off}$ is as previously mentioned. Moreover, the inverse square distance compensation factor in Eq. 2.33, or $\left(\frac{r_0}{r_s}\right)^2 \approx 1$ no matter the distance from the Sun. This assumption is acceptable since the used $r_0 = 1$ AU, and the highest relative error between the approximated and the non-approximated values along all the simulated orbit is below 1%.

- **Parasitic solar radiation pressure:** this disturbance, direct consequence of the Solar Radiation Pressure on the sail, is formulated according Eq. 2.34. Subsection 4.9.3 is informative about the extent to which the off-set $\mathbf{r}_{off}$ corresponds to a deformed sail.

- **Planetary albedo:** this disturbance is implemented as per Eq. 2.36. Note that this formulation has an attitude invariant albedo radiation pressure, corresponding to an upper bound for this torque.

- **Planetary thermal emission:** similarly to the former disturbance, the planetary thermal emission is implemented using a radiation pressure formulation which is attitude independent, see Eq. 2.40. The resulting disturbance torque is described in Eq. 2.38.

- **Poynting-Robertson drag:** This phenomenon is quite complex to model, and the expected magnitude is comparatively small with respect to the previous ones. However, it is implemented according to Eq. 2.41. Some related value assumptions are made, $T = 255\,\mathrm{K}$ is the selected spacecraft temperature. This because it is the same temperature assumed for Earth surface [3], however no thermal analysis has been performed. The other assumption is $\xi = 0.5$, the S/C thermal emissivity.

- **Eddy current damping:** the eddy current disturbance torque is modelled by Eq.2.43. Its k_e constant assumes a resisitvity $\rho = 1 \times 10^{17}\,\Omega\,\mathrm{m}$ typical of mylar [36], i.e. the assumed sail film material. Keep in mind that this value is temperature dependent, but due to the expected magnitude of the disturbance, even 3 orders of magnitude variations are acceptable therefore this variability is not modelled.

In order to validate the formulation of the disturbances their values are compared with some reference values obtained at $10\,000\,\mathrm{km}$ altitude [3]. The validation analysis is done on the

solar radiation pressure torque, residual dipole moment torque and gravity gradient torque. These are the most important in terms of magnitude, see Tab. 5.3. More specifically, the comparison is done on the angular accelerations produced by the aforementioned torques. These are obtained by [3]:

$$\dot{\boldsymbol{\omega}} \approx \frac{\mathbf{L}}{I} \tag{4.41}$$

Eq. 4.41 implies the assumption $I\boldsymbol{\omega}^2 \ll \mathbf{L}$. Note that to perform this analysis the spacecraft control system is deactivated, in fact, the attitude is always the nominal one as requested by the steering law. See the results in subsection 5.4.1.

4.9.2 Characterization

Subsection 4.9.1 outlines all of the disturbance torques implementations. However, it completely disregards their complexity, in terms of computational burden, with respect to their contribution to the perturbing effect. In order to compute only the essential disturbances at each time step, a characterization process is needed. This allows to assume that some of the disturbing phenomena have little to null effect on the problem at hand. Moreover, the characterization process self-validates the assumptions it allows to make, in the sense that it measures the relative difference in the disturbances with and without the assumptions.

The process consists in running a one-orbit simulation on a reference orbit and measuring the order of magnitude of each disturbance torque. Then these orders of magnitude are compared with the achievable control torque, in fact it is essential that they all are smaller or equal to that in order to grant control of the spacecraft. Next, another one-orbit simulation is performed assuming as zero any disturbance torque which is three or more orders of magnitude smaller than the greatest one. Ultimately, the relative difference between the cumulative disturbances with and without assumption is calculated. The results are in subsection 5.4.2

The reference orbit is a circular GEO with orbital plane corresponding to the ecliptic plane. No Earth eclipse is considered and the control system is deactivated, the nominal attitude corresponds to the S/C attitude at all times. A periodicity is observed in the disturbances during this test, which increases the confidence in the characterization process validity for all the other orbits until SOI escape.

Lastly, attention is posed on the variation of the disturbances with increasing sail size. The reason is that even if this study covers the Sunshade demonstrator, it should be informative also on the more general Sunshade project. In fact, the disturbance torques are evaluated, on the reference orbit, even with a sail size of $A = 9000 \, \mathrm{m}^2$. Besides looking at the order of magnitude of the disturbances with the increased square surface area, this allows to understand their dependence on sail dimensions.

4.9.3   Sail sag analysis

The off-set between Cm and Cp influences the disturbances acting on the sail. This ultimately impacts the sail attitude and control system. The implications of this off-set, naturally present in any sail, are to be found in the disturbance torques, section 4.9. The cause of the off-set, on the other hand, is the deformation to which the sail is subject to when impacted by the photons. Indeed, the real sail film is not perfectly flat as assumed for the SRP model in this study (subsection 4.4.1).

Usually, the Cm - Cp off-set is assumed to be $0.25\,\%$ of the square sail side [13]. This analysis is aimed at relating this percentage to the sag - span ratio of a sail side. More specifically, the sail is assumed to deform with a bi-parabolic shape, i.e. one parabola per sail side. The considered side length is $10\,\mathrm{m}$, therefore the deformation is assumed along the square's side, not the diagonal. Moreover, the sail film is not stretching while deforming. So a certain sail sag corresponds to a tip deflection, as if the spar sustaining the sail film would bend itself. This implies that the sag is defined as the longest vertical distance from a point on the sail and the line connecting centre and tip of the sail (the two extreme points of a sail side). The span is fixed at $5\,\mathrm{m}$, this is represented in Fig. 4.16
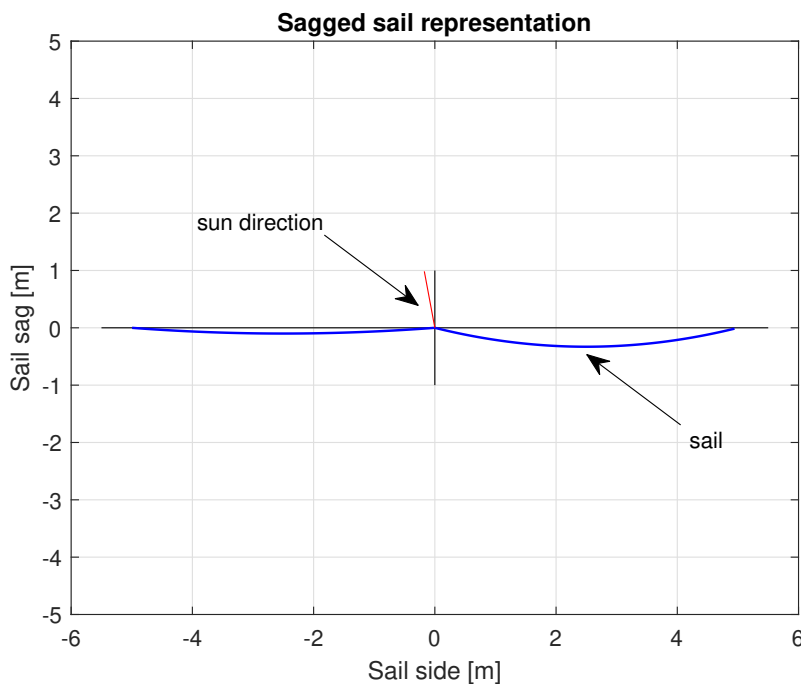
Figure 4.16: Deformed sail representation with Sun direction.

The SRP always generates a force $\mathbf{F_s}$ on the sail according to the model in section 4.5. Note that no billowing nor wrinkling correction coefficients are accounted for in this analysis. If the sail is deformed, the SRP force also generates a moment $\mathbf{M}_s$ on the sail. The moment

arm, which is obtained as in Eq. 4.42 is the Cm - Cp off-set r_{off}.

$$r_{off} = \frac{M_s}{F_s} \qquad (4.42)$$

In order to measure both the moment and the force generated on the sail by the incoming sunlight the sail film is divided in 100 elements, each is a surface $10\,\mathrm{cm}$ wide and $10\,\mathrm{m}$ long, see Fig. 4.17. Sail film thickness is disregarded. The normal of each of these elements is then found and used as the direction for an elemental SRP generated force whose intensity is calculated using Eq. 4.19 with $\chi = 1$ and A elemental surface area. All of the elemental forces are the summed together in their vector form to calculate $\mathbf{F_s}$. The moment is obtained by calculating the vector sum of the elemental moments about the centre of the sail which is fixed in space. Keep in mind that in Eq. 4.42 r_{off} has a sign. In the study it is eliminated but the information contained in it is kept by assigning a side to the off-set.
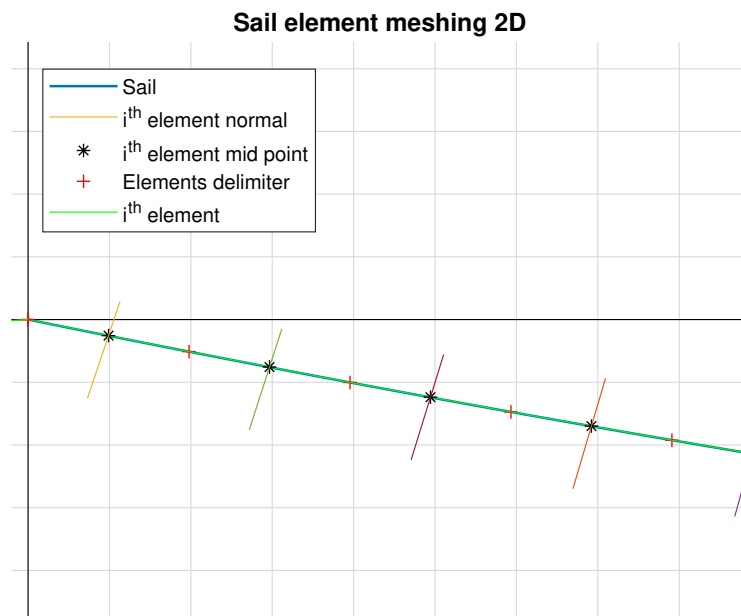

Figure 4.17: Detail of the sail film subdivision in several elements, two-dimensional view. Element normals can also be seen.

The output of this analysis, found in subsection 5.4.3, indicates the variation of the off-set with the percentage of sail - sag ratio. This ratio varies at the same time for both sides of the sail. The Sun direction is also a variable in the problem.

4.10   Eclipse implementation

Most Earth orbits have eclipse regions, this because their trajectories happen to cross the region where sunlight is obscured by the shade cast by earth itself. Thus, eclipse is a common phenomenon for S/C which usually is accounted for as a perturbation on the orbital dynamics. However, since this study covers a solar sail, eclipse becomes relevant, in fact, the tip vanes-based control system can only produce control torques when exposed to SRP. Moreover, the strongest among the disturbance torques listed in section 4.9 depends on the effect of the SRP itself. For this reason a model of eclipse has to be introduced in the simulation.

The eclipse is modelled without a penumbra, so the eclipse shade is modelled as an ideal cylinder [37] whose base diameter is the one of Earth's equatorial circle, $d_E = 12\,742\,\text{km}$. In this full-shaded region the SRP is null. Effects include the lack of control for the S/C and the lack of propulsion together with the reduction of disturbance torques acting on the S/C. The duration of the eclipse, i.e. the time the S/C takes to pass through the cylindrical shade is dependent on the orbital altitude, see results in section 5.5. Furthermore, the eclipse region is always opposite to the rotating Sun with respect to Earth. Note that the choice of a GEO-like orbit inclined as the ecliptic plane implies eclipse at every orbit all throughout the year. This is considered as a worst case scenario for the control system.

The actual implementation of the ideal cylinder is done through angles, this allows to track both the Sun direction and the position on-orbit to have a realistic duration. The angle ϵ is calculated as:

$$\epsilon = 2 \arctan\left(\frac{R_E}{r}\right) \tag{4.43}$$

Where R_E is Earth's radius and r is the S/C position vector magnitude. A region with span ϵ is centered around the direction vector opposite to the Sun direction vector, the S/C is considered in eclipse if it is inside this regions. Fig. 4.18 represents the model.
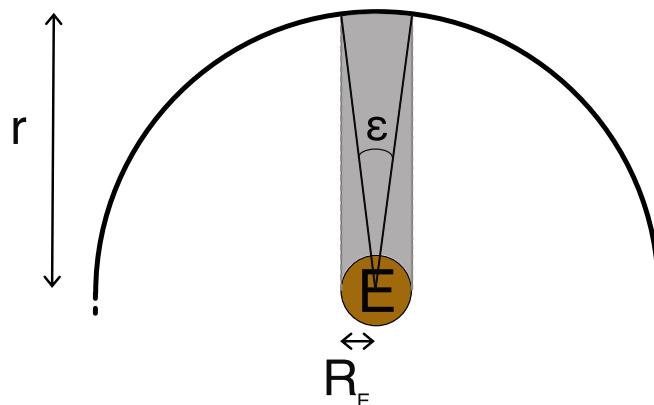

Figure 4.18: Eclipse model representation: Earth, part of the orbit and the definition parameters are shown. Sun is imagined in the bottom part of the image.

4.11 Gyroscopic stability analysis

Section 5.5 shows the effect that eclipse can have on the solar sail if solely controlled by the means of SRP-based tip vanes. In fact, during the eclipse phase no control is applicable and the disturbances spin the S/C up. The control can therfore not withstand the output attitude and angular velocity state at the end of eclipse. This limit is physical, the saturation law imposes a reduced control capability when the spacecraft is inclined in certain ways, see Fig. 4.15. Thus the need of a strategy to stabilize this situation and avoid the degradation of the attitude and angular rate states.

The solution to the problem is a gyroscopic stability induced by a constant spin rate initiated prior to entering eclipse [12]. Note that a rotation around the roll $\mathbf{X}_{BRF}$ axis does not affect the propulsion characteristic since the pitch can be kept constant. It is known that an axis-symmetric body is stable if spinning in torque free motion around its symmetry axis [15]. If a disturbance torque is introduced, the amount of angular momentum accumulated around the spin axis might help to avoid uncontrolled attitude drift. This is particularly true if the disturbance is cyclical in nature, as for example the gravity gradient torque over one orbit [12].

From the general case to the case specific to this study a number of considerations should be made before introducing a spin rate during eclipse. First, the disturbances acting on the S/C during eclipse are various in nature and add up to an irregular pattern. Moreover, the duration of the eclipse is around 5% of an orbit thus making it impossible to see the effects of periodicity of the disturbances in eclipse, since their period is one orbit long. On the other hand, while in the eclipse region there is not control capability, the control system is activated right out of eclipse and its success, being saturated, is not granted. In fact, the success metric for a gyroscopic stability strategy is to reach an eclipse output state which is replicable every time and well conditioned for the control to converge to the desired attitude. As shown in section 5.5 this is not the case if no effect mitigation is performed during eclipse.

The implementation does not require any change to the so-far-described simulation. Indeed, it is enough to change two control parameters dynamically depending on the position on the orbit, which is always known to the system in the simulation. This method is not representative of how this should be implemented in the flying S/C, in that case the two line element propagation is probably the best approach to predict an upcoming eclipse. Based on the eclipse span ϵ, see section 4.10, a pre-eclipse region is defined to be $2°$ larger than the eclipse region. In the pre-eclipse region the reference angular velocity is shifted from $\boldsymbol{\omega}_r = (\, 0, 0, 0 \,) \,\mathrm{rad\,s^{-1}}$ to $\boldsymbol{\omega}_r = (\, 0, \omega_{gyro}, 0 \,) \,\mathrm{rad\,s^{-1}}$. At the same time the K gain is set to zero. In this way the control system focuses on reaching the spin rate disregarding the reference attitude. The value of ω_{gyro} is changed until a good combination is found. Lastly, the choice of extending the pre-eclipse region of $2°$ comes from empirical evidence that it is the least required increase the allows the control system to properly spin the S/C up to the desired spin rate.

Note that to make sure that a good ω_{gyro} can eventually be found, a preliminary analysis is run on a simplified problem. The control-less sail dynamics are analysed with Eq. 4.8, whereas the kinematics are expressed using Euler angles by:

$$\begin{bmatrix} \dot{\theta}_1 \\ \dot{\theta}_2 \\ \dot{\theta}_3 \end{bmatrix} = \frac{1}{\cos{(\theta_3)}} \begin{bmatrix} \cos(\theta_3) & -\cos(\theta_1)\sin(\theta_3) & \sin(\theta_1)\sin(\theta_3) \\ 0 & \cos(\theta_1) & \sin(\theta_1) \\ 0 & \cos(\theta_3)\sin(\theta_1) & \cos(\theta_1)\cos(\theta_3) \end{bmatrix} \begin{bmatrix} \omega_1 \\ \omega_2 \\ \omega_3 \end{bmatrix} + \begin{bmatrix} 0 \\ \omega_{orb} \\ 0 \end{bmatrix} \quad (4.44)$$

The disturbances are summed in the term $\mathbf{L}$ in Eq. 4.8 and are generated from the orbital simulation with the uncompensated eclipse. The simulated time duration time of this analysis is 69 minutes, correspondent to the first eclipse in the orbital simulation. In Fig. 4.19 the S/C $\mathbf{X}_{BRF}$ axis trajectory is bounded and oscillating in a very small angles range. This result is obtained with $\omega_{gyro} = 1 \times 10^{-2}\,\mathrm{rad\,s^{-1}}$ and proves that the process of finding an ω_{gyro} can be successful.
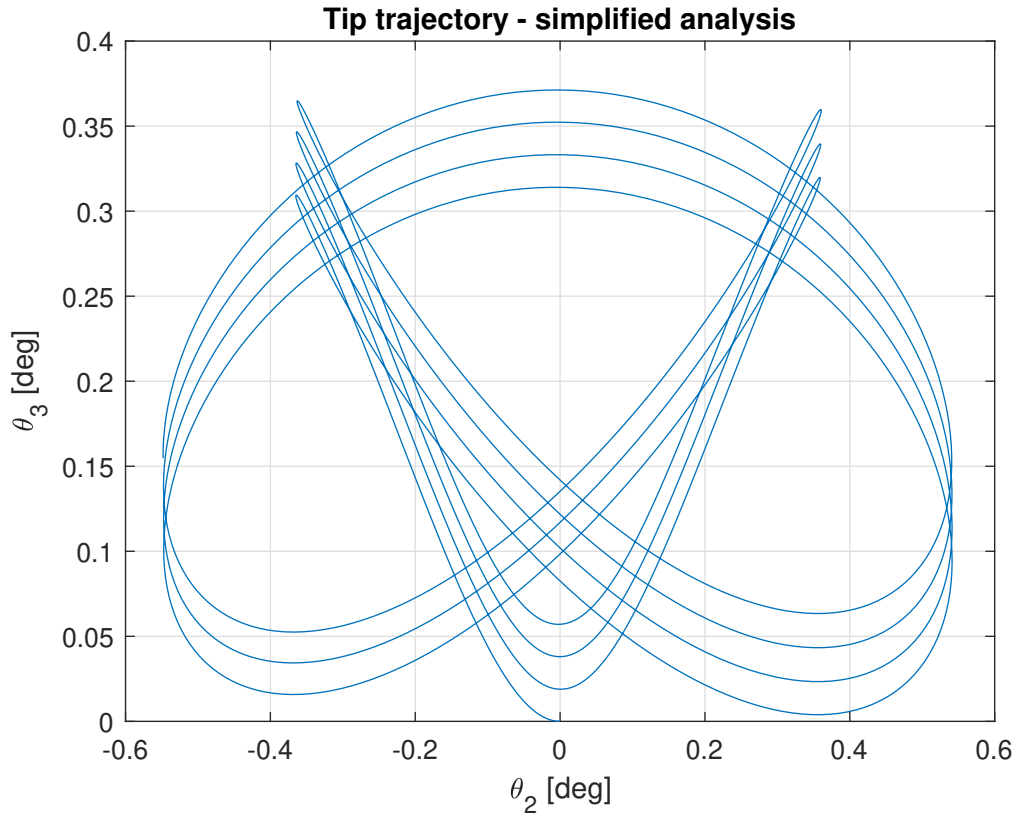

Figure 4.19: Sail normal tip trajectory in the simplified dynamic framework. Initial state is $\theta = [\,0°,\,0°,\,0°]$ and $\omega = [\,1 \times 10^{-2},\,5 \times 10^{-5},\,0]\,\mathrm{rad\,s^{-1}}$.

Chapter 5

Results and Analysis

5.1 Control hardware dimensions

5.1.1 Initial estimation

As a result of the initial estimation for the vanes size a dependency on the required vane area of the overall sail dimensions has been identified in section 4.1. Since the moment of the inertia about the diagonal axis of the system varies more than linearly with the total sail area so does the vane area. This can be seen in Fig. 5.1. The figure also shows, for comparison, the relative dimensions of other designs. Another key information which can be derived from the figure above is the percentage lines. In fact, they show how in general, to obtain a $\dot{\omega}_{\mathbf{B}} = 1 \times 10^{-6} \, \mathrm{rad \, s^{-2}}$ angular rate variation, it is enough to have vanes smaller than 1% of the total sail area. This is why an initial for the rest of the study the vane area is assumed to be $A_v = 1 \, \mathrm{m^2}$, i.e. 1% of the total solar sail area $A = 100 \, \mathrm{m^2}$.

Interestingly enough the result is valid also for a solar sail with $A = 9000 \, \mathrm{m^2}$. However, the two results do not have the same margin. Fig. 5.2 shows how the requirement for the demonstrator architecture is at least $A_v = 0.19 \, \mathrm{m^2}$, or 0.2% of the total sail area, according to the preliminary calculation. Whereas Fig. 5.1 sets the required A_v for the $A = 9000 \, \mathrm{m^2}$ Sunshade S/C just below the 1% line. Thus, for scalability reasons the control vanes surface areas are all initially set at 1% of the total sail area A. The chosen values for the initial vanes size estimation are summarized in Tab. 5.1.

Vane Number	Area [$\mathrm{m^2}$]	Height [m]	Base Length [m]	Q efficiency factor
1	1	1	2	0.85
2	1	1	2	0.85
3	1	1	2	0.85
4	1	1	2	0.85

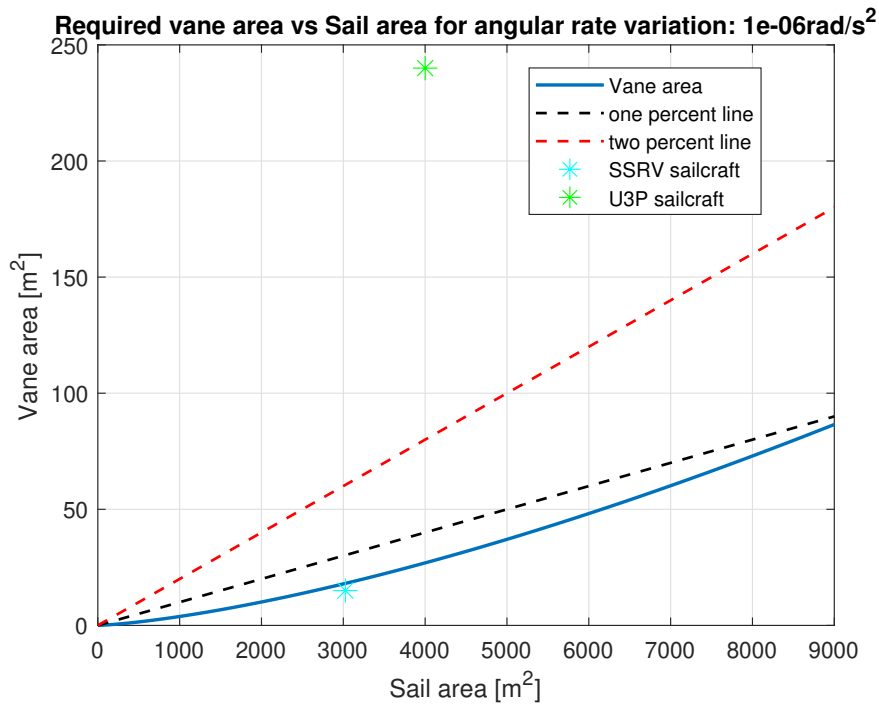Table 5.1: Initially derived vanes dimensional parameters

Figure 5.1: Required vane area as a function of the overall sail area. SSRV and U3P solar sail dimensions and vane areas are reported as well [1]. Note that vanes are estimated to produce an angular rate variation $\dot{\omega} = 1 \times 10^{-6}\,\mathrm{rad\,s^{-2}}$ along the $\mathbf{Z}_{BRF}$ axis.

5.1.2 Final values

Vane Number	Area [m^2]	Height [m]	Base Length [m]	Q efficiency factor
1	1.5	1	3	0.85
2	1	1	2	0.85
3	1	1	2	0.85
4	1.5	1	3	0.85

Table 5.2: Vanes geometrical parameters

Tab. 5.2 lists the final selected values for the control vanes. These are not derived by the initial estimation but are the result of the whole study. The difference is in the vanes' number 1 and 4, i.e. the roll/yaw vanes, their size is increased from 1% to 1.5% of the total sail area A. The main reason behind this change is related to the combined available torque envelope for the control torques around the $\mathbf{X}_{BRF}$ and $\mathbf{Z}_{BRF}$ axes and the saturation effect on it. The saturation constraint using 1% of A vanes is too strict to have a reasonable maximum control torque around the aforementioned axes. This is covered in more detail in subsection 4.7.1. On the other hand, due to their configuration the pitch vanes, 2 and 3, do not need a size increase and perform well across all the simulated test cases.
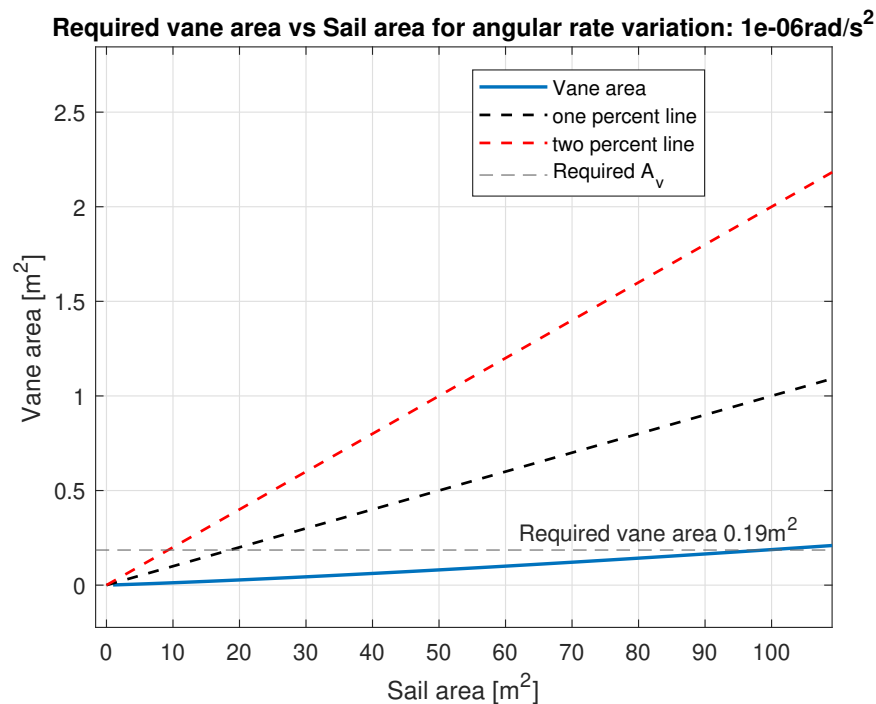
Figure 5.2: Vane area variation with respect to overall sail area. Zoom around the desired demonstrator dimension. The required sail area for the demonstrator is displayed.

5.2 Escape trajectory analysis

The steering law is a key piece in providing an initial set of requirements for the sail's control system. In fact, it describes the desired attitude at each time on the orbit, which is ultimately fed to the control system as a reference. To test the steering law's validity an escape trajectory analysis is performed according to section 4.3. The results are presented and explained here. The most informative indicator about an escape trajectory's performance is the evolution of its orbital energy ϵ, in Fig. 5.3. As mentioned in section 4.3 the S/C is considered to be escaped once $\epsilon = 0$ J. In Fig. 5.3 however the plot is stopped at around $\epsilon = -0.5 \times 10^{-6}$ J because the remainder of the trajectory is almost a straight line thus not being meaningful for the analysis. This latter energy level is referred to as escape for the rest of this section.

The first fact to notice is that the orbit rate trajectory is not as efficient as expected, being de facto the slowest to reach escape. This is simply due to a correction error introduced when the rotating Sun is taken into account. From now on, this steering law will be disregarded and plotted only for completeness. The only important observation related to it is the shape of the curve. In fact, the On-Off switching strategy has a sharp edge that separates the trust on and off parts of the orbit. The orbit rate, on the other hand, has a more evident smoothness as the effect of the energy gain even during the sun-ward part of the orbit. This property can be noticed even in the two optimal trajectories, moreover it is evident also in Fig. 5.5 and 5.4.
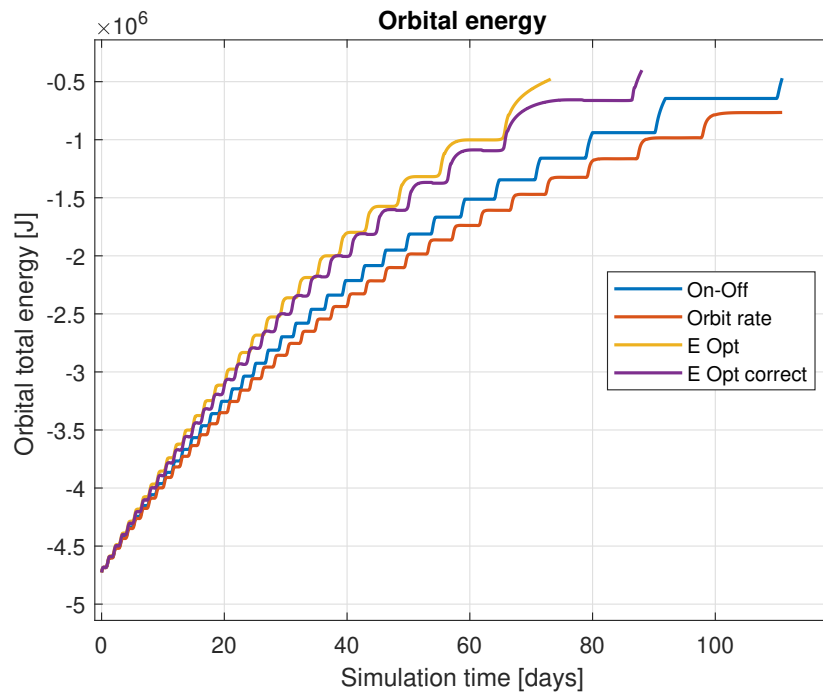
Figure 5.3: Orbital energy from GEO to escape orbit, all escape strategies mentioned in section 4.3 are included.
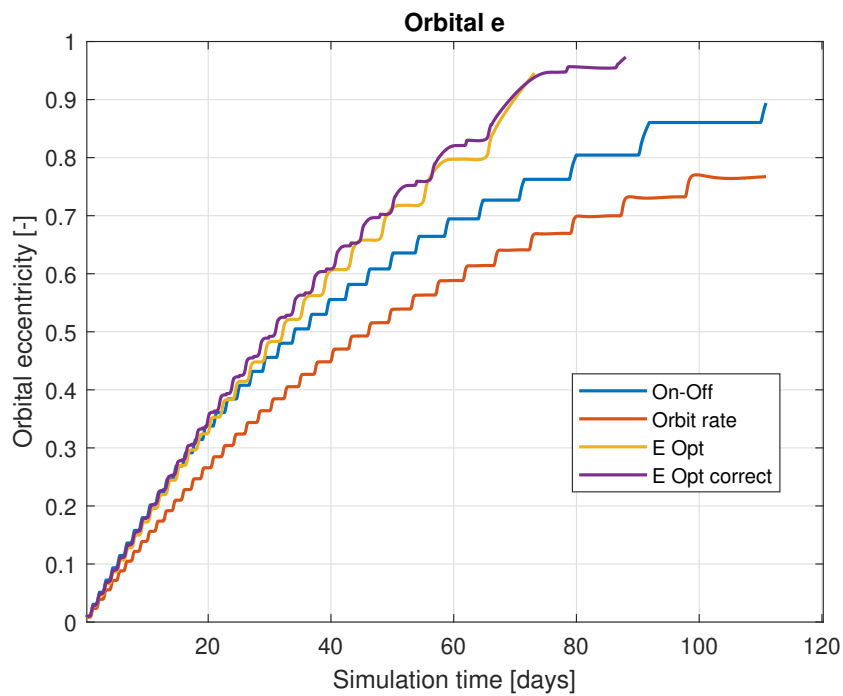

Figure 5.4: Orbital eccentricity from GEO to escape orbit, all escape strategies are included.

It is worth noting how the growth in orbital energy is less than linear in time, this because it is almost negligible for the Sun-ward portion of the orbit, i.e. the line is almost flat. This portion has an increased per-orbit duration as time progresses, due to the increasing eccentricity e. This is why it is fundamental to employ a strategy which increases the energy even during this portion of the orbit. Otherwise a great amount of the trajectory, in terms of time, is effectively useless in increasing the orbital energy. Note in Fig. 5.3 how the time required to escape is reduced by 39 days using the optimal steering law. In general, this increased energy efficiency is due to the larger ζ multiple, reflected in the semi-major axis a growth curve in Fig. 5.5. Remember that ζ is the proportionality constant that describes the per-orbit growth of semi-major axis as a function of the current semi-major axis, see Eq. 2.25. However, the optimal steering results also in a more eccentricity efficient trajectory being less demanding on the control system requirements, see Fig. 5.6 compared to Fig. 5.7. A better e efficiency means a greater increase in a for a certain growth in eccentricity. By comparing the a and e plots at 40 and 60 days the Δ_e increase is 100% whereas the Δ_a is 361%.
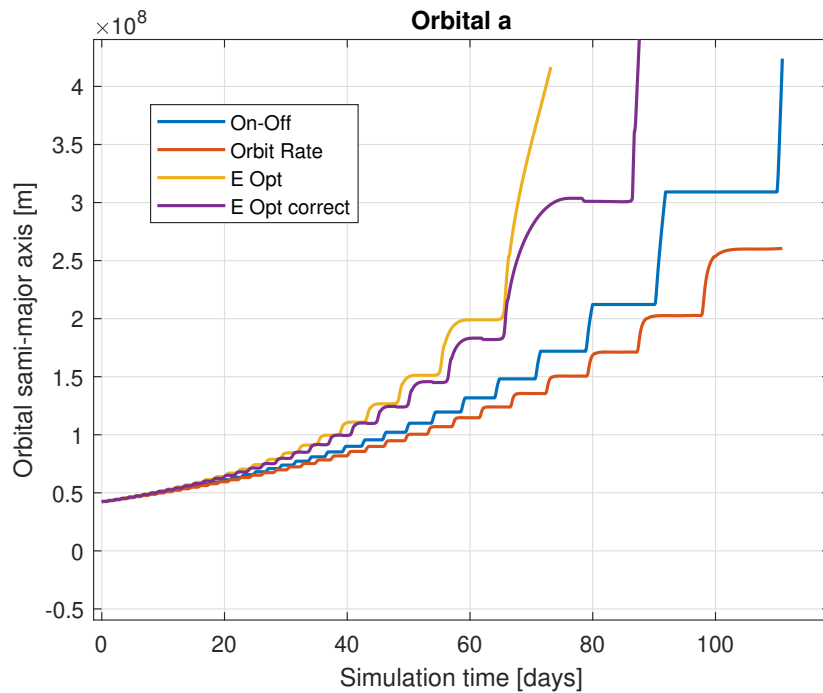
Figure 5.5: Orbital semi-major axis evolution from GEO to escape orbit, all escape strategies are included.

As initially intended, this result justifies the choice of an energy optimal strategy for the steering law. As stated in section 2.3, however, in the real case the pure energy optimal steering law can not be implemented. A correction is needed to cope with the maximum control torque delivered by the system not allowing a sudden rotation. The selected $\alpha_{turn} = 85°$ is obtained by performing several simulation runs with incremental α_{turn} and comparing the escape time as performance metric.

The energy optimal corrected steering law has the built-in drawback of exposing part of the film sail to the Sun in the Sun-ward portion of the orbit. This inherently reduces the orbital energy at that point due to the SRP force being pointed opposite to the velocity. This effect is better seen in the eccentricity plot rather than in the energy one, see Fig. 5.4. It is clear how this reduces the energy efficiency of the escape trajectory. Nevertheless the selected α_{turn} shows good results, in terms of escape time, while accounting for the real rotation with the limited torque available to the control system. The escape time is 13 days longer than the one measured for the non-corrected optimal law.

Lastly, for comparison a detail of the sail's pitch profile with the three analysed trajectories is shown in Fig. 5.8 and Fig. 5.9. Note that the SOI of Earth is much smaller than the distances achieved when reaching the energy level considered as escape here, being at around 1×10^6 km from the centre of earth.
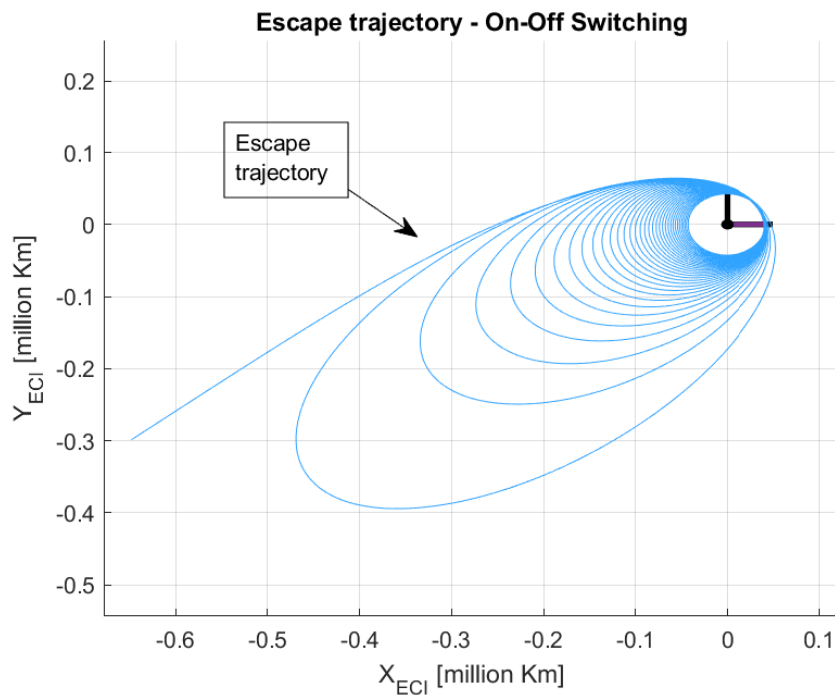
Figure 5.6: Escape trajectory for a standard configuration (see section 2.3), On-Off switching steering law.

5.3 Torque validation analysis

Results form the torque model and deflection angle algorithm validation are displayed below. Keep in mind that even if 20 runs have been performed at different inclinations only the results from one run are presented, with inclination angle $\gamma = 30°$. This because of similarity

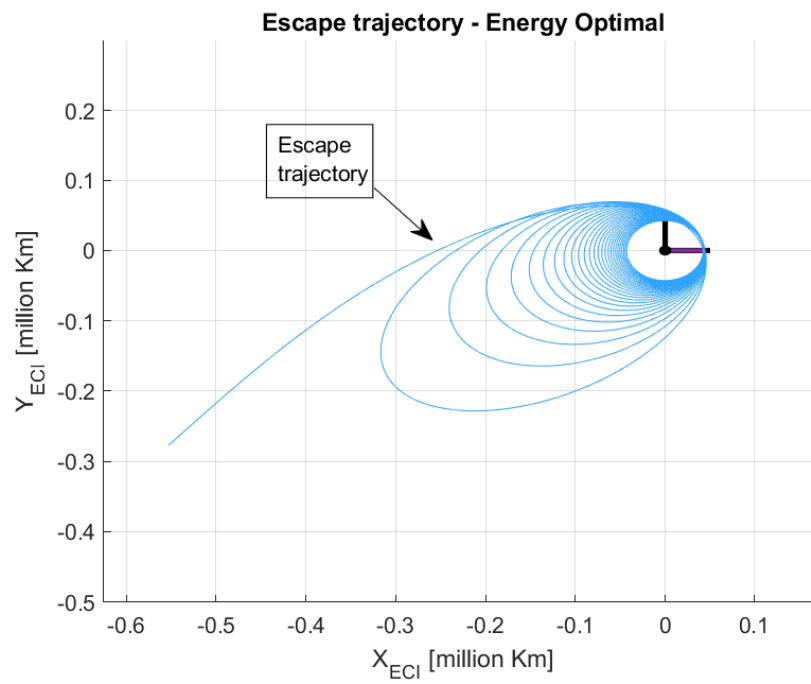Figure 5.7: Escape trajectory for a standard configuration (see section 2.3), Energy optimal steering law.
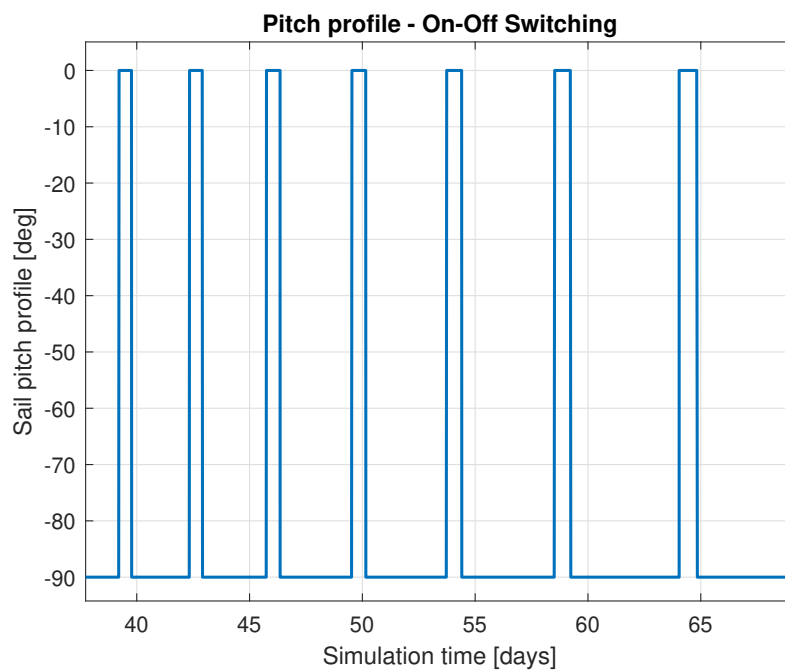

Figure 5.8: Detail: sail attitude pitch profile, On-Off switching steering law. The increased gaps are due to the increasing orbital a.
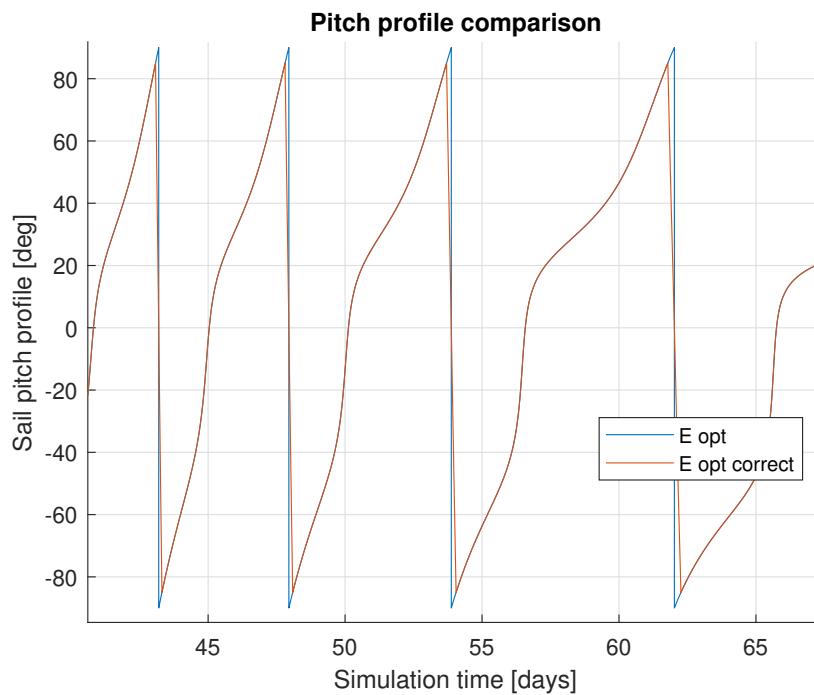
Figure 5.9: Detail: sail attitude pitch profile comparison, Energy optimal and corrected energy optimal steering laws. The change in the curve's steepness in the periodicity are due to the changing orbital shape.

between them, in terms of the observed relative errors, thus the loss of informative validity of repeated results.

The first output of the torque validation analysis, in Fig. 5.10, shows the actual randomly generated torques T_{rnd}, i.e. the desired torques from the deflection angle algorithm perspective. The model used to perform the analysis includes the saturation laws in order to account for physical vane deflection limits. Note here how the saturation law has the form of a band along the $T_{rnd}x$ and $T_{rnd}z$ components, as per subsection 4.7.1. On the other hand, the saturation on the $T_{rnd}y$ component is more selective and permits a larger and variable span of the desired torque.

The desired saturated torque is then given as input to the deflection angle algorithm which finds the appropriate δ_is to minimize the relative error between T_{rnd} and T_{ctrl}. This corresponds to finding the deflection angles per each vane that control the system. It is important to notice that both δ_1, δ_4 and δ_2, δ_3 respectively in Fig. 5.11 and Fig. 5.12 do not exceed the physical deflection limits indicated by the horizontal dashed lines. In fact, this means that the algorithm is able to control the system and that the hardware can cope with it. Another indication of proper algorithm functionality is the curve trend in Fig. 5.12. Indeed, δ_2, δ_3 generally converge in a neighborhood one of the other, meaning that the algorithm converges in points of the torque's envelope, Fig. 4.9, that are the furthest

from zero. Moreover the quasi-linear progression of the solutions is sensible, it follows the
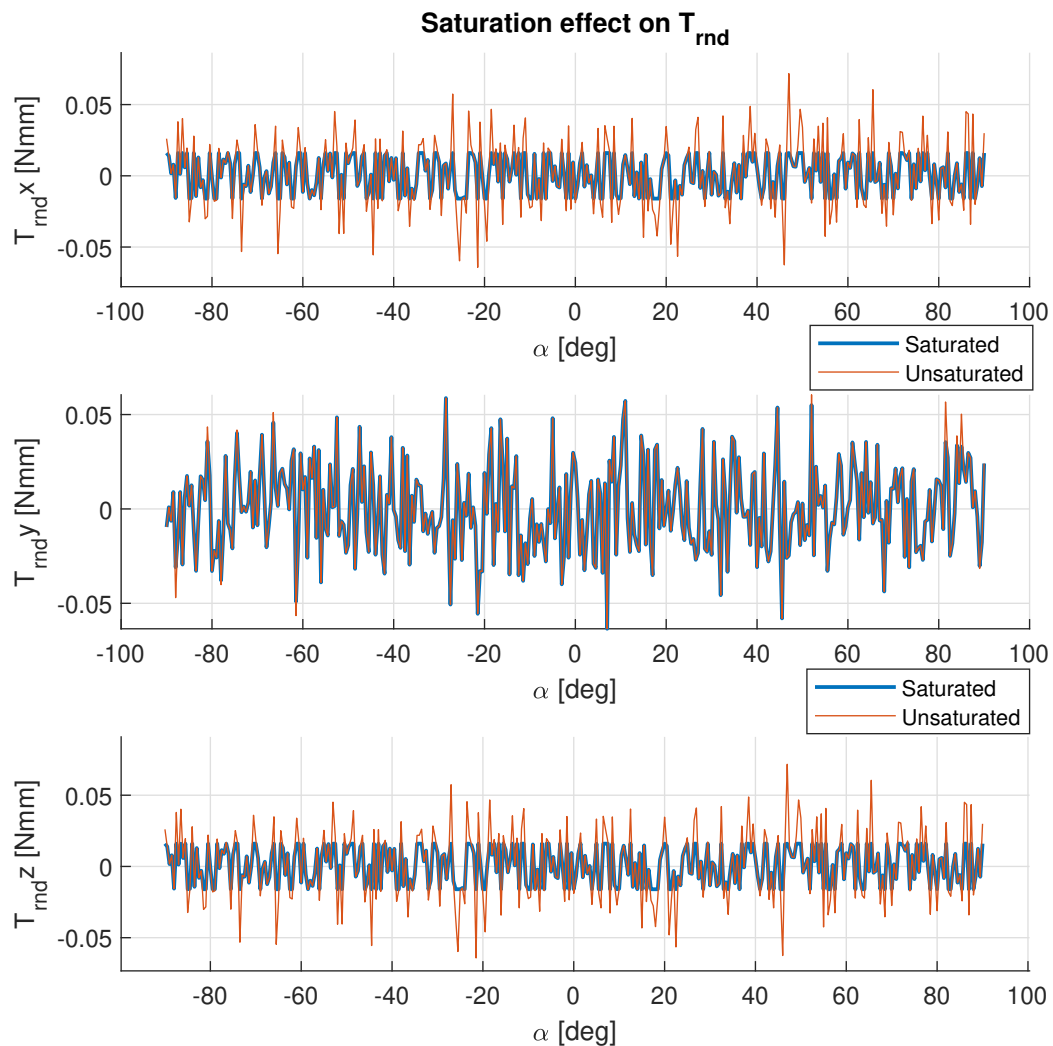
Figure 5.10: T_{rnd} as generated with superimposed T_{rnd} after saturation.

α variation on the envelope. The same can not be said of the yaw and roll vanes deflection angles, but due to the different topology and definition of the corresponding envelope that does not give any insight on the algorithm's sanity.

In Fig. 5.13, 5.14 and 5.15 the relative errors per component can be seen. These are the result of the torque validation analysis. Note the orders of magnitude of the errors, all approximately around $10^{-10}\%$. That resolution is about the algorithm's own mathematical imprecision. In particular, Fig. 5.14 which displays the relative error of the $\mathbf{Y}_{BRF}$ component is three orders of magnitude lower than the others, in fact the computational burden on the pitch algorithm is lower, hence the lower relative error. No particular reason is found behind
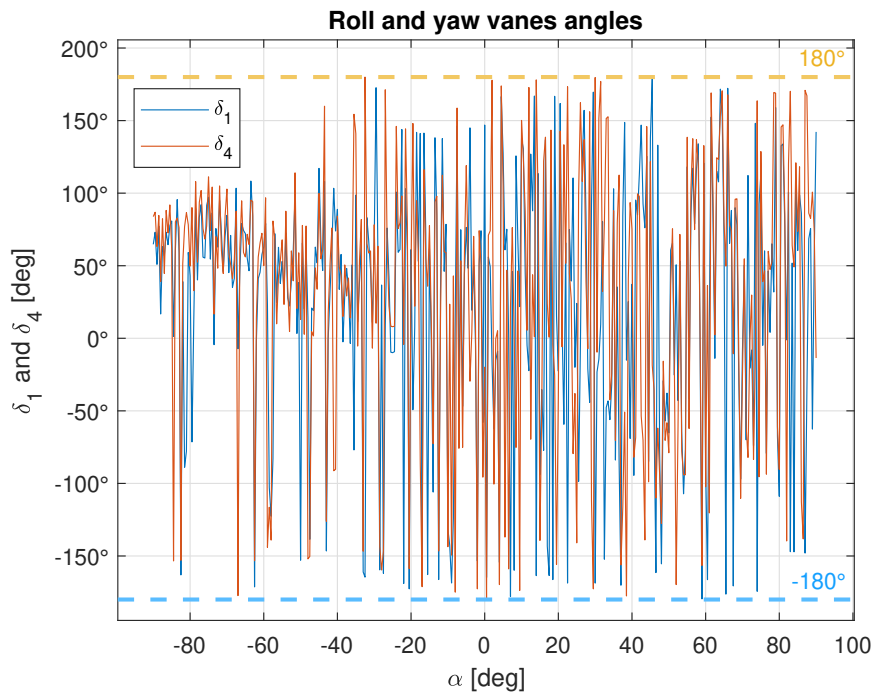
Figure 5.11: δ_1, δ_4 obtained for the torques in Fig. 5.10 at $\gamma = 30°$.
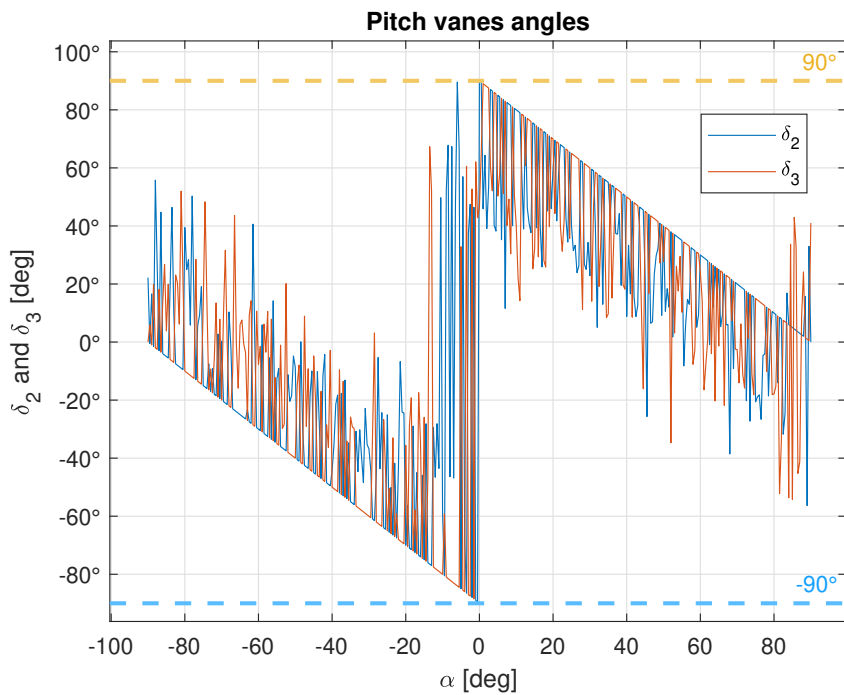
Figure 5.12: δ_2, δ_2 obtained for the torques in Fig. 5.10 at $\gamma = 30°$.

the peaks in the figure other than random convergence error related to the aforementioned algorithm precision.
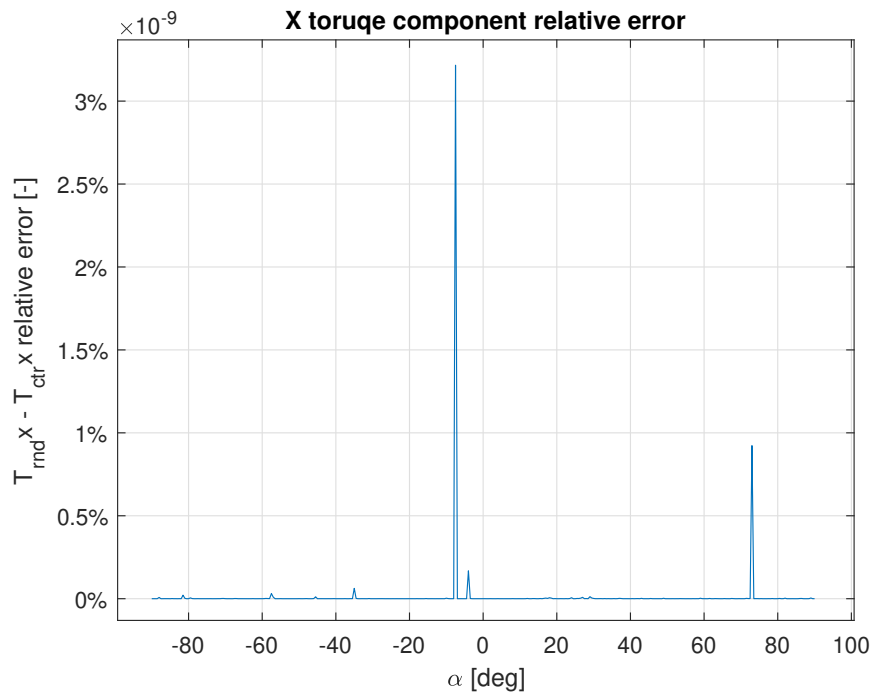
Figure 5.13: Relative error between $T_{rnd}x$ and $T_{ctrl}x$ obtained with the deflection angles angles in Fig. 5.11.
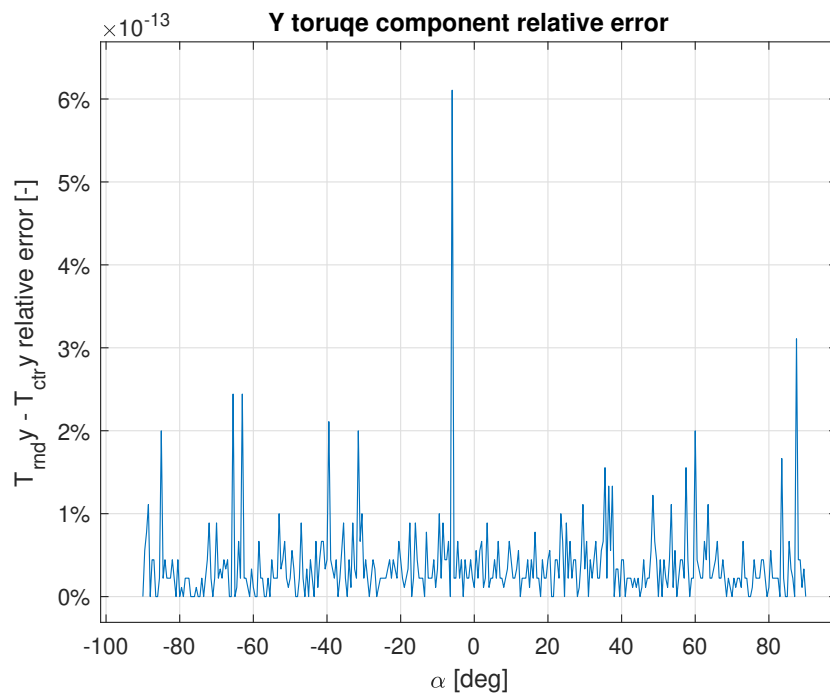
Figure 5.14: Relative error between $T_{rnd}y$ and $T_{ctrl}y$ obtained with the deflection angles angles in Fig. 5.12.
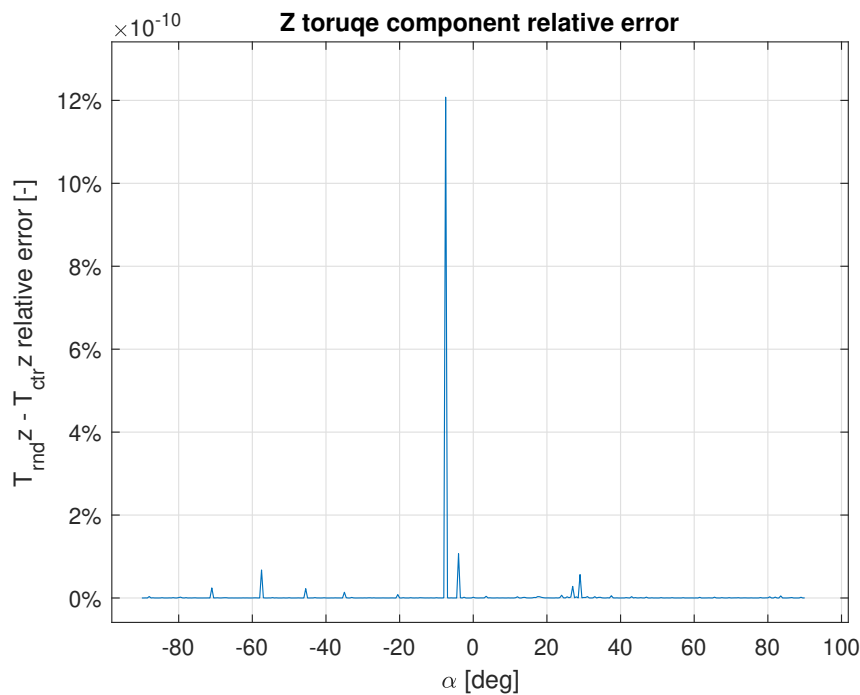
Figure 5.15: Relative error between $T_{rnd}z$ and $T_{ctrl}z$ obtained with the deflection angles angles in Fig. 5.11.

5.4 Disturbance torques assessment

5.4.1 Comparative validation

The disturbance torques validation, at $10\,000\,\mathrm{km}$ altitude in Fig. 5.16 yields promising results. In fact, it confirms that the formulation used for the solar radiation pressure parasitic, the residual dipole moment and gravity gradient torques is according to literature [3]. In particular, in Fig. 5.16, MR indicates the magnetic residual torque, corresponding to the residual dipole moment. On the other hand, SP stands for Solar Pressure, short for SRP and GG, intuitively, for gravity gradient. Note that the compared values match almost exactly except for the GG. This, however, is only less then an order of magnitude away form its correspondent literature value.

5.4.2 Disturbance torques characterisation

The results from the one-orbit run along the reference orbit described in subsection 4.9.2 are presented in Tab. 5.3. Note that these values correspond to a sail surface area of $A = 100\,\mathrm{m}^2$. The most disturbing effect is produced by the parasitic SRP. In fact, this is a direct consequence of the sail performance measured by the lightness number β, efficiency in film reflective properties and sail ensemble construction straighten the force produced by the sail together with its parasitic component. Nevertheless, all of the orders of magnitude in Tab. 5.3
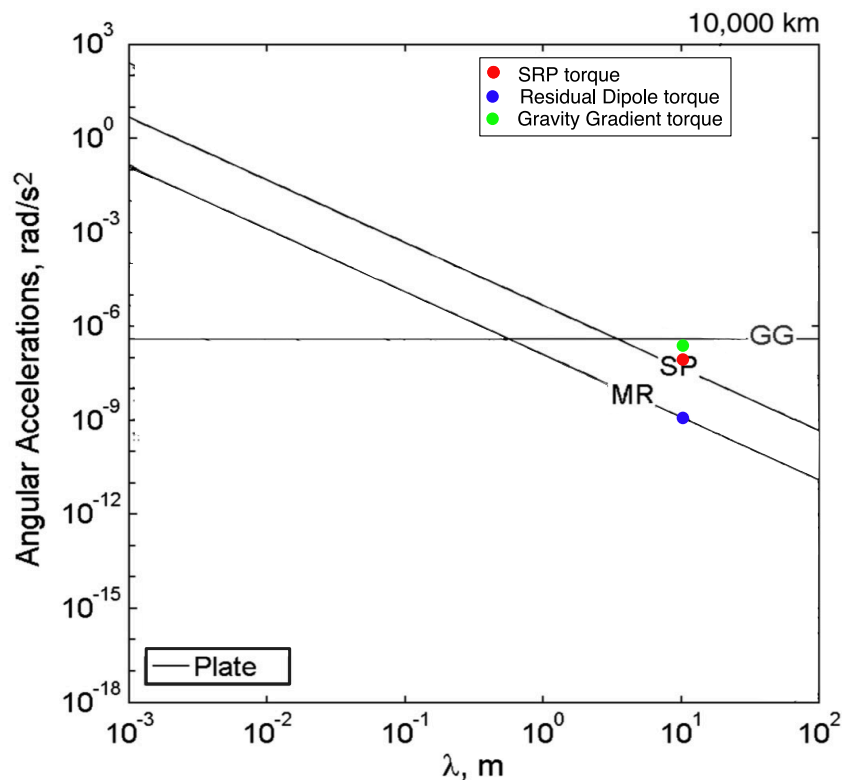
Figure 5.16: Atchison and Peck angular accelerations for disturbance torques at $10\,000\,\mathrm{km}$ [3] compared to obtained results with the formulation in section 4.9. On the horizontal axis λ is the side length of a square sail.

are lower or equal to the nominal control torque. The ability of the control system, hardware and algorithm, of controlling the S/C is confirmed.

The other major disturbance components are the gravity gradient torque, expected due to the large sail structure inertia, the planetary albedo torque and the thermal emission one. These two are also generated by means of radiation interacting with the sail, hence the efficency in converting partcles momentum in a propulsive force becomes problematic. It does so by means of the Cm - Cp off-set $\mathbf{r_{off}}$, the bigger $\mathbf{r}_{off}$ the bigger the disturbance.

Worth noting is also the eddy current damping torque. Its magnitude is several orders of magnitude smaller than the others. This is a consequence of the extremely high mylar resistivity. Keep in mind that the sail film is not only constituted of mylar in the real case. This might affect the magnitude of the eddy current disturbance, however, since it is modelled as an upper bound assuming the whole sail film area is a current loop, the assumption of disregarding it in the simulation is considered valid.

Lastly, the criteria with which it is decided whether or not to neglect the torques in the simulation model is to neglect any torque smaller $10^{-8}\,\mathrm{N\,m}$. This is indicated in the third column of Tab. 5.3.

Source	Order of Magnitude [N m]	Accounted for
Gravity Gradient	10^{-7}	✓
Residual Dipole Moment	10^{-9}	X
Micrometeoroid Collisions	10^{-11}	X
Solar Wind	10^{-11}	X
Parasitic Solar Radiation Pressure	1×10^{-5}	✓
Planetary Albedo	10^{-8}	✓
Planetary Thermal Emission	10^{-8}	✓
Poyinting-Robertson Drag	10^{-12}	X
Eddy Current Damping	10^{-30}	X
Nominal Control Torque	$2 \text{ - } 6 \times 10^{-5}$	✓

Table 5.3: Disturbance torques sources and orders of magnitude over the standard comparison orbit for a $100\,\mathrm{m}^2$ demonstrator sail.

A comparison between the total disturbance torque and the relevant disturbance torques, i.e. the ones ticked as accounted for in Tab. 5.3, shows that the assumption of neglecting the torque values below $10^{-8}\,\mathrm{N\,m}$ is sustainable with differences well below 1%. This can be seen in Tab. 5.4, note that for the X axis the absolute error is used instead of the relative error. This because the component of the accounted for disturbance torque on the X axis is close to zero therefore the relative error is almost 100%. However in this way the absolute error makes sense, in fact it indicates directly the torque component that is being neglected.

Absolute error X axis	Relative error Y axis	Relative error Z axis
10^{-11}	0.02 %	0.1 %

Table 5.4: Error parameters to compare the total disturbance torques with ones considered relevant.

To be informative for the Sunshade project, as well as for the demonstrator S/C design, results are shown also for the $9000\,\mathrm{m}^2$ Sunshade sail in Tab. 5.5. The attitude control torque order of magnitude for that full size solar sail is $10^{-2}\,\mathrm{N\,m}$ in a sun-facing attitude. This indicates that the S/C can be controlled over-weighing the disturbances as it was for the smaller sail size. The increase in order of magnitude is consistent throughout all of the disturbances but the residual dipole moment torque and eddy current damping torque. The reason is that all of the surface dependant disturbances grow two orders of magnitude because of the area increase and one because of the offset increase. The same goes for the gravity gradient torque, however, in its case the three orders of magnitude are brought by the growth in inertia. On the other hand, the residual dipole moment grows one order of magnitude because it is scaled with the mass. Lastly, the eddy current damping grows five orders of magnitude, two with the area and three with the current loop radius. For confirmation about the dependencies of each disturbance refer to section 2.4.

Source	Order of Magnitude [N m]
Gravity Gradient	10^{-4}
Residual Dipole Moment	10^{-8}
Micrometeoroid Collisions	10^{-8}
Solar Wind	10^{-10}
Solar Radiation Pressure	1×10^{-2}
Planetary Albedo	10^{-5}
Planetary Thermal Emission	10^{-5}
Poyinting-Robertson Drag	10^{-9}
Eddy Current Damping	10^{-26}
Nominal Control Torque	$2\text{-}6 \times 10^{-2}$

Table 5.5: Disturbance torques sources and orders of magnitude over the standard comparison orbit with a $9000\,\mathrm{m}^2$ sail.

5.4.3   Sail sag analysis results

If the sail film deforms as per Fig. 4.16, in a bi-parabolic manner, the right and left side sags have a combined effect on the Cm - Cp off-set. The sunlight direction is relevant as well, both in terms of off-set variation and maximum values.
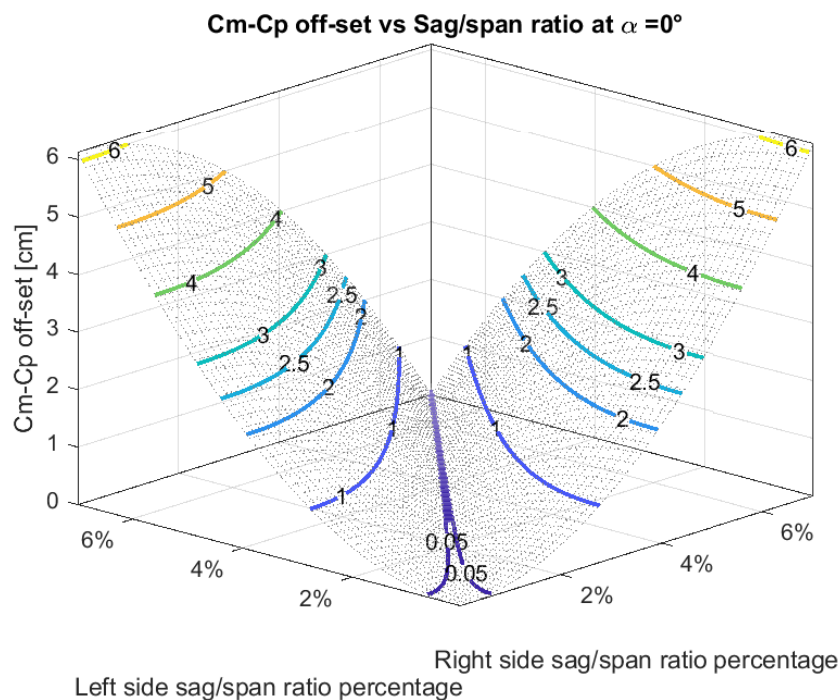

Figure 5.17: Cm - Cp off-set variation with sail sag ration on the right and left side of a bi-parabolic deformed square sail. Pitch angle $\alpha = 0°$.

At $\alpha = 0°$ the sunlight comes perpendicularly with respect to the sail. This results in a

zero off-set line whenever the sag to span ratio is equal on both sides, as per Fig. 5.17. In the same way it grows symmetrically, on the right and lefts sides, almost proportionally to the sag - span ratio. Note that the off-set is on the same side the deformation is on. It is worth highlighting the $2.5\,\text{cm}$ off-set lines, this is the value corresponding to the $0.25\,\%$ of the $10\,\text{m}$ sail side. At $\alpha = 0°$ this reference value is obtained with a sail to sag ratio of $4\,\%$ if the deformation is only on one side. This, on a $5\,\text{m}$ wide side corresponds to an absolute sag of $20\,\text{cm}$. Lastly, note the bend in the contour plot lines, they indicate that when the sag grows on one side, increasing the sail deformation, the other side one has to grow as well if the off-set is maintained constant. This is sensible since the sunlight is perpendicular to the sail.

At $\alpha = 8°$ in Fig. 5.18, even if low, the inclination of the sunlight becomes relevant. The zero off-set region is shifted towards the left, since the pitch angle is positive. This is due to the inner elements of the right hand side tendency to align with sunlight, together with the outer ones of the left side. The elements which are aligned with the sunlight do not generate a significant force. For this reason, the moment generated by the right side is greater than the left one, since the elements contributing to it, the external ones, have a longer moment arm. Because of this, the same sag - span ratio on the right side produces a higher off-set with respect to lower α. This effect is even more evident at higher pitch angles, to the point that at $\alpha = 15°$ the zero pitch region is not in the considered off-set interval. See this effect in Fig. 5.19.

In Fig. 5.19 it is clear that an off-set is generated by the inclination of the incoming sunlight, i.e. by the pitch angle. In fact, this off-set is present even at sag - span ratio close to $0\,\%$ but its value is small in the vicinity of of that point. Note the purple contour dot signifying zero almost correspondent to the X and Y axes crossing. One more thing to underline is the maximum off-set value in the range of considered sag - span ratios. This value increases with α for the reason explained above.

5.5   Eclipse model

This section is aimed both at showing the outcome of the eclipse model, and understanding its effects. First, notice how the eclipse duration changes over a year time of simulation in Fig. 5.20. The absolute duration of eclipse increases from 69 minutes to 93 in a year time, since the growing orbital size imposes the S/C to move slower. Note that the attitude in this simulation is corrected from the eclipse perturbation (described below) in order to have a nominal growth. On the other hand, the percentage of the eclipse duration on the current orbit diminishes over time. These trends are sensible since the eclipse occurs always in the second quarter of orbit, where the S/C is further away from earth at every orbit. The two curves trends also match, in fact, initially the orbital period is increased closely to how much the S/C velocity in eclipse is reduced. Hence, the percentage duration is almost flat. Then the duration in time is more flat, but it still increase more than the velocity decreases, thus

Figure 5.18: Cm - Cp off-set variation with sail sag ration on the right and left side of a bi-parabolic deformed square sail. Pitch angle $\alpha = 8°$.
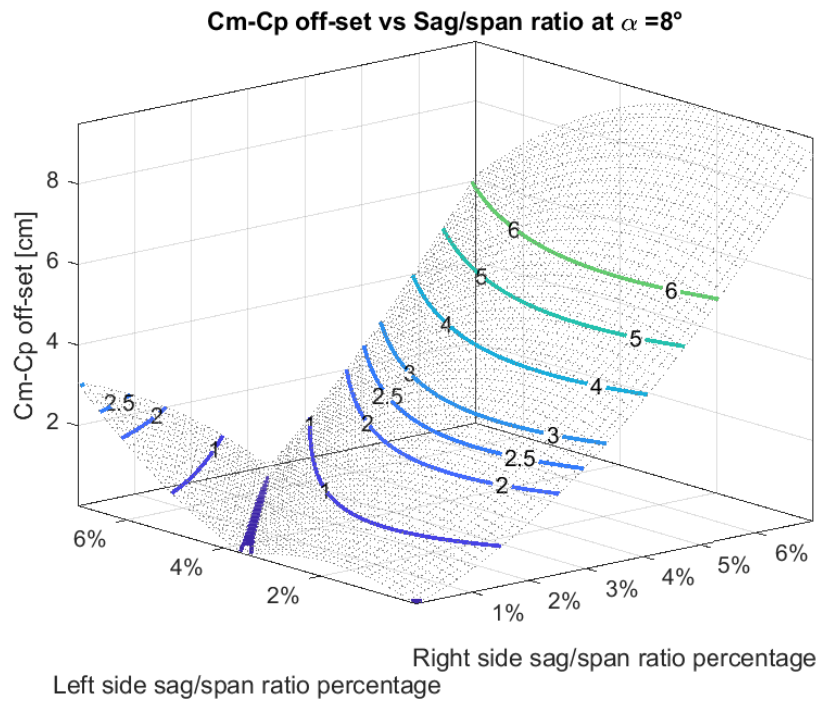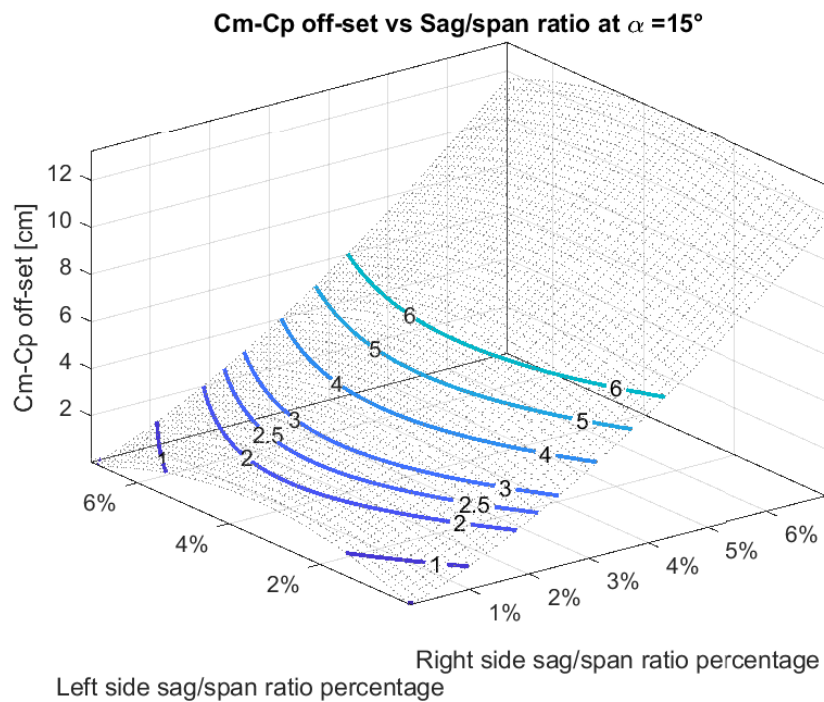

Figure 5.19: Cm - Cp off-set variation with sail sag ration on the right and left side of a bi-parabolic deformed square sail. Pitch angle $\alpha = 15°$.

the percentage duration drops. The explanation for this is to be found in the eccentricity over one year time in Fig. 5.21.

In the first half of the year, the eccentricity grows steadily, and so does the eclipse duration parameters trend. Then at half orbit the curve has an inflection point and starts decreasing. This is due to the raising of what initially was the perigee in what is a circularization maneuver. There the S/C is able to move along the orbit quicker while the orbital period has a reduced increase due to the circularization. Notice how the eclipse duration and eccentricity curves behaviours match, but the first is more compressed since the orbital period increases and a single orbit takes more than one day to occur.
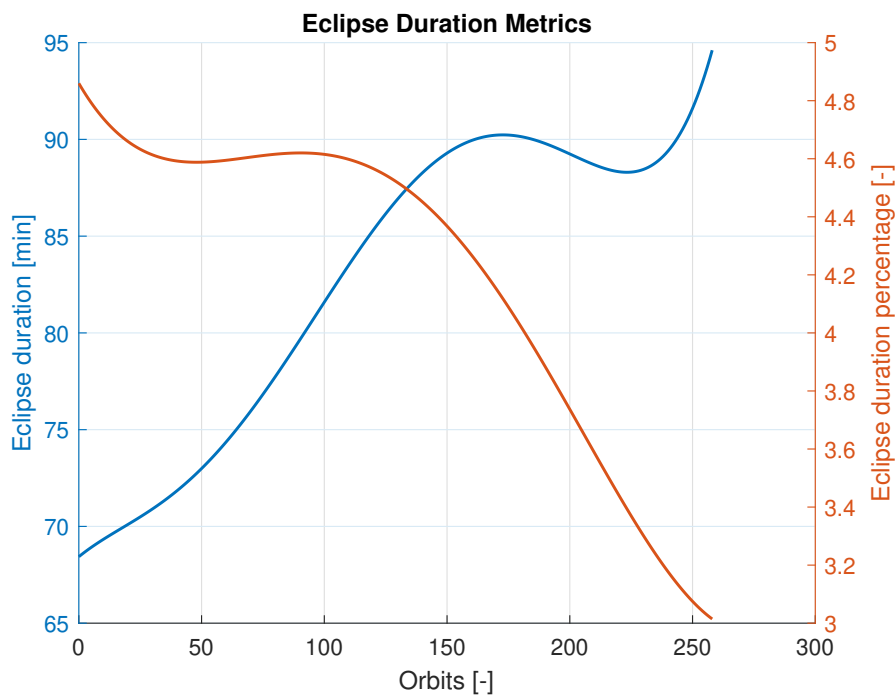
Figure 5.20: Eclipse duration and percentage of current orbit along a one-year simulation. The trajectory is corrected to ensure proper orbit raising.

The effect of eclipse is understandable from Fig. 5.22 and Fig. 5.23, these are the results from a two-orbits simulation run without correction for eclipse attitude perturbation. In the first one eclipse is marked by darkened sections. In general the S/C angular velocity is perturbed during eclipse, where no control is acting while the disturbances still steer the sail. This leads to a situation which the control system, with the saturation limits imposed by its size, has a hard time recovering. Notice how the spikes in angular velocity actually increase in size rather than reducing themselves initially, because the control is incapable of stopping the rotation triggered by eclipse. In the first orbit, convergence to the desired attitude is eventually reached, see also Fig. 5.23, but it is a matter of chance. An orientation where control is sufficient to stop the rotation is reached in the tumbling, but this doesn't prove (not

Figure 5.21: Orbital eccentricity evolution over a year long simulation.

even numerically) the system's stability. Indeed, in the second orbit control is lost, and the system does not converge to a stable state a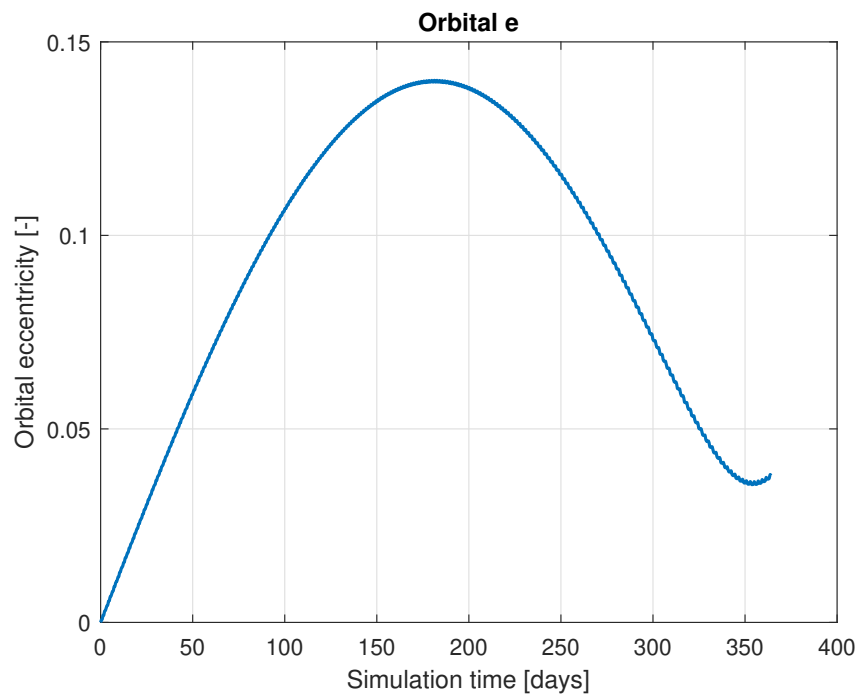ny more. Fig. 5.23 support this finding by showing how different the pitch angle profile for the real attitude with respect to the desired attitude one. It is clear where eclipse start, moreover, one can notice that pointing requirements can not be met in any way. This suggests the need for a gyroscopic stability, or spin stabilisation, during eclipse as described in section 4.11.

5.6 Gyroscopic stability analysis results

The process of finding an ω_{gyro} leads to a successful gyroscopic stability strategy if it results in a replicable and well-conditioned-for-the-control eclipse output. Indeed, if these conditions are satisfied the system's stability is proven numerically. Empirically, the obtained value is $\omega_{gyro} = 1 \times 10^{-4} \, \mathrm{rad \, s^{-1}}$, keep in mind that the analysis' resolution is one order of magnitude. Fig. 5.24 shows the trajectory of the sail normal's tip during eclipse, both with and without the gyroscopic stability strategy. The displayed results are for two consecutive orbits, for ease of display, the long term consequences are discussed in words. In both cases the trajectory during eclipse is the same one orbit after the other. So in principle the replicability of the output state would be granted even without the induced spin rate. This, however, is true only at the beginning of the sail propulsion maneuver, i.e. when the orbital altitude is still almost GEO. On the other hand the corrected strategy shows consistent replicability across all of the escape trajectory.
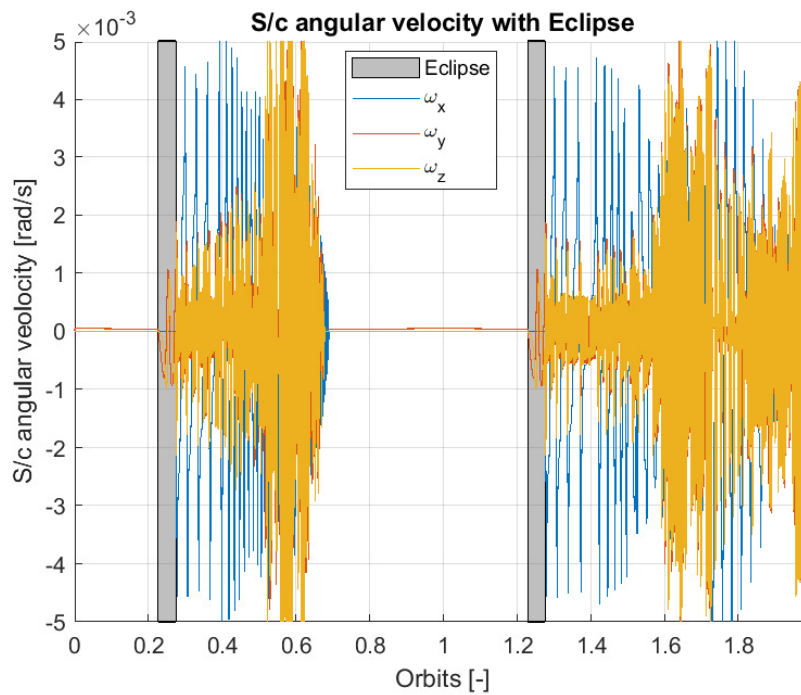
Figure 5.22: S/C angular velocity represented with the eclipse regions in a two orbits long simulation. No correction for eclipse disturbance.
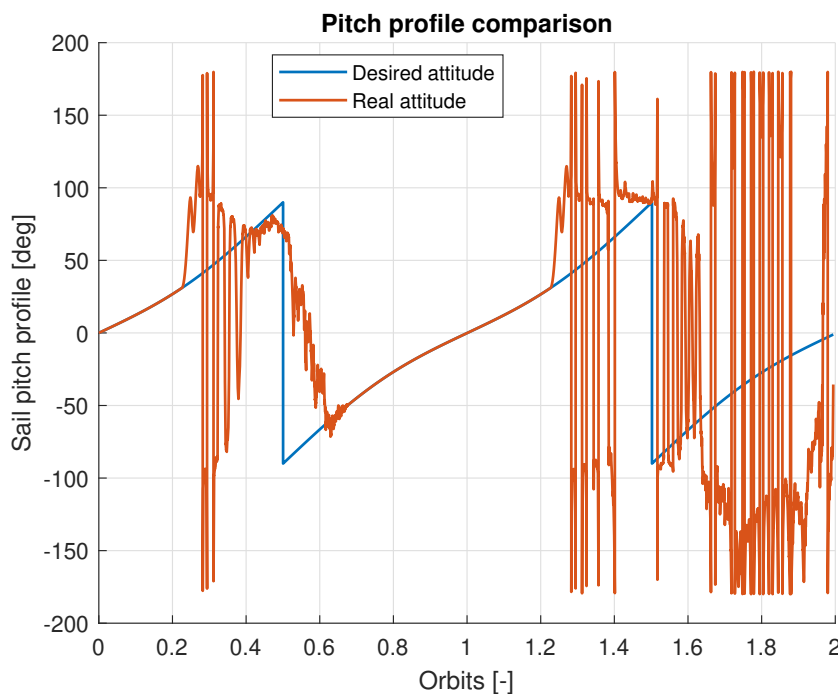

Figure 5.23: Pitch profile comparison for desired attitude and real attitude S/C in a two orbit long simulation with no correction for eclipse disturbance.
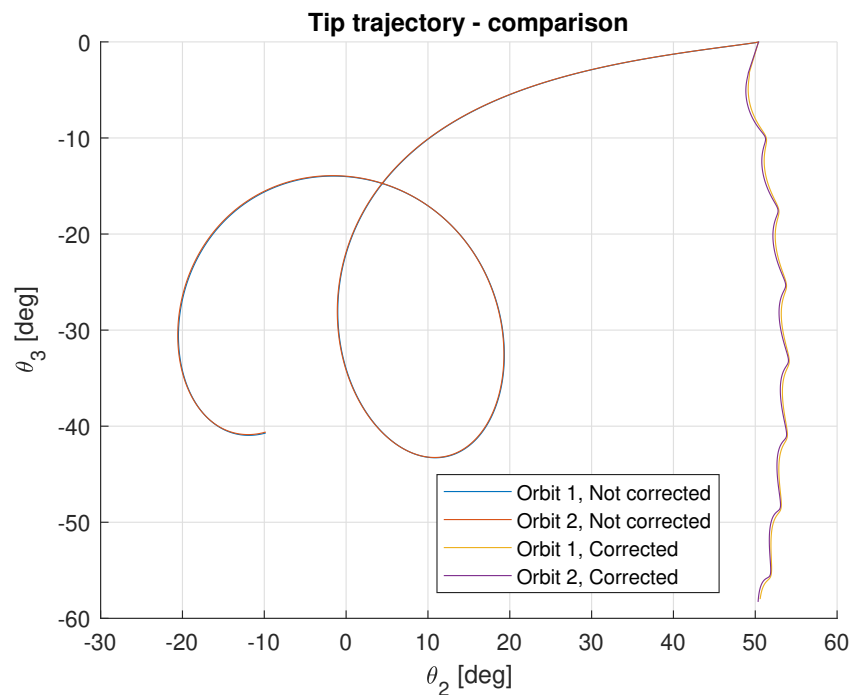
Figure 5.24: Sail normal tip trajectory in the orbital simulation's eclipse region. Distinction is made between corrected and non corrected with the gyroscopic stability strategy.

The main difference which can be noticed in Fig. 5.24 is the angle variation of the sail normal's tip with and without the spin rate. First, the uncorrected result shows a $40.5°$ vertical variation and a $60°$ horizontal one. The corrected strategy shows a larger $58°$ vertical variation but a much smaller $1.3°$ horizontal one. All the variations are considered from beginning to end of eclipse. This very difference is what makes the output of the corrected strategy manageable by the control system when eclipse ends. In fact, Fig. 5.25 which displays the angular velocity pattern across the two orbits confirms that the control system is able to control the S/C. This can be directly compared with the previous Fig. 5.22 where the control system is not able to efficiently, if at all, recover the S/C perturbed attitude. Moreover, the pattern shown in Fig. 5.25 is reproduced with the same shape for the whole escape orbit, confirming the replicability of the eclipse output condition caused by the gyroscopic stability strategy. Note that these results imply that the inclined only non-nominal condition, even with considerable γ angle as in Fig. 5.24 is easier for the control system to recover from than a mixed error both in terms of inclination and horizontal error. This is due to the fact that the control system has to recover from the attitude error while aligning the S/C to a varying desired attitude (in terms of α). Therefore, it is easier for it to cope with a larger error along just one axis.

Lastly, a confirmation of the success of the strategy and its effect on the control is the accuracy with which the real pitch angle tracks the desired one, see Fig. 5.26. This result can be compared to what is shown in section 5.5 too, in particular Fig. 5.23. Note that during
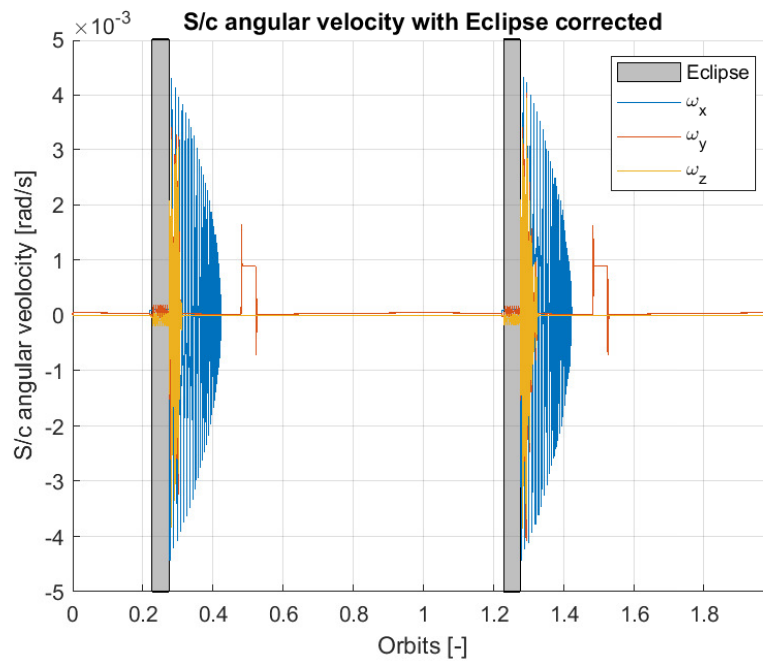
Figure 5.25: S/C angular velocity represented with the eclipse regions in a two orbits long simulation. The gyroscopic stability strategy correction for eclipse disturbance is activated.

eclipse it is impossible for the control hardware to steer the S/C towards the desired attitude since the SRP is null thus nullifying the control as well.
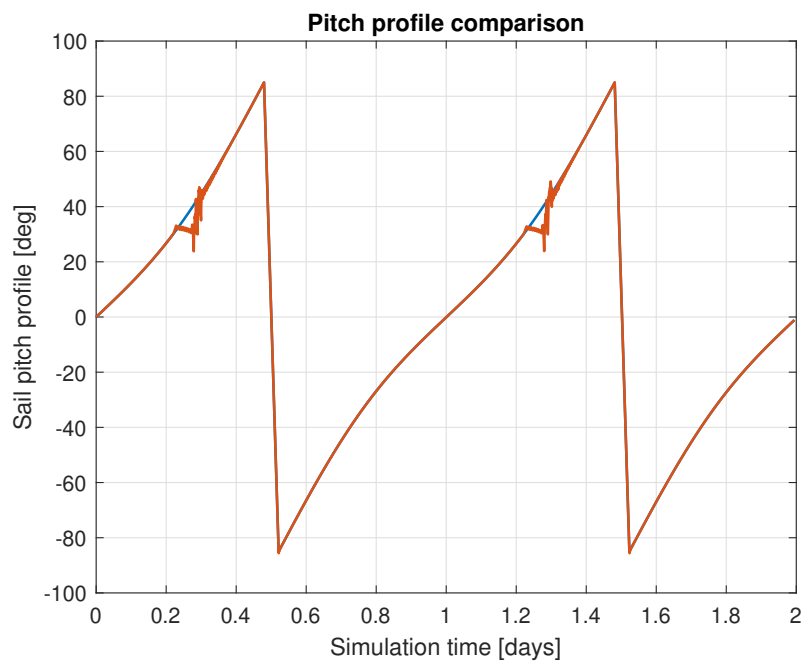
Figure 5.26: Pitch profile comparison for desired attitude (blue line) and real attitude (red line) S/C in a two orbit long simulation with correction for eclipse disturbance.

5.7 Escape orbit results

To merge together the results from the previous subsections, and ultimately the sub-goals of this work, the orbital simulation is used to simulate the escape of the Sunshade demonstrator S/C. The escape is here intended as the escape from the Earth's Sphere Of Influence, which has a radius of $R_{SOI} = 924\,000\,\text{km}$ [38]. These results include the selected escape trajectory as well as the environmental perturbations and the eclipse model. This provides a general overview of the challenges that the solar sail S/C is going to face during its escape orbit, while making meaningful considerations about the control system.

The time to escape is 1215 days, or 3 years and 4 months. Note that the initial condition is a circular orbit at GEO altitude with orbital plane correspondent to the ecliptic plane. The time to escape per se is not a performance metric within the scope of this work. In fact, it is influenced by the low lightness number $\beta = 0.011\,\text{m}\,\text{g}^{-2}$ which reflects a poor force generation capability of the design. This is mainly due to the relatively high mass assumed in this work for the demonstrator S/C. In Fig. 5.27 it is clear how the orbital raising maneuver is slow in the initial part of the escape trajectory. This because the increase in semi-major axis a is proportional to the a of the previous orbit through the quality of its force generation (as in subsection 2.3.3. With this latter being small, since the β is low, the growth in a per orbit is initially small too. As the orbit grows the per orbit growth in a increases, in Fig. 5.27 the trajectory becomes more distinguishable from the previous passage.
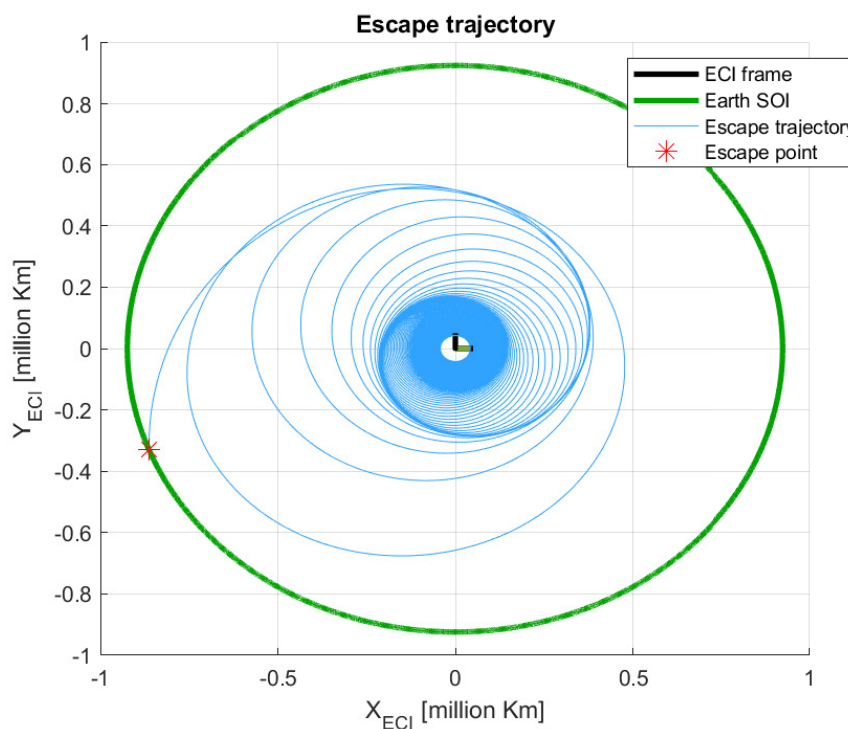

Figure 5.27: Orbital trajectory plot, solar sail escape trajectory, 1215 days long.

The consequence on the control system of such low β choice, on the other hand, is the resulting lowered parasitic SRP generated disturbance. Indeed, as seen in subsection 5.4.2, the control system maximum output torque is always grater than the highest disturbance torque, from start to escape. This alone does not grant control, being the control saturated. However, the control proves, numerically, always capable of controlling the S/C when required, i.e. at all times but during eclipse.

The most critical situation along a single orbit for the control system is the recovery of the desired attitude after eclipse. This repeats in the same way along all the orbits until escape. The pattern can be seen in Fig. 5.25, a detail of which is in Fig. 5.28, and it is due to the effect of the gyroscopic stability strategy explained in section 4.11. In order to properly understand the control behaviour in this particular portion of the orbit, virtually the only non-intuitive one, Fig. 5.29 is fundamental which contains a detail at the same scale with the control torques at the exit of eclipse. Moreover, Eq. 4.10 has to be expanded in:

$$I_X \dot{\omega}_{BX} = (I_Y - I_Z)\omega_Y\omega_Z + L_X \tag{5.1a}$$
$$I_Y \dot{\omega}_{BY} = (I_Z - I_X)\omega_X\omega_Z + L_Y \tag{5.1b}$$
$$I_Z \dot{\omega}_{BZ} = (I_X - I_Y)\omega_X\omega_Y + L_Z \tag{5.1c}$$

Note that this formulation assumes that Eq. 4.10 is written in a system of principal inertia axes. Just as the S/C exits eclipse the control systems tries to stop the roll rotation as well
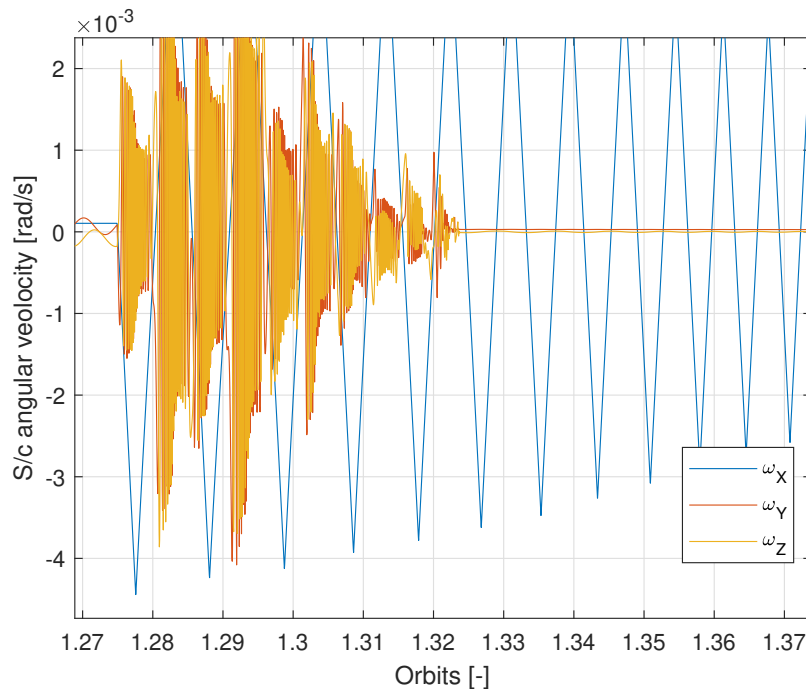

Figure 5.28: Detail: angular velocity curves, at the exit from eclipse.

as to steer the pitch angle to the new desired value. The difference between this latter and the
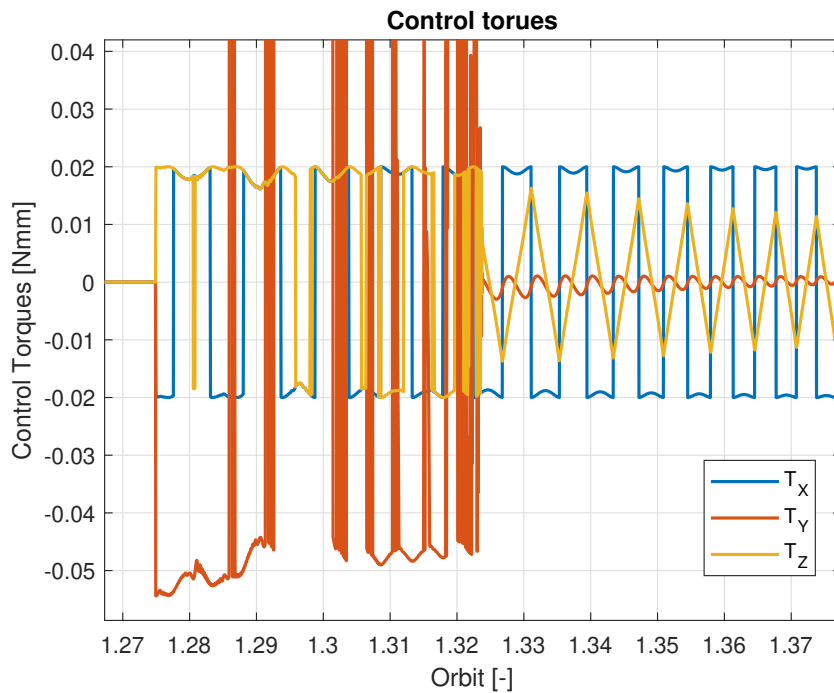
Figure 5.29: Detail: control torques curves in the same interval ad Fig. 5.28, at the exit from eclipse.

actual S/C pitch is significant since during eclipse the sail normal does not steer much in the horizontal direction as in Fig. 5.24 whereas the desired attitude continues to change. This saturates the roll torque and the pitch torque, both values are negative but their saturation laws are different. The yaw axis behaviour is also important, in fact, during eclipse the disturbances generate an angular velocity around this axis as well, even if it is less relevant than the roll one. At eclipse exit a saturated torque tries to stop this rotation.

In Fig. 5.28 it is evident that the control system is not able to directly stop the rotation along the pitch and yaw axis. The roll axis, on the other hand, is stopped slowly, this due to the constraint on the maximum control torque posed by the saturation law. The pitch angular velocity, and the yaw one engage in a "bottle-shaped" re-amplification. This affects the control performance but it is not due to the loss of control authority. Instead, it is due to the cross-coupling of the angular velocities together with the control torques. After the first bottle neck, ω_Y and ω_Z values re-grow the first time, negatively, exactly when ω_X shifts from negative to positive. There the first terms after the equal sign in Eq. 5.1b and Eq. 5.1c become negative due to this shift. These negative terms are added to the control torques, which at that moment along the pitch and yaw axes are negative as well, see Fig. 5.29. The sum of two terms that are now both negative produces a strong negative angular acceleration, which ultimately amplifies the angular velocities negatively.

The saturated control, after the re-amplification of the angular velocities tries to slow them

down again. This is done successfully until ω_X switches sign again, triggering once more a similar coupling phenomenon. This happens a total of 10 times, with a periodicity identical to the negative-to-positive and positive-to-negative transition of the roll angular velocity ω_X. The highest peaks are reached when the acceleration is negative, i.e. every time ω_X transitions from negative to positive. An unsaturated control would not allow this behaviour, reacting to the change in the control torque strong enough to prevent the re-amplification, however the saturated nonlinear PD implemented in this study is not able to prevent it. Lastly, note that in that the roll and yaw angular velocities, ω_Y and ω_Z have a phase displacement in their periodicity. This is due to the disturbances acting during the eclipse phase which cause the two to start the phenomenon from different initial velocities.

The starting orbital energy at the beginning of the simulation is $\epsilon_I = -4.73 \times 10^6$ J, the energy at escape is $\epsilon_E = -0.22 \times 10^6$ J. Note that this is different from section 5.2, in fact, here the definition of escape is based on the distance of the solar sail from the centre of Earth. When it is equal to the radius of the SOI of Earth the S/C is considered escaped. The energy build-up in Fig. 5.30, however, is similar to the one corresponding to the corrected escape trajectory in section 5.2. This because escape trajectory develops in the same way but for the eclipse and the post eclipse attitude recovery phases. These are, in fact, the only two portions of the orbit in which the control system is not capable of matching the actual trajectory with the desired one.
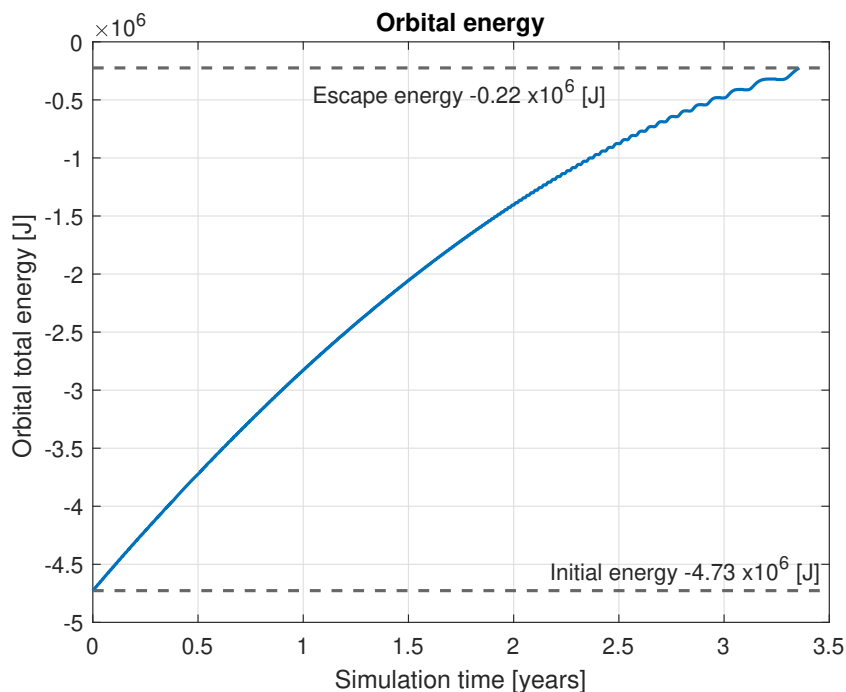

Figure 5.30: Orbital energy development curve for the 1215 days long escape trajectory.

The eccentricity, e, curve in Fig. 5.31 shows the year long periodicity of the apogee-

raising maneuver. Indeed, the rotation of Earth around the Sun causes the apogee to rotate as it is being raised: the optimal steering law tracks the Sun's relative motion to apply the highest acceleration possible on the sail. This progressively circularises the trajectory in the second part of the year and reduces the eccentricity. However, e does not return to zero after the first year, thus the curve has a long term growing trend. After the second year, the eccentricity growth in each orbit becomes evident in the curve in Fig. 5.31, in fact, the semi-major axis a is at this point big enough to cause significant eccentricity improvements even on a single orbit. It is worth reminding that the semi-major axis growth is proportional to the semi-major axis of the immediately previous orbit to the power of three. After a certain value of a, the increase per orbit is sufficiently big to bring about a significant increase in eccentricity as a consequence.

Towards the end of the escape trajectory, around and after three years from the start in Fig. 5.31, the eccentricity growth pattern of the single orbits can be distinguished. This is made of a steep growth, followed by a shorter decrease, then a flat region with a step in it middle. The steep growth phase corresponds to the last quarter of the previous orbit and the first one of the current orbit. The decrease in e that follows is due to the the second quarter of the current orbit, in this phase the optimal steering law is able to steer the sail in a way that it accelerates efficiently. That is the orbit is raised, i.e., the energy increased, but raising a region past the local apogee, thus being eccentricity efficient. The flat region is, in general, due to the region where the pitch angle is bigger than $\alpha = 60°$ or smaller than $\alpha = -60°$, here the SRP force is $F_S = 0\,\text{N}$ due to the billowing and wrinkling phenomena. See section 4.5. Lastly, the step in eccentricity is due to the rotation at half orbit, see section 4.3, there the sail is momentarily rotated so that it generates an SRP force in the direction opposite to the velocity. This causes a decrease in the altitude of the current perigee, this directly increases the eccentricity.

Fig. 5.32 the escape orbit semi-major axis, a, development curve is displayed. No particular remark is to be made. The growth is similar to a third order polynomial due to the relation expressed in Eq. 2.25 according to which the per orbit growth is proportional to the semi-major axis of the previous orbit cubed. Moreover, the flat regions with the step, downwards in this case, are due to the same thrust-off and rotational phenomena described in the previous paragraph.
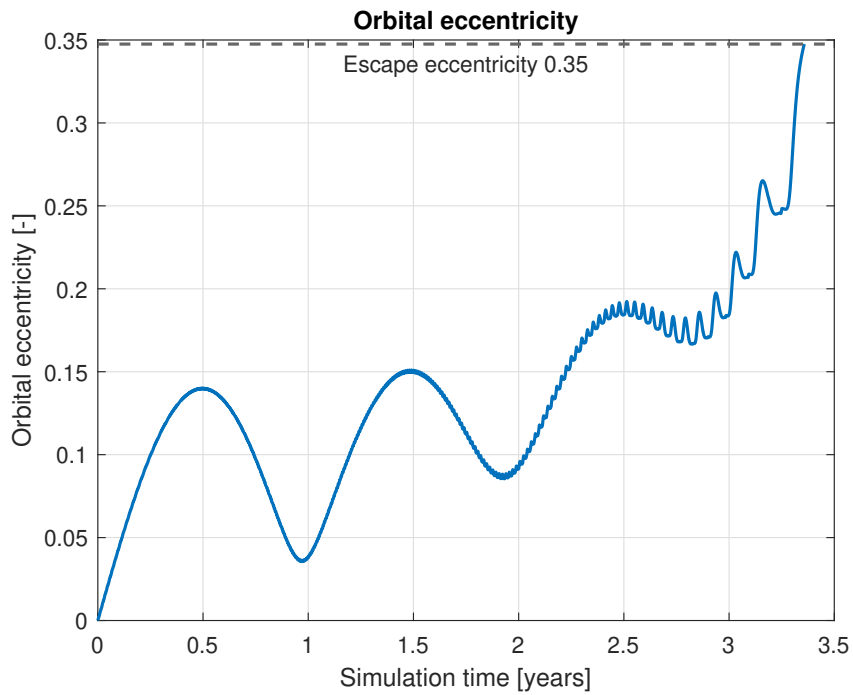
Figure 5.31: Eccentricity, e, development curve for the 1215 days long escape trajectory.
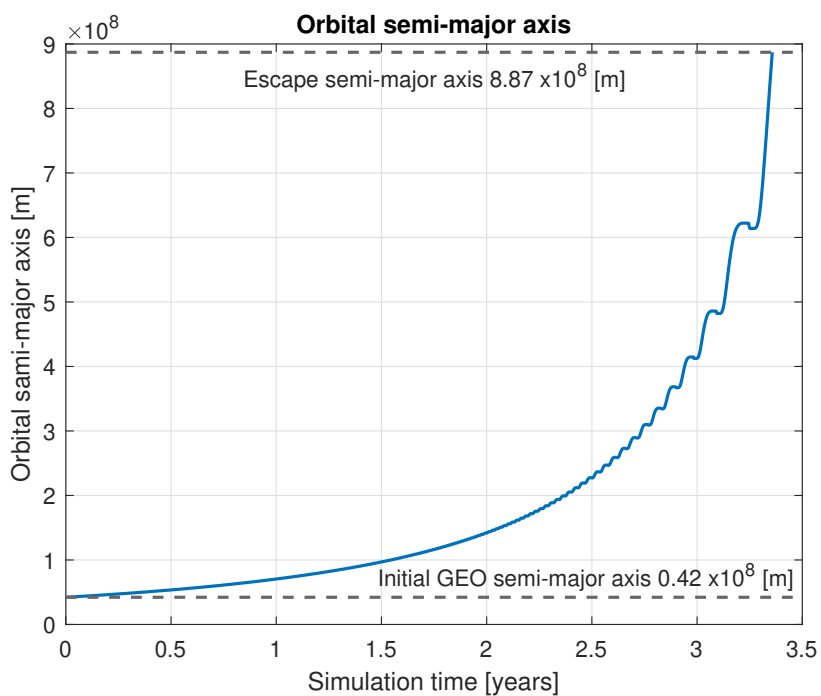
Figure 5.32: Semi-major axis, a, development curve for the 1215 days long escape trajectory.

Chapter 6

Discussion

Attitude control system implementation and operations

This study assesses the feasibility of the tip vanes as a control hardware in an attempt to escape the Earth SOI, however no detailed insight is given about the actual implementation of this system on the S/C. First, the very tip vanes would have to be folded themselves and then deployed, similarly to what is done with the main sail. This procedure is critical and prone to failure, arguably even more than the main sail, since the housing for the stored vanes is suspended at the end of a structural spar. Moreover, the stored vane housing would have to be at most as big as a quarter of the bottom face of the 6U CubeSat as in Fig. 6.1.
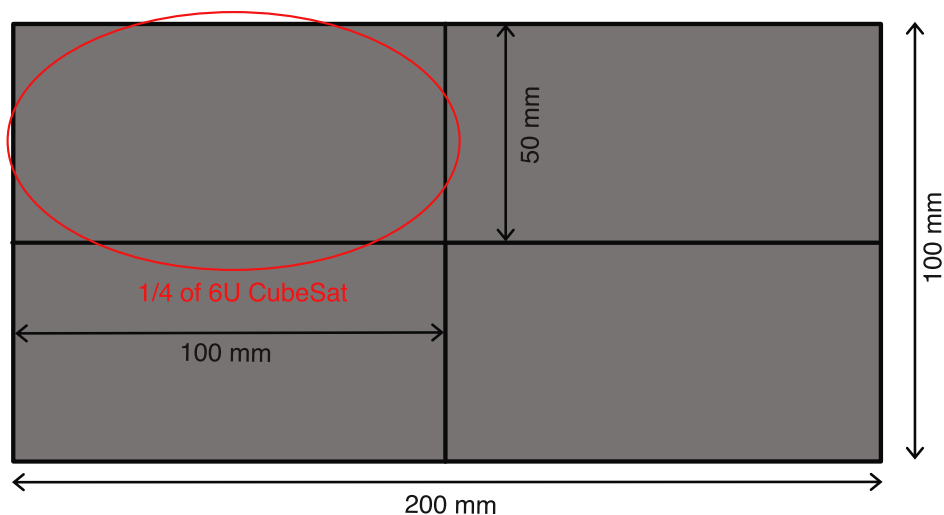
Figure 6.1: 6U CubeSat representation from $\mathbf{Z}_{BRF}$, highlighted a section worth $\frac{1}{4}$ of the bottom surface area.

At the tip of the spar is also to be found the electric motor which actuates the one DOF motion of each control vane. For this reason it is worth to underline the high constructive complexity and the strict mass requirement of this ensemble. The Sunshade demonstrator project group is currently studying and prototyping the construction of the spar-tip ensemble

but the TRL is still 1. As mentioned in subsection 4.4.1, the pitch control vanes are non reflective on one side, while the yaw/roll pair is reflective on both sides. This constructive choice of the demonstrator S/C is purely dictated by simplicity in the deflection angle algorithm solution, see section 4.6.3, and not linked to constructive complexity. Its feasibility and impact on the stowed vane volume have to be further elaborated with a dedicated study.

Moreover, the simulation performed to obtain the results in chapter 5 assumes a detumbled S/C as an initial condition for the start of the propulsion phase, i.e. with zero angular velocity in all the directions of the BRF reference frame. This is more important from an operational standpoint rather than a control one. In fact, the sail film deployment is the most delicate and prone to failures procedure, therefore it has to happen when the S/C is already detumbled. It is worth noting that prior to the sail film deployment the control vanes are stowed too. No operations plan has been devised but the expected deployment procedure envisions the vanes deployment as the last step. The only way of detumbling the S/C with the stowed tip vanes is by installing an auxiliary set of control actuators. No specific one is suggested, a more detail study on the topic alone woud have to be conducted. However, it is important to acknowledge here, that at GEO altitude the magnitude of the geomagnetic field is low and that a reaction-momentum wheel based control would require de-spin manoeuvres. Therefore the most reasonable control actuators to act as an auxiliary system are micro thrusters (cold gas or). Note that this system would be auxiliary, so the intent of making the control system of the Sunshade demonstrator not relying on propellant, from section 1.1 is preserved.

Lastly, the auxiliary control system should be capable of pointing deployed sail whilst being deployed and before the tip vanes are deployed themselves. This because the propulsion manoeuvre starts as soon as the sail has a portion of the film surface area visible to the incoming sunlight. An early commencement of the propulsion phase could cause wrong phasing of the semi-major axis growth. This is perilous for a successful escape, the reasons are explained in the "Eclipse phasing" section below.

Vanes' architecture and dimensions

In section 4.4 the four tip vanes are said to have a common direction for the rotation vector around which their DOF is. This means that the two pitch vanes rotate out of the sail film plane, not along the structural boom that supports them. While the roll/yam vanes rotate along their boom axis. It is worth noting that this characteristic is assumed as it allows for higher control torque along the pitch axis at a nominal attitude. Moreover, it simplifies the deflection angle algorithm, section 4.6.3. This choice is by no means the only possible one, a different st-up might end up in a successful mission too. However, this feasibility study would not cover such scenario so a different study would have to be performed to prove it.

Another assumption is made with regards to the required vanes size. Fig. 5.2 shows that for a solar sail with area $A = 100\,\mathrm{m}^2$ an estimated vane area of $A_v = 0.2\%A$ would be enough to grant enough angular acceleration to control the spacecraft. However, Fig. 5.1 shows that

with sail area $A = 9000 \, \mathrm{m}^2$ the estimated vane area to grant control grows to $A_v = 1\%A$. Therefore, this is the selected baseline vane area relatively to the total sail area. The roll/yaw vanes are increased to $A_v = 1.5\%A$. It is important to note that the previously mentioned estimations do not account for any perturbation or parasitic effect, i.e. the vane size at which the study has to be considered valid is $A_v = 1\%A$ only if $A = 100 \, \mathrm{m}^2$. With any bigger sail surface area no feasibility of the escape trajectory can be proven by this study. In fact, the vane area with any sail surface area greater than $A = 100 \, \mathrm{m}^2$ should be expected bigger than 1% of A.

Attitude determination

This study does not cover any attitude determination algorithm, however it assumes that a correct attitude estimation is performed on-board. This should result in a status vector containing the attitude and angular velocity parameters. The sensor array is itself not defined, but the suggested steering law is based on a number of different parameters which are to be estimated on board with dedicated sensors or systems. Note that the accuracy of these measurements is directly affecting the accuracy, therefore efficiency, of the escape trajectory. The most important one is the Sun position, found with a set of sun sensors, this information could also be used to determine part of the attitude. Another required parameter is the orbital velocity, in magnitude and direction, this is used to determine the optimal pitch angle to maximise the energy increase. Moreover, the position on orbit must be known to the system. The latter two can be transmitted from the ground [1] through ranging procedures.

Structural static loads and vibrations

One of the characteristics that enable the tip vane to be a viable control hardware is their distance from the Centre of Mass. In fact, even though each vane generates a relatively small force, the great moment arm assures a sensible amount of control authority. However, this physical feature of the sail design has an inherent flaw: the sensitivity of the structure to the loads generated by the control hardware itself. This both in terms of static loads, which could cause spar deformation or buckling, and vibrations which could cause the stimulation of natural frequencies. This aspect, once more, requires a study of its own which should be conducted alongside any control algorithm optimisation. Gain selection could prove itself relevant in making sure that the system never reaches load conditions that it can not withstand.

In this study the gain selection process is load condition agnostic, therefore the only metric which can be used to make load related considerations is the angular rate variation. In fact a high acceleration could generate vibrations in the structure and trigger spar deformation. The highest value reached during the simulated escape is $\dot{\omega}_B = 1.5 \times 10^{-3} \, \mathrm{rad \, s}^{-2}$. This value is intuitively small and considered not harmful for the structural integrity.

Sail ensemble performance

As stated in section 5.7, the Sunshade demonstrator sail lightness number $\beta = 0.011 \, \mathrm{m \, g^{-2}}$. This value is one order of magnitude lower than what suggested by Fuglesang and Miciano [8] in their study about the Sunshade system. The downward driver is the sail loading σ, which value measures the constructive efficiency of the system, see section 2.2. In Fuglesang and Miciano's work [8] the Sunshade S/C has a $A = 9000 \, \mathrm{m^2}$ sail compared to a $A = 100 \, \mathrm{m^2}$ one in this study, and a mass of $m_{tot} = 81 \, \mathrm{kg}$ compared to a $m_{tot} = 6 \, \mathrm{kg}$ considered here. These values yield one order of magnitude worse constructive efficiency for the smaller demonstrator S/C. The reasons are mainly two:

- **Nonlinear S/C components mass scalability:** The baseline internal subsystems found on-board a solar sail are the same, no matter the size of the S/C. Clearly, bigger mass implies bigger power and thermal subsystems, and a more complex auxiliary control system. But the increase in S/C mass is not linearly proportional with the increase in subsystems mass, hence the difference in load factor.

- **No attention to structural parameters:** While the full-scale Sunshade S/C study [8] contains structural considerations and research about possible future (and low TRL) material densities, this study does not. The more conservative assumption is made that the S/C is at the highest end of its 6U CubeSat specification [31]. Note that sail efficiency is, on the other hand, the same [8].

Simplistic control algorithm and steering law

The choice of a nonlinear PD control algorithm together with the planar steering law are dictated by the need to keep the study simple. However, it is fundamental to develop a more sophisticated algorithm altogether, including attitude estimation, before the actual mission takes place. This said algorithm should account for the coupling with the structural deformation and vibrations, similarly to what was done by Choi and Damaren [39] or Jiafu et al. [40]. Moreover the sail optical parameters degradation should be included in the SRP models, Dachwald et al. offer an example [41].

Moreover, it is worth noting that the steering law in this study inherently contains a number of simplifications. Among these the fact that by selecting the orbital plane coincident with the ecliptic plane an eclipse occurs in every orbit. This is considered to be a worst case scenario assumption since in each orbit during escape there is a phase with lack of propulsion. On the other hand, assuming the Sun co-planar with the escape trajectory overestimates the force available to accelerate the Centre of Mass. Moreover, there is no optimization in terms of the Earth SOI escape direction, the steering law does not take into account any pointing towards L1 of the escape trajectory. This might cause great inefficiencies in reaching the final destination, L1, after the escape and should be accounted for in future and more detailed trajectory-related studies [8]. Lastly, no effect of the Moon's gravitational field is included in the study: this might become relevant in the real escape situation since the orbit raising trajectory is a spiral with rings very close one to the other. This means that the transitory

phase in which the S/C is at a similar distance from the Earth as the Moon is extended, and the likelihood of being captured in the Moon's SOI high if not carefully avoided.

Tip vanes control not available in all orientations

By looking at Eq. 4.21 it is clear that the suggested control hardware configuration at some orientations, with respect to the Sun, has a null available control torque. In fact, whenever the S/C has the $\mathbf{Y}_{BRF}$ axis aligned with the incoming Sunlight the S_x and S_z components of the Sun direction vector are equal to zero. This results in zero overall obtainable control torque along any axis. It is worth noting that in any orientation within a certain neighbourhood of the above Sun aligned condition, the obtainable control torque is different from zero but still consistently low compared to the nominal value presented in Tab 5.3. Fig. 4.15 shows the coefficient which characterises the reduction of obtainable control force with inclination and, ultimately, gives an order of magnitude of the reduction in obtainable control resulting from an alignment of the $\mathbf{Y}_{BRF}$ with the Sunlight too.

The assumption made in this study, to accommodate for this inherent flaw in the control availability, is that the auxiliary control system is able to provide a sufficient torque to exit the zero-available-control-torque condition. This condition itself is assumed to be very rare, in fact, it never occurs in any of the simulated test cases in this study. The reason being that the environmental disturbance torques are always acting on the S/C, de facto acting as an auxiliary torque device that shifts the orientation away from the zero-available-control-torque one.

Eclipse phasing

Fig. 4.18 represents the eclipse-shadowed region along the orbital arc. This is present in each and every orbit of the escape trajectory, due to the assumption, in this study, of performing a planar escape on an orbital plane inclined as the ecliptic plane (discussed in section 4.3). This shadowed region, even if compensated by a gyroscopic stability strategy, sections 4.11, 5.6, does affect the accuracy with which the real pitch angle tracks the desired one, Fig 5.26. This is never a problem in the simulated test cases because the propulsive manoeuvre is phased correctly with the eclipse-shadowed region. In fact, if the propulsion where initiated at a greater true anomaly angle the eclipse perturbation on the pitch angle, α, would correspond with the transition from positive to negative alpha (at local apogee). See fig. 5.26 between 0.4 and 0.6 days and between 1.4 and 1.6 days. This is a particularly sensitive part of the orbit since it forces the sail to thrust in an opposite to velocity direction when it transitions from positive to negative α. If eclipse perturbed the pitch angle during this phase the consequences on the orbital energy increase would be detrimental. Moreover, since the local apogee rotates with a periodicity related to the relative Sun's rotation, the bad phasing would be carried on for the whole escape trajectory making the consequences even worse.

In any future study and implementation on the Sunshade demonstrator solar sail it is fundamental to take into account this phasing of the propulsion manoeuvre. This attention

is needed even if the selected orbit does not fall within the eclipse-shadowed region in every orbit of the escape trajectory.

Variable Cm - Cp off-set

In subsection 5.4.3 the sail sag/span ratio dependency on the Cm - Cp off-set is presented. It is clear from Fig. 5.17, 5.18, 5.19 that the said off-set is pitch angle, α, dependent. In this study this dependency is not accounted for when simulating the escape from Earth SOI, the fixed off-set value is set at 0.25% of the square sail side. The reason is that the deformation analysis, in subsection 4.9.3, is not as accurate and complete as the rest of the disturbances implementation. It is, indeed, developed to give an order of magnitude of the correlation between a sail deformation in the form of sag and the Cm - Cp off-set which is ultimately generating the whole pressure-related perturbations.

Once more, when iterating the design process of the Sunshade demonstrator S/C it is fundamental to include a complete analysis of the shift of the Centre of Pressure along the sail film with a varying pitch angle and deformation condition. This study is going to require a meshed model of the sail, see the work by Jenkins et al. "Prediction of Center of Pressure for Deformed Solar Sails" [42]. Therefore, it is suggested to develop it in conjunction with the load cases analysis discussed above.

Chapter 7

Conclusions and Future work

7.1   Conclusions

The feasibility study hereby conducted shows that it is possible to raise the orbit of solar sail up until escape from Earth's sphere of influence using a propellant-free control system. A set of tip-mounted control vanes, installed at the tip of the sustaining booms, is capable of providing the necessary control torque to accurately track an energy optimal escape. Their dimensions have to be 1%-1.5% of the sail surface for a square sail, and their shape right-triangular. The distance of each vane from the Cm is a driver to generate enough angular acceleration to control the Spacecraft and counteract the environmental disturbances. However, it might also lead to excessive deformation or structural weakness. In this study this distance value was fixed and dependent on the size of the square sail, of side $5\,\mathrm{m}$. Moreover, it still has to be established how the vane's structure can be developed and deployed in a small enough form factor, while bearing the loads generated by the tilting.

The physical principle that allows to propel the solar sail, i.e., the Solar Radiation Pressure, is also the same that enables the control actuators. This, however, is absent in eclipse conditions. It several orbital scenarios, e.g., all of the ones presented in this study, eclipse is unavoidable at least in some of the escape trajectory orbits. Exploiting the gyroscopic stability, i.e., spinning the S/C along one of its body axes, is enough to avoid the loss of control during and after eclipse. Moreover, the SRP is also exerting a perturbing effect on the S/C attitude: the sail film deformation off-sets the Cp with respect to the Cm generating a parasitic Solar Radiation Pressure force. If the sail is deformed with a parabolic shape, the Cm - Cp off-set is 0.25% of the sail side with a sag/span ratio of 4%, i.e. $20\,\mathrm{cm}$ of sag with a $5\,\mathrm{m}$ sided sail, Fig. 4.16.

Even if the Sunshade demonstrator S/C model suggested in section 4.4 is proven to escape in 3 years and 4 months, it should be noted that all of the simulations run in nominal scenarios. Unforeseen events, particularly related to attitude, could harm the successful completion of the trajectory. This because, as it is the control system has some evident weaknesses. First, the lack of control torque available at certain inclinations: when the sunlight is aligned with the

$\mathbf{Y}_{BRF}$ axis the only output of the control hardware is $0\,\mathrm{N\,m}$. Second, the structural sensitivity to applied loads, especially the ones exerted by the control system. The structure, built with 4 deployable booms and a $2.5\,\mathrm{m}$ thin mylar film, is intuitively deformable by loads applied perpendicular to the boom extension direction. Therefore, it becomes clear that during a real life escape the S/C could lose controllability or even break due to unconventional attitude states, i.e., orientations and angular velocities.

Lastly, the whole study is based on a successful deployment of the sail ensemble. This can occur only under controlled conditions, hence the need for an auxiliary control system capable not only of stopping any after-launch tumbling, but also of properly phasing the propulsion maneuver.

7.2 Limitations

Even though the escape is proven to be successful, it is accomplished with several limitations and simplifications. While most simplifications are discussed throughout the work in the form of assumptions, here the main limitations are listed.

First, the steering law used to determine the desired attitude to maximise the orbital energy growth is strictly planar. Indeed, it is developed to work with an orbit whose orbital plane is correspondent to the ecliptic plane. Moreover, no perturbing force is included in the simulated test cases. The perturbing accelerations are listed in section 4.9 but these do not affect the motion of the Centre of Mass which, especially in inclined orbits, undergoes a number of perturbing effects [43].

The Spacecraft model contains a few limiting assumptions too. First, the Cm is assumed to be in the centre of the sail ensemble. This condition might be sought after in a final realistic S/C design, but it is not possible to reproduce it exactly, at least not with conventional sail assemblies [1]. Among the consequences of this simplification there is the absence of a perturbing torque generated by the Cm - Cp off-set along the $\mathbf{X}_{BRF}$ axis. Keep in mind that the off-set discussed in section 4.9 is on the $\mathbf{YZ}_{BRF}$ plane. Moreover, no deformation is accounted for in the sail structure and in the control tip vanes, the only element for which deformation is accounted for is the sail film, see subsection 4.9.3. However, the model applied here is based on standard deformation coefficients and is not specific to this design.

Lastly, the trajectory is optimised for orbital energy increase but not for minimum time to escape nor to the final destination at L1. This, as shown by Fuglesang and Miciano [8], is largely affected by the direction of the S/C at the exit from the SOI. In this study this consideration is disregarded.

7.3   Future work

The next steps in the context of the Sunshade demonstrator projects are twofold. First, the Spacecraft design and TRL should be developed further. Second, the scalability of the demonstrator to the Sunshade S/C and constellation should be analysed qualitatively and quantitatively.

Under the category of S/C design development falls the attitude and orbit control system, the direct continuation of this feasibility study. With this respect a number of actions are required, starting with the study of the control system performance in the trajectory from Earth SOI escape to L1 and at L1, maintaining the equilibrium point. Moreover a high performing control algorithm should be designed and tuned according to the problem limitations and boundary conditions of a fully three-dimensional steering law. For this, the simulation software used in this study could be used as a baseline.

On the other hand, the Spacecraft structural model should be built in a CAD environment and a structural analysis should be performed. Such model, together with the mass properties, is highly informative to the control system. This, however, is second to the development of the tip vanes deployment and actuation subsystem, which is, to date, ongoing within the project group. Lastly, an auxiliary control system has to be designed and integrated in the AOCS ConOps.

References

[1] C. R. McInnes, *Solar Sailing. Technology,Dynamics and Mission Applications*. Springer-Praxis, 1999. ISBN 978-1-85233-102-3

[2] S. Gabriel, E. Rogers, and M. Leomanni, "The applicability of pulsed plasma thrusters to rendezvous and docking of cubesats," 01 2013.

[3] J. Atchinson and M. Peck, "Length scaling in spacecraft dynamics," *Journal of Guidance Control, and Dynamics*, FEbruary 2011. doi: 10.2514/1.49383

[4] C. R. McInnes, "Space-based geoengineering: challenges and requirements," *Journal of Mechanical Engineering Science*, 2009. [Online]. Available: https://journals.sagepub.com/doi/10.1243/09544062JMES1439

[5] M. Kramer. Welcome to the spaceflight revolution. Axios. (Accessed on: 27.05.2021). [Online]. Available: https://www.axios.com/commercial-spaceflight-revolution-competitions-e39f783d-3bde-4da4-991c-2782e09c737d.html

[6] R. Lindsey and L. Dahlmann. Climate change: Global temperature. (Accessed on: 16.03.2021). [Online]. Available: https://www.climate.gov/news-features/understanding-climate/climate-change-global-temperature#

[7] Geoengineering the planet: The possibilities and the pitfalls. YaleEnvironment360. (Accessed on: 2021-03-16). [Online]. Available: https://e360.yale.edu/features/geoengineering_the_planet_the_possibilities_and_the_pitfalls

[8] C. Fuglesang and M. Miciano, "Realistic sunshade system at 11 for global temperature control," *Acta Astronautica*, no. Vol. 186, 2021. [Online]. Available: https://www.sciencedirect.com/science/article/pii/S0094576521001995

[9] Small solar power sail demonstrator 'ikaros' successful solar sail deployment. Japan Aerospace Exploration Agency. (Accessed on: 2021-03-22). [Online]. Available: https://www.jaxa.jp/press/2010/06/20100611_ikaros_e.html

[10] S. Stirone. Lightsail 2 unfurls, next step toward space travel by solar sail. (Accessed on: 2021-03-22). [Online]. Available: https://www.nytimes.com/2019/07/23/science/lightsail-solar-sail.html

[11] R. L. Sohn, "Attitude stabilization by means of solar radiation pressure," *ARS Journal*, vol. 29, pp. 371–373, May 1959.

[12] B. Wie, *Space Vehicle Dynamics and Control*, 2nd ed. Amer Inst of Aeronautics, 2008, ch. 12. ISBN 978-1563479533

[13] ——, "Solar sail attitude control and dynamics, part 1," *Journal of Guidance Control and Dynamics*, August 2002. [Online]. Available: https://www.researchgate. net/publication/228833626_Solar_Sail_Attitude_Control_and_Dynamics_Part_1

[14] Y. Wu, "Radiometry, brdf and photometric stereo," in *EECS 432-Advanced Computer Vision Notes Series 3*, 2017. [Online]. Available: http://users.eecs.northwestern.edu/ ~yingwu/teaching/EECS432/Notes/lighting.pdf

[15] H. Shaub and J. Junkins, *Analytical Mechanics of Space Systems*, 3rd ed. Amer Inst of Aeronautics , August 2014. ISBN 9781624102400

[16] International geomagnetic reference field (igrf), 13th generation calculator. British Geological Survey. (Accessed on: 09.07.2021). [Online]. Available: http://www. geomag.bgs.ac.uk/data_service/models_compass/igrf_calc.html

[17] E. B. et al., "Spacecraft magnetic torques," NASA, NASA Space Vehicle Design Criteria (guidance and Control), March 1969. [Online]. Available: https://ntrs.nasa. gov/api/citations/19690020961/downloads/19690020961.pdf

[18] B. Cour-Palais, "Meteoroid environment model: 1969 (near earth to lunar surface)," NASA, NASA SP-8013, March 1969. [Online]. Available: https: //ntrs.nasa.gov/api/citations/19690020961/downloads/19690020961.pdf

[19] P. Hughes, *Spacecraft Attitude Dynamics*. Dover, 2004. ISBN 9780486140131

[20] J. Wertz, *Spacecraft Attitude Determination and Control*. Springer, 1978. ISBN 9789027712042

[21] G. Cole and M. Woolfson, *Planetary Science: The Science of Planets Around Stars*. Institute of Physics Publishing, 2002.

[22] J. B. et al., "Radiation forces on small particles in the solar system," *Icarus*, 1979. doi: 10.1016/0019-1035(79)90050-2

[23] How a mission is chosen. European Space Agency. (Accessed on: 24.05.2021). [Online]. Available: https://www.esa.int/Science_Exploration/Space_Science/How_ a_mission_is_chosen

[24] diff-differentiate symbolic expression or function. MathWorks. (Accessed on: 26.05.2021). [Online]. Available: https://it.mathworks.com/help/symbolic/diff.html

[25] Fixed step solvers in simulink. MathWorks. (Accessed on: 26.05.2021). [Online]. Available: https://it.mathworks.com/help/simulink/ug/fixed-step-solvers-in-simulink. html

[26] W. Holmes, "Frames of reference, orbits and ellipses," The University of Sydney, 2017. [Online]. Available: https://web.aeromech.usyd.edu.au/AERO2705/ 2017_course_notes/AERO2705_Wk2_2017_Orbits_Elipses.pdf

[27] J2000.0. Wikipedia. (Accessed on: 03.06.2021). [Online]. Available: https://it. wikipedia.org/wiki/J2000.0

[28] T. Brady and C. T. et al., "The inertial stellar compass: A new direction in spacecraft attitude determination," in *16th Annual AIAA/USU Conference on Small Satellites*, August 2002.

[29] D. A. Spencer, B. Betts, and J. M. B. et al., "The lightsail 2 solar sailing technology demonstration," *Advances in Space Research*, 2020. [Online]. Available: https://doi.org/10.1016/j.asr.2020.06.029

[30] A. R. Sobey and T. R. Lockett, "Design and development of nea scout solar sail deployer mechanism," in *43rd Aerospace Mechanisms Symposium*, May 2016. [Online]. Available: https://ntrs.nasa.gov/api/citations/20160008143/downloads/20160008143. pdf

[31] *6U CubeSat Design Specification Revision 1.0*, June 2018. [Online]. Available: https://static1.squarespace.com/static/5418c831e4b0fa4ecac1bacd/t/ 5b75dfcd70a6adbee5908fd9/1534451664215/6U_CDS_2018-06-07_rev_1.0.pdf

[32] C. Falthammar, *Space Physics*, 2nd ed. KTH - Royal Institute of Technology, August 2001. [Online]. Available: https://www.kth.se/social/upload/ 521f2beaf276542c27bf78f4/Falthammar.pdf

[33] Root of a nonolinear function. MathWorks. (Accessed on:293.06.2021). [Online]. Available: https://it.mathworks.com/help/matlab/ref/fzero.html

[34] L'algoritmo di newton-gauss. Wikipedia. (Accessed on: 30.06.2021). [Online]. Available: https://it.wikipedia.org/wiki/Algoritmo_di_Gauss-Newton

[35] M. Choi and C. J. Damaren, "Control allocation of solar sail tip vanes with two degrees of freedom using elliptical constraints," in *AIAA Guidance, Navigation, and Control Conference*, August 2012.

[36] *Mylar*, TAP Plastic, May 2010. [Online]. Available: https://www.tapplastics.com/ image/pdf/Tech%20Data-2011-%20Mylar.pdf

[37] L. Felicetti, M. Ceriotti, and P. Harkness, "Attitude stability and altitude control of a variable-geometry earth-orbiting solar sail," *Journal of Guidance, Control, and Dynamics*, 2016. doi: 10.2514/1.G001833

[38] M. Peet, "Interplanetary mission planning," Illinois Institute of Technology, 2012. [Online]. Available: http://control.asu.edu/Classes/MMAE441/Spacecraft/441Lecture24.pdf

[39] M. Choi and C. J. Damaren, "Structural and attitude dynamics and control of a solar sail using two degrees of freedom tip vanes," in *2nd AIAA Spacecraft Structures Conference*, January 2015.

[40] J. L. et al., "Potential solar sail degradation effects on trajectory and attitude control," November 2014.

[41] D. et al., "Potential solar sail degradation effects on trajectory and attitude control," in *AIAA Guidance, Navigation, and Control Conference*, June 2005.

[42] "Prediction of center of pressure for deformed solar sails," in *46th AIAA/ASME/ASCE/AHS/ASC Structures, Structural Dynamics Materials Conference*.

[43] D. X. et al., "Dong x, hu c, long t, li y. numerical analysis of orbital perturbation effects on inclined geosynchronous sar." in *Sensors (Basel)*, September 2016. doi: 10.3390/s16091420
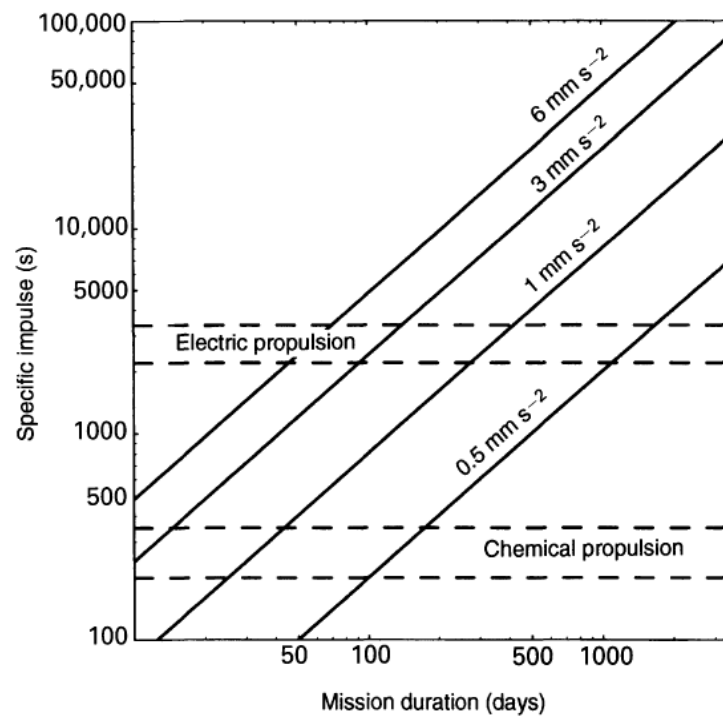
Appendix A

Figure A.1: I_{sp} versus mission duration comparison as found in McInnes "Solar Sailing. Technology,Dynamics and Mission Applications" [1].
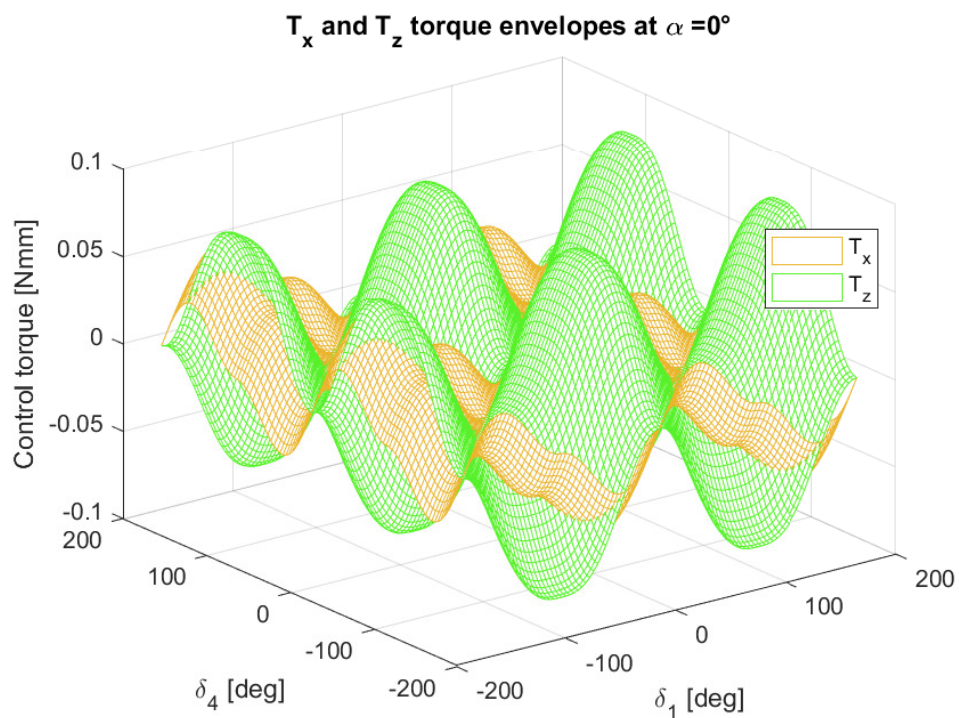
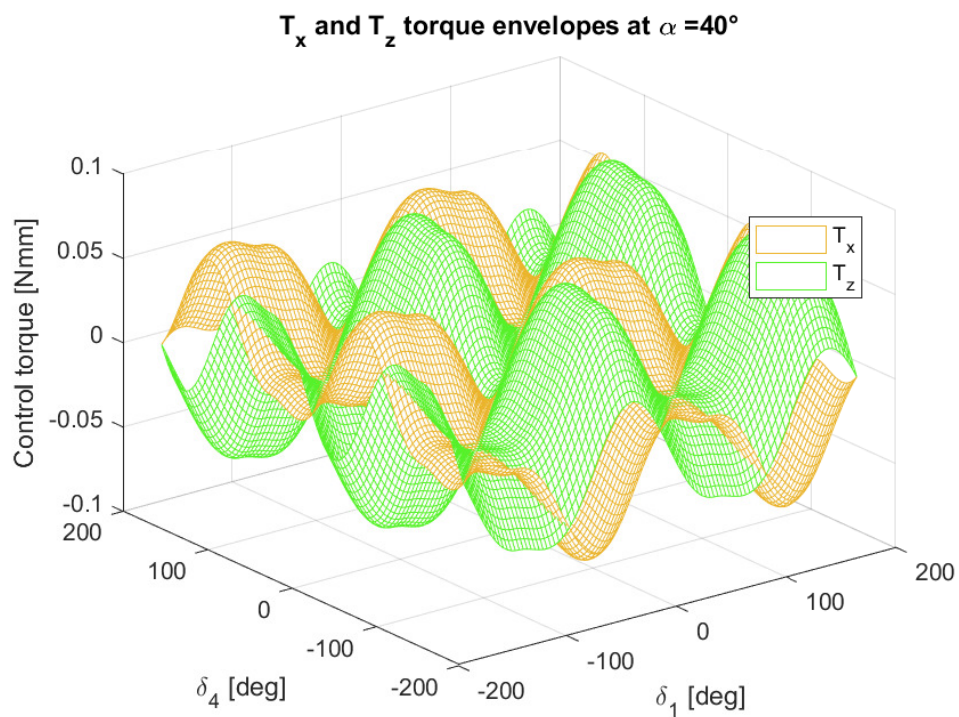Figure A.2: Roll and yaw torques overlapped envelopes at $\alpha = 0°$, full possible envelope.

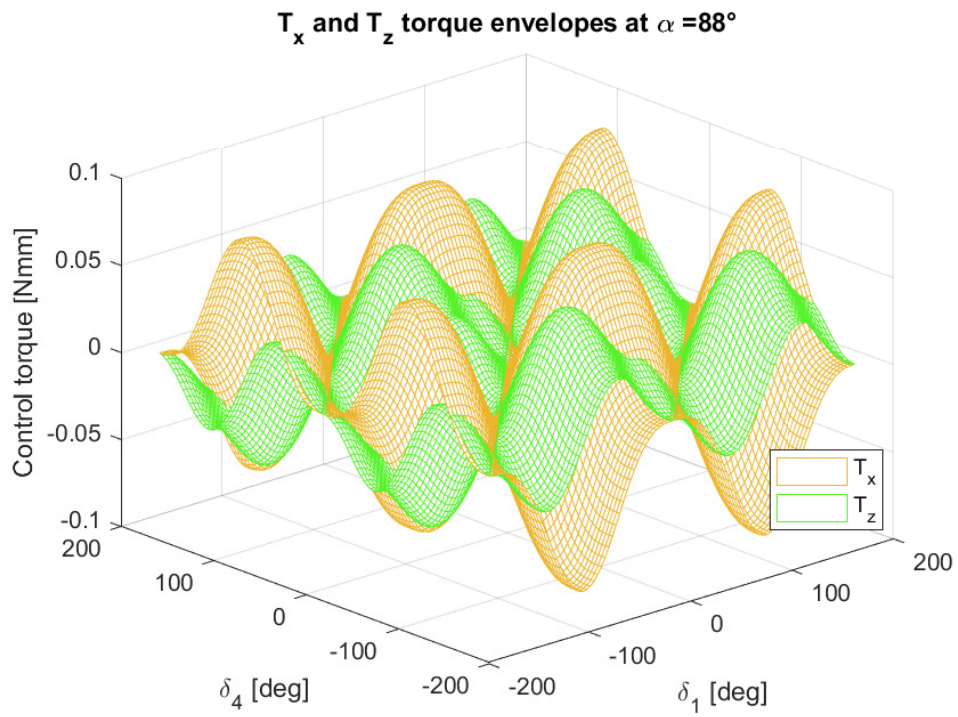Figure A.3: Roll and yaw torques overlapped envelopes at $\alpha = 40°$, full possible envelope.

Figure A.4: Roll and yaw torques overlapped envelopes at $\alpha = 88°$, full possible envelope.